Hisaki and ALMA observations of spatial and time variations of Io's SO2 atmosphere and neutral oxygen torus associated with volcanic activities

Doctoral Thesis
博士論文

Hisaki and ALMA observations of spatial and time variations of Io's SO_2 atmosphere and neutral oxygen torus associated with volcanic activities

Hisaki と ALMA による火山活動に伴うイオの SO_2 大気と中性酸素トーラスの空間・時間変動の観測

東北大学大学院理学研究科
地球物理学専攻

Ryoichi Koga
古賀　亮一

論文審査委員

坂野井　健　准教授（指導教員・主査）
笠羽　康正　教授
小原　隆博　教授
平原　靖大　准教授（名古屋大学）
土屋　史紀　助教
鍵谷　将人　助教

2019
令和元年

Acknowledgements

I would like to express my sincere thanks to my supervisor, Associate Professor Takeshi Sakanoi. His patient guidance allows me to continue my study for 5 years. I would like to express special thanks to Assistant professor Fuminori Tsuchiya. He teach me analyzing Hisaki data and give me fruitful suggestion continuously. I also appreciate Professor Yasumasa Kasaba and Takahiro Obara, Associate Hiroaki Misawa and Assistant professor Masato Kagitani and Emeritus Professor Shoichi Okano for providing constructive idea mainly at the weekly seminar. I am very grateful to Professor Yuto Kato and Naoki Terada, Associate Professor Atsushi Kumamoto and Isao Murata, and Assistant Professor Takeshi Kuroda and Hiromu Nakagawa for useful suggestion and comments mainly at the joint seminar of Planetary and Space Physics Group, Tohoku University.

I thank Hisaki science team member, especially Professor Ichiro Yoshikawa, Dr. Kazuo Yoshioka, Dr. Kimura Tomoki, Dr. Go Murakami, Dr. Atsushi Yamazaki, Dr. Nick Schneider, Mr. Fumiharu Suzuki, Ms. Reina Hikida and Mr. Eddie Nerney. They not only discuss me about science of Jupiter magnetosphere, but also give me much opportunity to talk with foreign researchers. Dr. Yoshioka and Ms. Reina Hikida provided the precious data of plasma parameters in Io torus derived by Hisaki, and Dr. Hajime Kita provided the data of Io plasma torus light curve. Dr. Mizuki Yoneda provided the data of sodium nebula emission and gave me the motivation to study Io's surface and atmosphere. I thank the collaboration with the Hisaki team supported by NASA's Hisaki Participating Scientist Program. Especially, Dr. Fran Bagenal and Dr. H. Todd Smith became co-author of our peer-reviewed paper and gave me grateful advice aiming to publish our paper.

I also thank the collaboration with Dr. Yasuhiro Hirahara and Mr. Tatsuya Suzuki at Nagoya University on the research of Io's atmosphere by analyzing ALMA archive data. They taught me radio astronomy and analysis of ALMA data, and discussed interesting phenomena of Io's atmosphere.

Acknowledgements

Thanks to my laboratory members, Mr. Fukizawa Mizuki, Ms. Asuka Hirai, Mr. Naoshi Yagi, Mr. Toshihisa Suzuki, Ms. Aina Oura, Mr. Kazuki Yamaguchi, Mr. Kanbara Ayumu, Mr. Tatsuya Fujimoto, Ms. Miki Kawamura, Mr. Takumi Kera, Mr. Risei Kogure and Mr. Yuichiro Seki.

The Hisaki/EXCEED data is archived in the Data Archives and Transmission System (DARTS) (http://hisaki.darts.isas.jaxa.jp/).
The SORCE solar spectral irradiance data is archived at the LASP Interactive Solar Irradiance Data Center (LISIRD) (http://lasp.colorado.edu/lisird/index.html).
CHIANTI is a collaborative project involving the University of Cambridge (UK), George Mason University (USA), and the University of Michigan (USA).

This paper makes use of the following ALMA data: ADS/JAO.ALMA# 2017.1.00670.S. ALMA is a partnership of ESO (representing its member states), NSF (USA) and NINS (Japan), together with NRC (Canada), MOST and ASIAA (Taiwan), and KASI (Republic of Korea), in cooperation with the Republic of Chile. The Joint ALMA Observatory is operated by ESO, AUI/NRAO and NAOJ.

This work (R. Koga) has been supported by Grants-in-Aid for the Japan Society for the Promotion of Science (JSPS) Research Fellowship for Young Scientists. KAKENHI Grant Number is 19J10742.

Finally, I want to express my grateful appreciation to my family. Especially, my parents continuously supported me in both financial and mental aspects.

Abstract

Io is the most volcanically active body in the solar system, which is the important target to understand the processes from the generation of gasses from geologically active bodies to the escape of the gasses into space.

There are many studies about material transport and energy coupling processes in different areas from the Io's surface to the orbit (surface, atmosphere, neutral cloud and Io plasma torus (IPT)). Previous studies showed the temporal variations of Io's atmosphere. For example, the increase of S^+ in the torus simultaneously occurred with the increase of neutral sodium nebula during volcanically active period. Observation of spatial distribution of Io's atmosphere (main component is SO_2), and neutral cloud (main component is oxygen atom) is important to understand the escape process of neutrals from Io, as well as the source and loss processes of IPT. However, such spatial distributions were poorly observed so far. To clarify these issues, it is useful to perform ground-based millimeter/submillimeter observation with a high spatial resolution of the SO_2 atmosphere distribution on Io's disk, and to monitor the UV OI 130.4 nm emission around Io's orbit.

ALMA (Atacama Large Millimeter /Submillimeter Array) can resolve the Io's disk (beam size is ~0.3") and observes several SO_2 lines very precisely. The extreme ultraviolet spectrograph called EXCEED installed on the Hisaki satellite continuously observes the spatial distribution and variations Io plasma torus in the wavelength of 55-145 nm, and faint atomic oxygen emission at 130.4 nm since the launch in 2013. These ALMA and Hisaki observations give us unique opportunities to examine the precise time and spatial variations in the Io's atmosphere and plasma torus.

Purpose of this study is listed as follows.

- To reveal the spatial distribution and temperature variability in the Io's atmosphere and find effects of volcanism to generate the Io's atmosphere.
- To clarify the spatial distribution and time variations of Io's neutral oxygen cloud, and discuss the source and loss processes of oxygen ion in the torus.
- To understand the response of IPT to volcanic activity.

Abstract

We examined the change of spatial distribution of SO_2 atmosphere before and after Jupiter ingress of Io using the ALMA archive data obtained on 20 March 2018. We found the presumed volcanically active areas in the east side and northern high latitude region, and in the west side near the equator. In the former area, two components with high and low velocities are clearly identified in the velocity distribution. The result suggests the significant volcanic plume would generate complex atmospheric dynamics with high and low velocity motions. In the later area, the rotational temperature of SO_2 is 311±41 K after ingress, much higher than temperature of sublimation atmosphere (~100-200 K). The temperature might reflect the gas emitted form volcanoes or heated by a hot lava lake. The observation also showed the dayside atmosphere consists of multiple gases with different temperatures. This suggests that the atmosphere has different sources of volcanism and sublimation, and/or a non-uniform vertical temperature profile. The enhancements of the sodium nebula and IPT on the dusk side are observed by the ground-based telescope and Hisaki during this period. The simultaneous enhancement of sodium nebula and IPT would potentially be caused by volcanic plumes that increase the height of exobase, and gain the atmospheric sputtering.

From the Hisaki data obtained from November to December 2014 during volcanically quiet conditions (hereafter, referred to as the normal density period), we estimated the azimuthal distribution of neutral oxygen cloud. We found a dense region of neutral oxygen near Io (called "banana cloud"), as well as a longitudinally uniform diffuse region along the Io's orbit. The radial distribution showed the neutral oxygen cloud spreads out to 7.6 Jupiter radii (R_J), where the brightness drops below ~1 R. We also found the dawn-dusk asymmetry of oxygen emission from 5 to 6 R_J, and that the emission on the dusk side emission was larger than that the dawn side.

The enhancement of OI brightness started around day of year 20 in 2015, and continued for 3 months (hereafter, referred to as the high density period). The radial distribution of oxygen cloud showed the outward expansion up to 8-8.6 R_J during the period from January to March of 2015, and recovered by April. Assuming the north-south thickness of oxygen cloud is 1.2 R_J, we estimated the number density of oxygen cloud in the Io's orbit to be 91^{+29}_{-25} cm^{-3} during the high density period. This is three times larger than that during the normal density period (27^{+8}_{-7} cm^{-3}). Concerning the longitudinal distribution of the OI emission during the high density period, we suggest that the neutral oxygen cloud is composed of the banana cloud and diffuse region along Io's orbit, similar to that during the normal density period. However, it is clear that the total amount of the neutral increased during the high density period, and the distribution width along the orbit may be enlarged. We also found that the neutral escape rate from Io significantly increased during the high density period.

We estimated the oxygen plasma source rate as 410 kg/s from the radial distribution by using the plasma parameters derived from Hisaki and Voyager observations. Out of 410 kg/s, electron impact and charge exchange cause 100 kg/s and 310 kg/s of ionization of oxygen atom,

respectively. From the variations of OII 83.4 nm and OI 130.4 nm emissions from November 2014 to May 2015, we calculated the lifetimes of O^+ to be 40.5 days in the normal density period and to be 20.5 days in the high density period. The main loss process of O^+ is outward radial transport. The result suggests that the increases of neutrals and ions produce the faster outward transport.

Contents

Chapter 1 Introduction

1.1 Source and escape processes of Io's atmosphere

Io is one of the Galilean moons of Jupiter, and its orbital distance is about 5.9 R_J (R_J; a radius of Jupiter, 71,492 km) and orbital period is 1.769 days. Io is the most volcanically active body in the solar system, and has a thin atmosphere mainly composed of SO_2. Escape processes of neutrals ejected from Io are summarized in Figure 1.1. It has been discussed whether the immediate source of Io's atmosphere is sublimation of surface frost or direct volcanic input (see reviews by McGrath et al. (2004) and by Lellouch et al. (2007)). Atmospheric generation by volcanism is mainly distinguished as one of two main processes: "plume events" (like geysers), which emit SO_2-dominant gases, and "lava-lake evaporation," whereby hot lava evaporates SO_2 frost. Electrons and photons dissociate the SO_2 in Io's atmosphere into SO, sulfur, and oxygen atoms (e.g., Smyth and Wong, 2004). Characteristic timescales of escaping neutral material in the torus is shown in Table 1.1. The most important interaction of neutrals around Io with ions is atmospheric sputtering, the process the torus ions collide with neutrals around Io, which in turn collide with other neutrals. However, electron impact ionization, charge exchange, and electron impact dissociation are also key reactions. Saur et al. (2003) found the elastic collision rate at Io exceeds the pickup rate by at least a factor of five from model calculations. When neutrals escape from Io's gravity, they create neutral clouds around Io's orbit. It is not clear exactly how much of the atmosphere escapes in molecular form versus escaping as clouds of co-orbiting neutral atomic sulfur and oxygen (e.g., Dols et al., 2008, 2012). Oxygen and sulfur atoms in these neutral clouds are finally ionized by interactions with ions, and electrons surrounding Io's orbit and contribute to create the Io plasma torus (IPT) (see reviews by Thomas et al. (2004) and by Schneider and Bagenal (2007)).

Neutral atoms originating from Io are the main plasma source in Jupiter's magnetosphere, and therefore, gaining an understanding of the distribution of oxygen and sulfur in the neutral cloud

is one of the most important issues related to Jupiter's magnetosphere

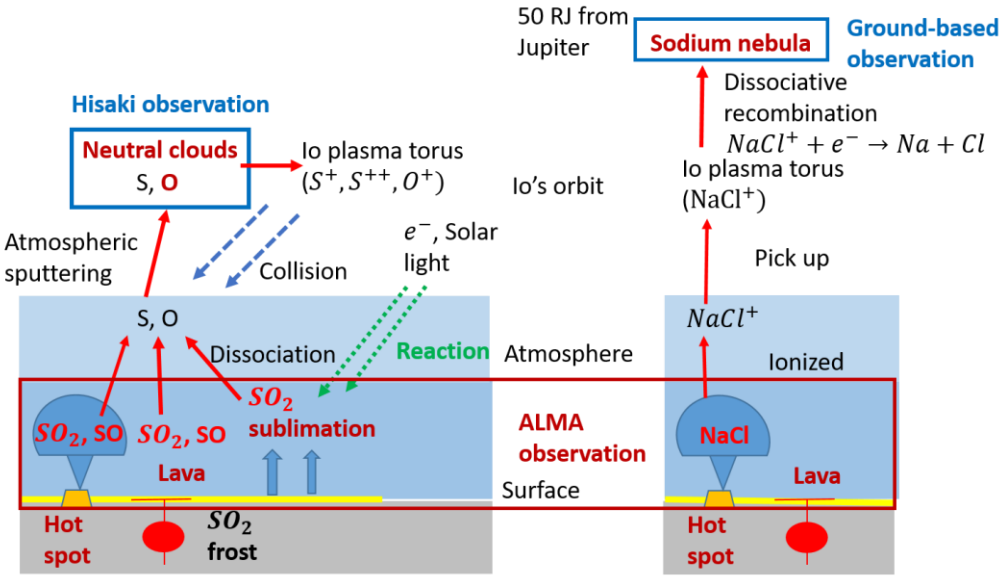

Figure 1.1. Schematic image of generation and escape of Io's atmosphere and neutral cloud.

Table 1.1. Summary of escape processes of neutral materials from Io, and their lifetimes (after Schneider and Bagenal (2007)). Lifetime is calculated under conditions with electron density of 2000 cm^{-3}, and with electron temperature of 5 eV. The mark * shows a fast neutral (several 10's km/s) which leaves from the torus quickly.

Process		Dominant reaction	Lifetime (hours)
Electron impact ionization		$O + e^- \rightarrow O^+$	100
		$S + e^- \rightarrow S^+$	10
		$Na + e^- \rightarrow Na^+$	4
Charge exchange		$O + O^+ \rightarrow O^+ + O^*$	50
Electron impact dissociation		$SO_2 + e^- \rightarrow SO + O$	4
Transport time	(1-6 R_{Io} from Io)	~3 km/s (average)	1
	(~6 R_J from Jupiter)	~3 km/s (initial)	20

1.2 Io's atmosphere

1.2.1 Volcanism and surface composition

Before understanding Io's atmosphere, we need to understand Io's volcanic activities and surface condition. There are three primary types of eruption style listed as follows (Williams and Robert 2007).

1. Flow-dominated (Promethean) eruption (Keszthelyi et al., 2001). It occurs at Prometheus and Amirani. They continuous events for several months and produce extensive lava flow fields through repeated breakouts of lava. SO_2 dominant gases are formed at lava field since hot lava flow vaporize SO_2 frost.
2. Explosion-dominated (Pillanian) eruption (Keszthelyi et al., 2001). It occurs at Pillan, Tvashter, Surt, and Pele. They are short-lived (for days to weeks), but vigorous activity produces both extensive pyroclastic deposits and dark lava flow fields.
3. Intra-Patera (Lokian) eruption (Lopes et al., 2004). It occurs at Loki (the most powerful volcano on Io), Pele, and Emakong. Volcano-tectonic depression occurs lava lake eruption with and without plume that emits SO_2-rich gas like geyser.

We pick up and explain the observation results which relate to this study.

Plume activities

New Horizon approached Io in 2007 and observed dynamics of major plume eruption of the Tvashtar volcano (Spencer et al. 2007). Time series of the plume is shown in Figure 1.3. Center of Tvashtar is near 62°N, 122°W. The image reflected the morphology of the particles that may condense after ejecting from the volcano. The plume height was constant as 320 – 360 km, and its width was about 1100 km. Particle velocities projected on the plane of the sky are 0.4 – 0.7 km/s. The particles speed up when they fall toward the surface.

Geissler et al. (2004) reported observation results of surface changes, plumes and auroral emissions seen in Galileo SSI (Solid State Imaging) images. Moore et al. (2010) classified two volcanic plume type according to size, gas velocity and temperature using the results of Geissler et al. (2004) (Table 1.2). One is Pele type: Large volcanos with a ring radius exceeding ~400 km and shock heights of several hundred km. They assumed Pele type plumes have vent temperature of 650 K, gas velocity of 900 m/s and mass flow rate 1.1×10^4 kg/s. The other is Prometheus type: Smaller volcanoes with a ring radius of ~180 km and shock height of ~120 km. They assumed Prometheus type plumes have vent temperature of 300 K, gas velocity of 500 m/s and mass flow rate of 5.9×10^3 kg/s.

Hot spot distribution

Cantrall et al. (2018) summarized infrared observations of eruptions on the surface of Io using

Keck and Gemini north telescope in 2001-2016, and made the global map of hot spots from the ground. Their map showed there are no significant concentration of detectable hot spot based on hemisphere (leading or trailing, antijovian or subjovian), and distribution of detectable hot spots is random. They observed 18 “persistent” hot spots (detection fraction is over 50 %). Out of 18, 13 persistent hot spots are in the antijovian hemisphere, and 13 persistent hot spots are in the leading hemisphere. Comparison between the hot spot map and ALMA (Atacama Large Millimeter/submillimeter Array) observation of Io’s atmosphere is shown in Section 3.2.

SO_2 frost map

Figure 1.4 shows abundance and grain size of Io’s SO_2 frost (Douté et al., 2001). The locations rich in SO_2 with fine grain frost (shown by green) are always correlated with the most active plumes. The locations are southward of Pele, Pillan and Marduk, and northward in Maui, Amirani, Volund and Zamama. However, the most volcanically active locations around Loki are much depleted in SO_2. Further explanation is shown in the next subsection.

Table 1.2. Active volcanic plume list (Moore et al., 2010). Longitude and latitude is slightly different from Cantrall et al. (2018).

Plume	Longitude, Latitude	Type
Kanehikili	38°W, 16°S	Prometheus
Grian (S. Karei)	16°W, 2°N	Prometheus
Amirani	117°W, 24°N	Prometheus
Tvashtar	125°W, 59°N	Pele
Prometheus	156°W, 2°S	Prometheus
Culann	164°W, 20°S	Prometheus
Zamama	174°W, 18°N	Prometheus
Marduk	210°W, 27°S	Prometheus
Pillan	244°W, 12°S	Prometheus
Pele	256°W, 20°S	Pele
Loki	311°W, 10°N	Prometheus
Dazhbog	302°W, 54°N	Pele
Acala	336°W, 11°N	Prometheus

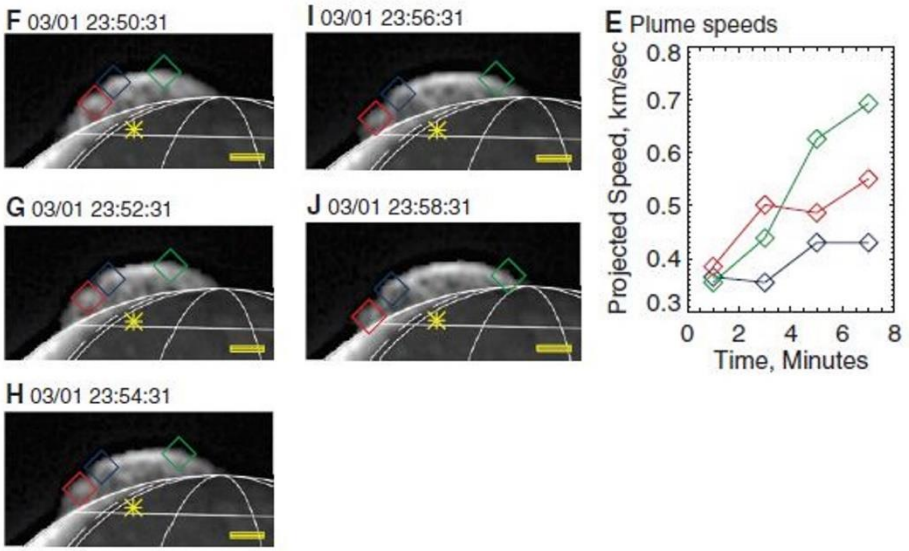

Figure 1.3. (Left) Time series of Tvashtar plume on Io observed by New Horizons (Right) Projected velocity of each diamond of the left figure (Spencer et al., 2007)

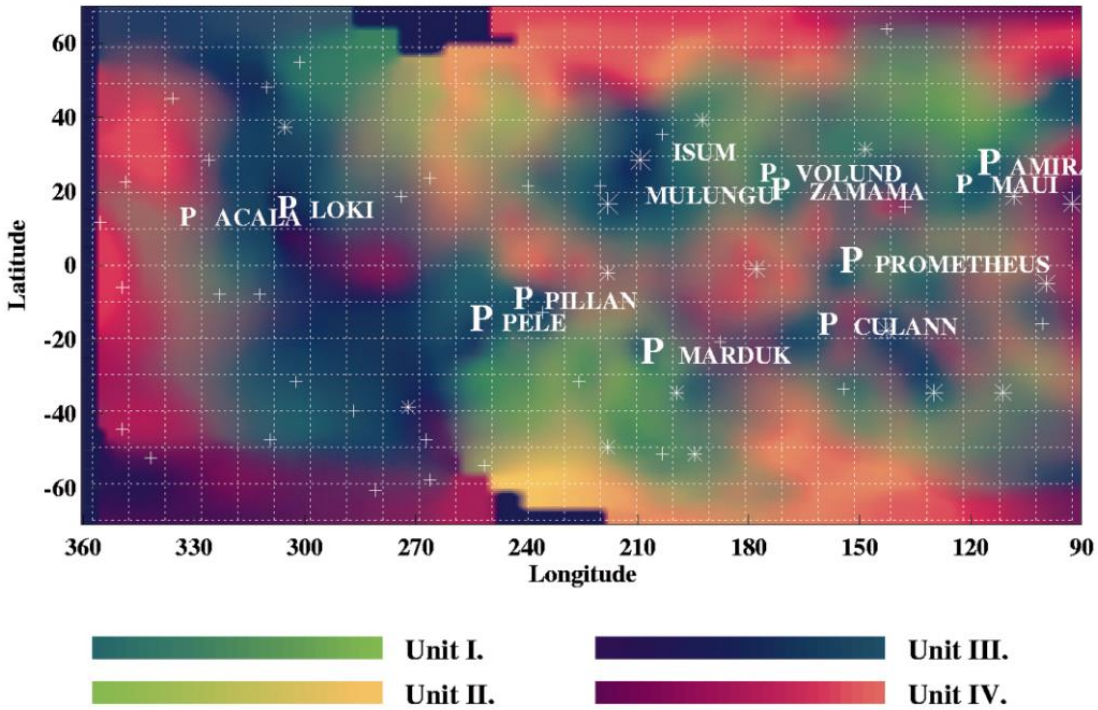

Figure 1.4. Global distribution and granularity of SO_2 frost on Io surface obtained with NIMS (Douté et al., 2001). Unit I indicates rich in SO_2 with fine grain frost. Unit II indicates rich in SO_2 with coarse grain frost. Unit III indicates poor in SO_2 with fine grain frost. Unit IV indicates poor in SO_2 with coarse grain frost. P is the place of the persistent plumes which cloud be the source of SO_2 frost. Stars are the place of the plumes that were not detected in 100 % of the observations.

1.2.2 Horizontal distribution of SO_2 atmosphere

Overview of SO_2 atmosphere

Emission of SO_2 gas was detected for the first time by measuring a rotational line at 222 GHz (Lellouch et al., 1990). According to the data of Lellouch et al. (1990; 1992), the atmosphere is collisionally thick (5×10^{16} - 5×10^{17} cm^{-2}), but the atmosphere covers in limited areas on Io's disk. They and Lellouch et al. (1996) showed Io's trailing atmosphere is very hot (gas temperature T_{atm} = 500-600 K) and much localized (atmospheric coverage f = 5-8 %), and the leading atmosphere is cooler (250-400 K) and more extended (12-16 %). Lellouch et al. (2000) also showed the similar tendency (T_{atm} = 400 K, f = 8 % on the trailing side and T_{atm} = 200 K and f = 24 %). In this subsection, we introduced observation and modeling studies in case that sublimation dominantly support the atmosphere and that volcanic inputs cannot be ignored.

Sublimation support

Jessup et al. (2004) showed the SO_2 gas distribution falling off smoothly as a function of latitude or solar zenith angle (SZA) (see Figure 1.5). It is because the surface temperature changes by latitude and SZA, and SO_2 gases condenses under the low surface temperature. Model calculations of Wong and Johnson (1996), Wong and Smyth (2000) and Smyth and Wong (2004) showed SZA dependence of Io's SO_2 atmosphere. The vapor pressure of SO_2 (P_{vap}) shown by Wagman (1979) and used in previous modeling studies as follows:

$$\mathrm{P_{vap}} = 1.516 \times 10^{13} e^{-4510/T_{surface}} \ \mathrm{Pa}, \tag{1.1}$$

where $T_{surface}$ is the surface temperature. The assumption of the relation between SZA and dayside surface temperature is different in each modeling study. We introduced the assumption used in Smyth and Wong (2000)

$$\mathrm{T_{surface}} = A(cos\theta)^{0.75} + 80 \ \mathrm{K}, \tag{1.2}$$

where θ is SZA ($0° \leq \theta \leq 90°$). They assumed A = 40 K for high density case and A = 33 K for low density case (subsolar temperatures are 120 K and 113 K, respectively).

Moullet et al. (2008) presented the millimeter observation of Io's atmosphere (SO_2 216.643 GHz) with a synthesis beam of 0.5 × 1.5". The observation resolved Io's disk (~1.0") in the longitudinal direction. They observed the Doppler shift due to the atmospheric dynamics. The limb-to-limb difference in the Doppler shift is 330±100 m/s, larger than the equational solid rotation of Io (~75 m/s).

Contribution of direct volcanic eruption

Thickness of local atmosphere also depends on the distance from plume. Lellouch et al. (1996) suggested that the atmosphere of Io is emitted directly from plumes and transported by horizontal wind. Figure 1.4 shows SO_2 frost rich area is near the plumes, which rain SO_2 dust.

It is likely that sublimation of SO_2 frost can easily occur and atmosphere is dense near the plumes (Douté et al., 2001). Figure 1.5 shows the column density of SO_2 sublimation atmosphere near the equator was 1.25×10^{17} cm^{-2}, and there was additional enhancement around Prometheus (5×10^{16} cm^{-2}). It corresponds to a volcanic output of ~10^4 kg/s.

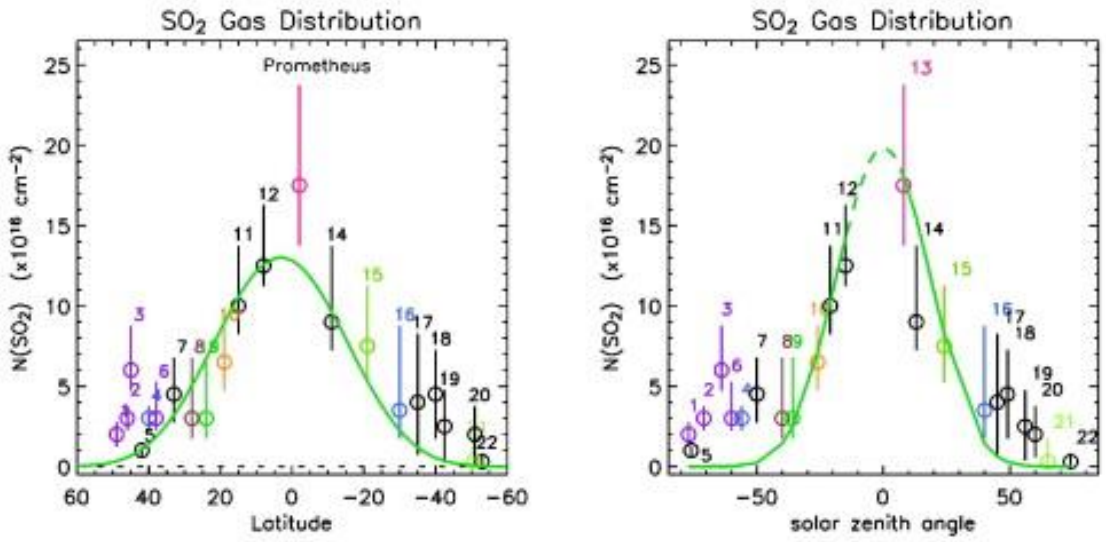

Figure 1.5. (Top) (Bottom) SO_2 gas distribution as a function of latitude and solar zenith angle observed with HST/STIS (the Hubble Space Telescope Space Telescope Imaging Spectrograph) (Jessup et al., 2004). Number shows spectral bins. Colored dots correspond to the locations of observed hot spots, plumes, or lava lakes.

1.2.3 Vertical distribution of SO_2 atmosphere

There is no observational study of vertical density and temperature profile of Io's atmosphere, but are some modeling studies. The calculations of Johnson (1989) and Wong and Johnson (1995) suggested collisional heating by the corotating plasma is important role to determine the height and temperature of Io's exobase. Wong and Smyth (2000) calculated vertical profile of Io's atmosphere in four cases, subsolar points are 120 K and 113 K (high and low density case), and when Io is at eastern and western elongation (the plasma impact Io's nightside and dayside atmosphere). At western elongation in the low density case, plasma collisional heating is contributing near the surface in addition to Joule heating and solar heating. Therefore, temperature increases from the surface to 500 km (~400 – 2300 K). In high density case, Joule heating and solar heating are mainly contributing at lower altitude. The temperature keeps cool below ~70 km (~200 – 300 K) and in turn increases above the altitude that plasma collisional heating takes place (~300 – 2400 K). At eastern elongation, the dayside leading atmospheric temperature is mainly determined by Joule heating and solar heating. Figure 1.6b shows the

temperature in the low density case is much higher than that in the high density case at all latitude, and the temperature in the low density case significantly increases from the surface to 500 km. They also showed the exobase height ranges from 30 to 465 km, and exobase temperature ranges from 220 to 2800 K depending on SZA.

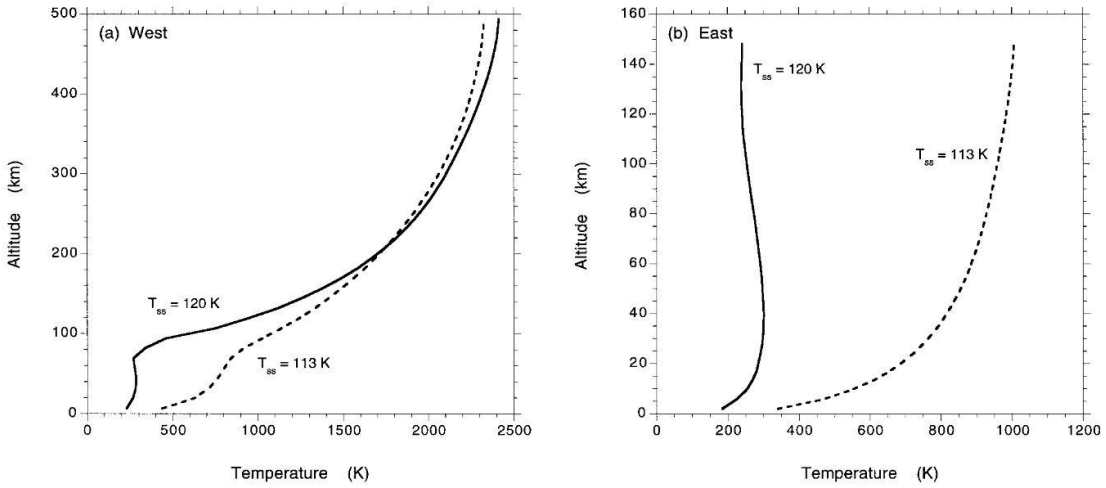

Figure 1.6. Vertical temperature profile at the subsolar point for subsolar temperature 120 K (solid line) and 113 K (dotted line) cases (a) when Io is at western elongation and (b) at eastern elongation (Wong and Smyth, 2000)

1.2.4 Observations of Minor components

SO was first detected by IRAM (the Institut de Radio-Astronomie Millimétrique) 30 m radio telescope (Lellouch et al., 1996). They found the SO/SO_2 mixing ratio of 3-10 %. Primary source of SO had been suspected to be photolysis of SO_2 (ex. Summers and Strobel, 1996):

$$SO_2 + h\nu \rightarrow SO + O \quad (\lambda \leq 219.0 \text{ nm}). \tag{1.3}$$

de Pater et al. (2002) conducted infrared observation of Io's atmosphere during eclipse, and detected the forbidden electronic $a^1\Delta \rightarrow X^3\Delta^-$ transition of SO at 1.71 μm. They estimated the rotational temperature of 1000 K from the shape of SO emission band, and concluded the emission reflects direct ejection of SO molecular from volcanic vents.

Minor atmosphere gases NaCl, KCl were also detected by submillimeter observations. NaCl was first detected by the IRAM (Lellouch et al., 2003). $NaCl/SO_2$ mixing ratio is 0.3-1.3 %. They showed the emission of NaCl varies when Io's central median longitude changes. KCl was tentatively detected by the APEX (Atacama Pathfinder EXperiment) 12 m antenna (Moullet et al., 2013). Moullet et al. (2010) presented the simultaneous submillimeter observation of Io's atmospheric SO_2 (346.652 GHz, 346.523 GHz), SO (346.528 GHz) and

NaCl (338.021 GHz) with a synthesis beam of 0.7-1.0 × 0.7". They showed contribution of direct input from volcanic plume is minor for SO_2, but that is more significant for SO, and volcanic plume is only source of NaCl. The maps of SO_2 and SO, and the first map of KCl are obtained by ALMA (Moullet et al., 2015) (Figure 1.7). They showed SO_2 and SO are distributed widely around Io's disk, but KCl is localized to a smaller area on the disk. KCl is localized mostly around volcanoes, and their amount varies depending on volcanic activities.

$^{34}SO_2$ was only detected by APEX (Moullet et al., 2013). [$^{34}SO_2$]/[$^{32}SO_2$] ratio in Io's atmosphere is 0.065-0.120, larger than the solar system reference $^{34}S/^{32}S$ value of 0.044. The possible cause of the difference are that $^{32}SO_2$ and $^{34}SO_2$ have slightly different vapor pressure, and mass-dependent (isotope) fractionation occurs in sublimation and condensation cycles.

Search for new minor molecular species is one of the most important topics about Io. For example, considerable components such as CO, H_2S, OCS, S_2O, ClO, CS and NaOH have not been detected (Lellouch et al., 2003). Previous ALMA (Moullet et al., 2015) and APEX observations (Moullet et al., 2013) tried and failed to detect SiO submillimeter emissions. Detection of these molecular may progress our understanding of the composition of lava, plume and underground environment.

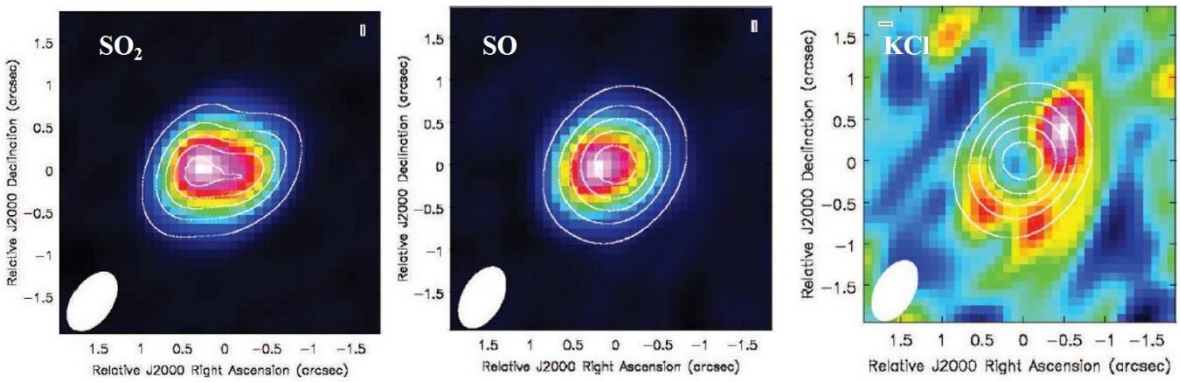

Figure 1.7. Spectral maps of Io's atmosphere of SO_2, SO and KCl emissions in October 2012 observed by ALMA (Moullet et al., 2015). The contour show a synthetic SO_2 distribution (left) and continuum emissions from Io's surface (middle and right). White oval shows the beam size.

1.2.5 Eclipse observations

During the period of Io's eclipse of Jupiter (Figure 1.8a), the observations were carried out to evaluate the importance of volcanism to sublimation for the generation of Io's atmosphere. The total brightness of atomic oxygen emission at 135.6 nm in eclipse decreased compared with that out of eclipse (Clarke et al., 1994; Retherford 2002). They suggested that the brightness change was caused by rapid decrease of Io's surface temperature during eclipse that is probably sufficient to diminish the sublimation component of atmosphere. During the New Horizon's Jupiter flyby in 2007, the spacecraft observed the Io's aurora in eclipse (Retherford et al., 2007). Auroral brightness and morphology on the dayside hemisphere varied after eclipse ingress and egress (Figure 1.8b). They compared the Io's auroral observation with the simulation of Io's UV aurora changing during and after the eclipse (Saur and Strobel, 2004), and found that the volcanic supply of the dayside atmosphere is minor (1 - 3 %).

Observations of Io's tenuous lower atmosphere using HST (Hubble Space Telescope) showed the atmospheric density of SO_2 changes only within 15 % after egress, which implies the importance of volcanic support in the Jupiter-facing hemisphere (Tsang et al., 2015). However, Tsang et al. (2016) observed time series of absorption band at 19 μm of Io's SO_2 atmosphere in eclipse by the Gemini-north telescope with the Texas Echelon Cross Echelle Spectrograph (TEXES), and estimated the atmospheric column density drops by a factor of 5±2 from pre-eclipse to in-eclipse (Figure 1.8c). The result implies Io's atmosphere is mainly supported by sublimation before ingress, and that is mainly supported by volcanism after ingress.

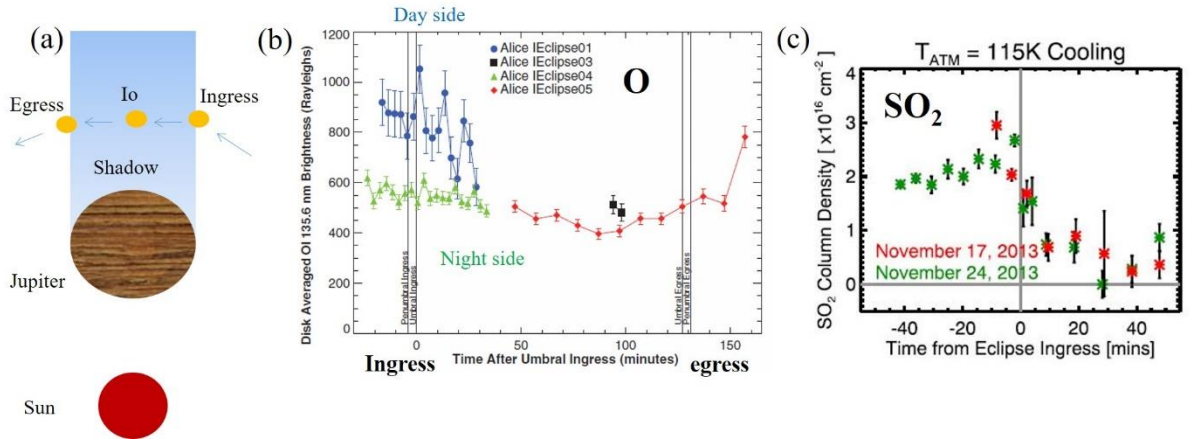

Figure 1.8. (a) explanation of Jupiter eclipse (b) Time series of 135.6 nm Io's auroral emissions in Eclipse observed by New Horizon/Alice (Retherford et al. 2007) (c) Time series of SO_2 column densities observed by Gemini – TEXAS at 19 μm (Tsang et al., 2016)

1.3 Observations of neutral sodium originated from Io

1.3.1 Io's sodium corona

The emission from Io was first detected at sodium D-lines at wavelengths of 589.0 nm and 589.6 nm (Brown and Chaffee 1974). Sodium D-line emissions are produced by resonant scattering of sunlight, and therefore, its brightness faithfully reflects the column density of sodium atoms. Scattering cross section of sodium atom is large enough to be able to observe from the ground. For this reason, sodium D-line emissions have been monitored as a tracer of neutral particles emitted from Io (Yoneda et al., 2015 and references therein).

Figure 1.9 (left) shows schematic diagram of Io's corona and extended clouds. Some of the escaping atoms remain close to Io in a corona inside the Lagrange sphere (<5.81 R_{Io} (where R_{Io} = 1,821.6 km)), where Io's gravity is significant. Some of the neutral atoms form extended clouds (>5.81 R_{Io}), in the region where Jupiter's gravity is dominant. Schneider et al. (1991) measured Iogenic sodium absorption lines in the reflectance spectra of Europa. They showed radial profile of sodium column density in the corona region 1.4-5.6 R_{Io} (Figure 1.9 (right)). The best fit profile was:

$$\mathrm{N(r > 1.4)} = 2.6 \times 10^{12} \times r^{-2.48} \ \text{sodium atoms cm}^{-2} \quad (1.4)$$

where r is the impact factor of Io radii. They also searched for temporal variability of the corona and showed there was no statistical difference during eclipse. They concluded the profile of the corona is symmetric.

Unlike sodium D-lines emissions, spatial and temporal changes of electron density have effects on atomic sulfur and oxygen emissions brightness. However, assuming that electron impact excitation is caused by electrons uniformly distributed in the plasma torus, the emission profiles of atomic oxygen (135.6 nm) and sulfur (147.9 nm) reflect the neutral column density along the line-of-sight, which is expected to be similar to the profiles of neutral sodium. They can be represented as power-law in the radial corona region between 1.4-4.0 R_J (Wolven et al., 2001).

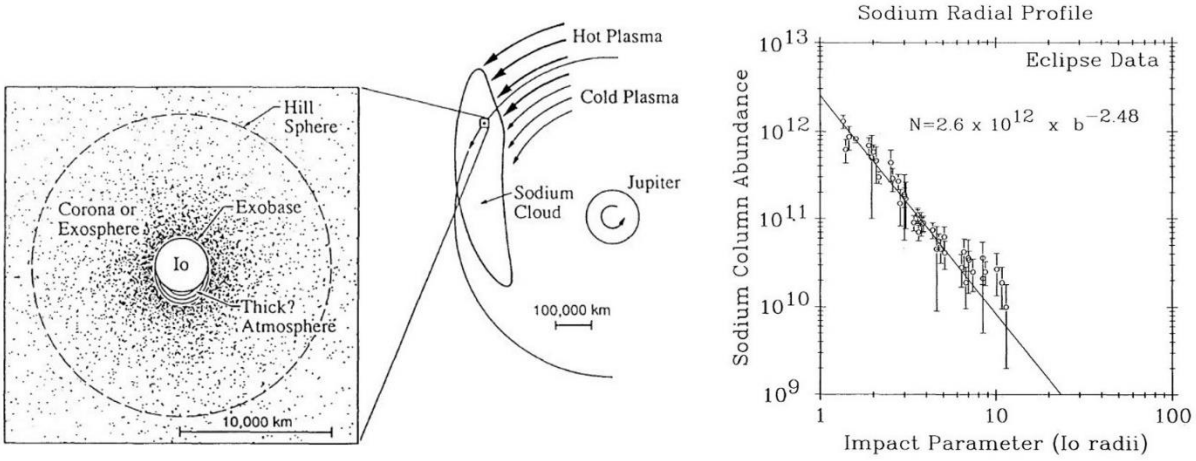

Figure 1.9. (Left) Schematic diagram of Io's exobase, corona and extended cloud (Schneider et al., 1991). Distribution of corona is shown in dots. Dash line show Hill sphere (the effective limit of Io's gravity). (Right) Radial distribution of the sodium corona (Schneider et al., 1991).

1.3.2 Extended sodium neutral cloud

Sodium atoms distributed around Io's orbit and form a structure called banana (b-cloud). The process making sodium cloud is thought to be mainly caused by atmospheric sputtering (Wilson et al., 2002). Most of the neutrals escape speed ejected by sputtering is only few km/s. Sodium clouds therefore extend approximately along Io's orbit (Thomas et al., 2004). Murcray and Goody (1978) observed sodium cloud emission rapidly varies as a function of Io phase angle. They concluded the sodium cloud distributed forward from Io and slightly inside the Io torus.

Smyth and Combi, (1988, 1997) showed detail explanation of two types of the source velocity distribution from Io's exobase (Figure 1.10). They also compared the observation of sodium corona and cloud with the model of source velocity distribution. The Maxwell-Boltzmann flux distribution ($\phi(\mathrm{v};\mathrm{T})$) is defined as

$$\phi(\mathrm{v};\mathrm{T}) = \phi_0 \left(\frac{R_S}{R_E}\right)^2 \frac{2}{v_T} e^{-\left(\frac{v}{v_T}\right)^2}, \tag{1.5}$$

where $\mathrm{v_T} = \sqrt{2kT/m}$ is the most probable velocity of the velocity distribution of atoms (m is the mass of atom), $\mathrm{R_S}$ is the satellite radius, $\mathrm{R_E}$ is the exobase radius, ϕ_0 is the local velocity integrated distribution. The velocity distribution only depends on the exobase temperature T.

The model using the speed distribution did not match the observed profile of both forward and trailing cloud (6-100 $\mathrm{R_{Io}}$), where the slope is milder than the corona and asymmetric. This behavior indicates there is the high velocity population which is not included in the Maxwell Boltzmann flux distribution.

Then they also considered the modified sputtering flux distribution, which represents

the composite effects of heating below the exobase and ion sputtering of the atmosphere. The velocity distribution ($\phi(\mathrm{v};\alpha,\mathrm{v_b},v_M)$) is defined as:

$$\phi(\mathrm{v};\alpha,\mathrm{v_b},v_M)=\phi_0\left(\frac{R_s}{R_E}\right)^2\frac{1}{v_b D(\alpha,v_M/v_b)}\left(\frac{v}{v_b}\right)^3\left(\frac{v_b^2}{v^2+v_b^2}\right)\left[1-\sqrt{\frac{v^2+v_b^2}{v_M^2}}\right], \tag{1.6}$$

where $\mathrm{D}(\alpha,v_M/v_b)$ is a normalization constant (see Smyth and Combi, 1988). The velocity distribution depends on the two velocity parameters $\mathrm{v_M}$ and $\mathrm{v_b}$, and the exponent α which primarily determines the dispersion. $\mathrm{v_M}$ is represented as

$$\mathrm{v_M}=\frac{2M}{M+m}v_R, \tag{1.7}$$

where $\mathrm{v_R}$ is the relative velocity, M and m are mass of ions and atoms. There is non-linear relation between the most probable velocity $\mathrm{v_m}=\sqrt{3kT/m}$ and $\mathrm{v_b}$ represented as

$$\mathrm{v_b}=v_m\sqrt{\frac{2}{3}\alpha+\frac{1}{3}\xi-1}, \tag{1.8-1}$$

$$\xi=\left[\frac{v_M}{\sqrt{v_m^2+v_b^2}}-1\right]^{-1}, \tag{1.8-2}$$

The observation of both the corona and extended cloud was best fitted by the velocity distribution whose peak speed is 0.5 km/s (well below the exobase escape velocity of 2 km/s), and parameter α = 7/3. In this situation, collisional cascade process that moves energy from the speed tail to the lower speed core occurs, but it is not complete (Smyth and Maconi, 2003). About 62 % of the source atoms for this distribution cannot escape beyond corona, while the remaining 38 % can move to neutral clouds (Smyth, 1998; Smyth and Marconi, 2003). High velocity (several 10's km/s) atoms ejected from Io (tail component of atmospheric sputtering and charge exchange) also exist. They move quickly inward and outward from Io's orbit and contribute primary to the neutral clouds at much larger and smaller jovicentric distances.

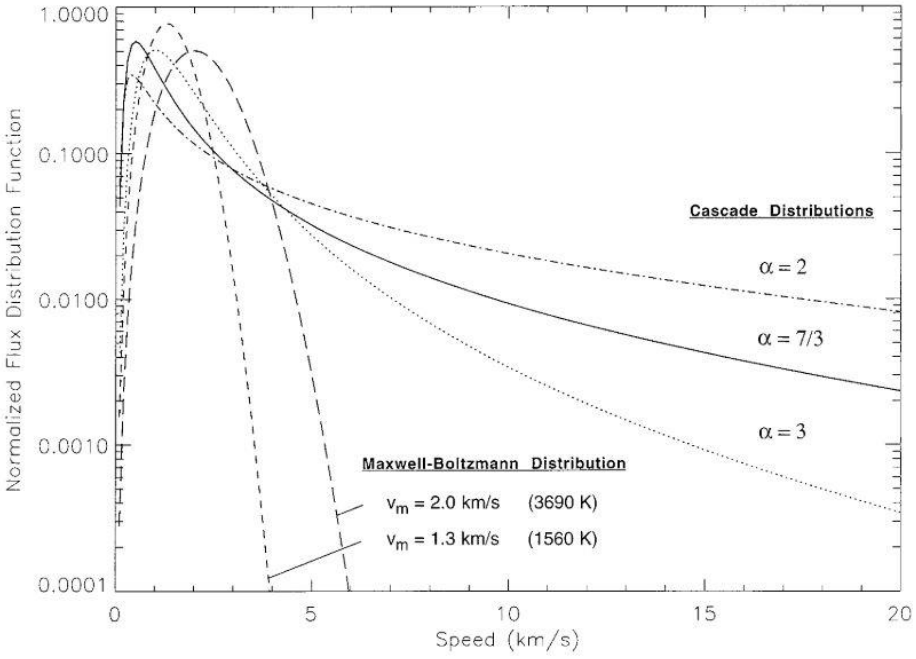

Figure 1.10. Flux velocity distribution function for sodium at Io's exobase. V_m is most probable speed (Smyth and Combi 1997). Most probable speed of cascade distribution is V_m = 1.0 km/s for α = 3, 0.5 km/s for α = 7/3, 0.4 km/s for α = 2.

1.3.3 Sodium nebula

Mendillo et al. (1990) reported the extended sodium nebula spread up to 500 R_J centering at Jupiter. Escape process of atomic sodium outside the Io torus is thought to be dissociation and dissociative recombination of sodium bearing molecular ions in the torus with electron (Wilson and Schneider 1994) as expressed by

$$\mathrm{NaX}^+ + e^- \rightarrow \mathrm{Na}^* + X^- + e^-, \qquad (1.9-1)$$

$$\mathrm{NaX}^+ + e^- \rightarrow Na^* + X^*. \qquad (1.9-2)$$

Though NaX^+ is not identified completely, $NaCl^+$ is a strong candidate because of observation of Cl^+ (Kuppers and Schneider 2000), and direct detection of NaCl (Lellouch et al., 2003). Molecular ions (NaX^+) are picked up by the Jupiter's corotating magnetic fields from the Io's ionosphere.

In the vicinity of Io, it is difficult to observe sodium D-line emissions because the sodium emission near Io is hardly distinguished from very strong sunlight reflection at Io surface. Sodium D-line emissions outside Io torus (approximately 5-150 R_J) are therefore used to monitor the variation of neutrals. Mendillo et al. (2004) showed that both sodium D-line brightness and Io's 3.5 μm infrared brightness are correlated (see Figure 1.11). Considering that the infrared brightness probably reflects the volcanic activities on Io, this fact suggests that

we can monitor Io's volcanic activity by observing the time variation of sodium emissions remotely from the ground. However, de Kleer et al (2019) suggested that there is no significant correlation between activity of Loki Patera and SO gases from observations of an emission band at 1.707 μm (Figure 1.12). The relations between place, types and activities of Io's volcanoes and their amount of emitting gases, or contribution of generating the atmosphere, are still poorly understood.

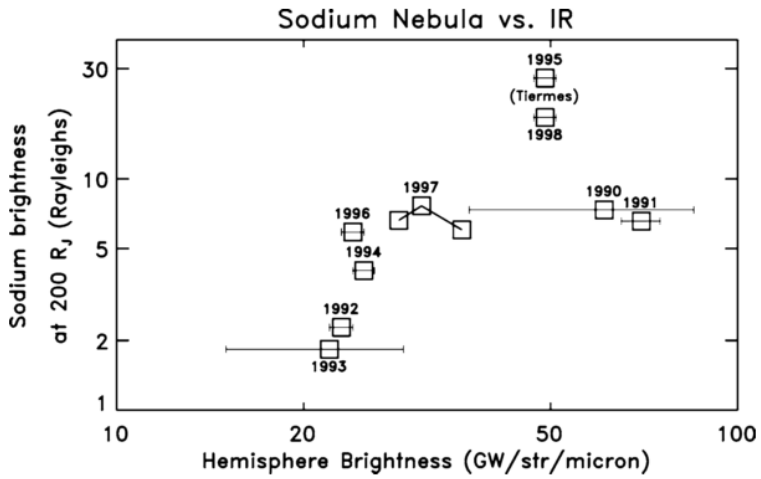

Figure 1.11. Correlation between of Io's sub-Jovian hemispheric brightness of infrared emission at 3.5 μm and the brightness of sodium nebula emission obtained at a distance of 200 R_J from Jupiter (Mendillo et al., 2004).

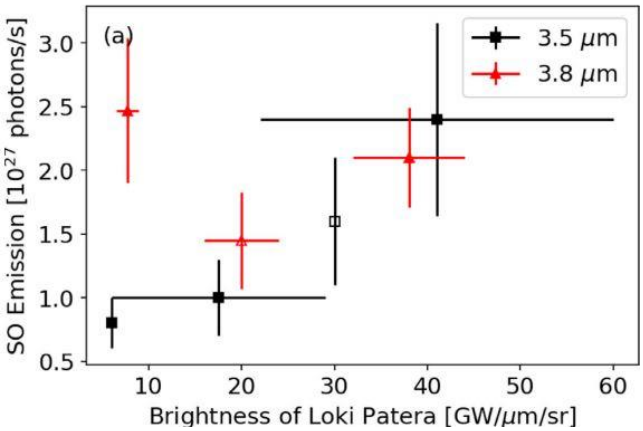

Figure 1.12. Correlation between total measured SO emission and infrared brightness at Loki Patera (de Kleer et al., 2019).

1.4 Neutral oxygen corona and cloud

1.4.1 Observations of neutral oxygen emission

Neutral atomic oxygen has been detected near Io via ground-based optical observations (Brown, 1981; Oliversen et al., 2001; Scherb & Smyth, 1993; Thomas, 1996) from ultraviolet (UV) emissions (Durrance et al., 1983, 1995; Roesler et al., 1999; Wolven et al., 2001) (Table 1.3). However, the detailed distribution of the oxygen and sulfur neutral clouds beyond the Lagrange sphere has not yet been directly measured because of their faint emissions.

Atomic oxygen emissions from Io's neutral cloud at the wavelength of 630.0 nm were first detected by ground-based observations with a brightness of 8±4 Rayleighs (R) (Brown, 1981). They deduced the atomic oxygen number density in the Io torus as 30±15 cm^{-3} assuming electron density is 2000 cm^{-3}. Atomic oxygen emissions at 630.0 nm from the neutral cloud were also detected by Thomas (1996). The peak brightness they found was 8.8±1.7 R, which is consistent with Brown (1981). Further observations of these optical emissions close to Io by Oliversen et al. (2001) between 1990 and 1999 showed substantial variations with local time, Io phase and longitude.

Atomic emissions can be detected farther from Io in the UV. Atomic sulfur emissions at 142.9 nm (2.5±1.2 R) were first discovered with rocket-borne Faint Object Telescope (FOT) observations (Durrance et al., 1983). In these observations, atomic oxygen emissions at 130.4 nm (3.6±2.0 R) were also detected. Skinner and Durrance (1986) estimated that the lower limits of atomic oxygen and sulfur number densities in regions of the torus far from Io are $n_O > 29±16$ cm^{-3} and $n_S > 6±3$ cm^{-3}, respectively, based on the observations of Durrance et al. (1983). Atomic sulfur emissions from the Io torus at 142.9 nm were also detected by the Hopkins Ultraviolet Telescope (HUT) (Durrance et al., 1995). In that study, the authors estimated that only 33% of the sulfur emissions measured by HUT were from Io, and the rest of the emissions were inferred to be from a diffuse neutral sulfur component of the torus. They also estimated the number density of atomic sulfur from the Io torus to be in the range of 2-12 cm^{-3}. Wolven et al. (2001) used 30 observations by the Hubble Space Telescope Space Telescope Imaging Spectrograph (HST/STIS) of OI at 135.6 nm in the UV extending out to 10 R_{Io} where the brightness dropped below 10 R (Figure 1.13). They also showed that emissions downstream of Io tended to be brighter than those upstream, that the local time (dawn vs. dusk) asymmetry depends on the Io phase angle.

Scherb and Smyth (1993) and Oliversen et al. (2001) showed that Io's orbital phase (θ) and System III of longitude (λ) dependence of Io's atomic oxygen emission at 630.0 nm. Figure 1.14 shows the dependence of brightness of the emission at 630.0 nm on the Io's System III longitude for the dawn side and dusk side, respectively (Oliversen et al., 2001). The average brightness of emission peaks at 630.0 nm in the range of $\lambda = 90°$ and 290° on the dawn side,

and λ = 130° and 290° on the dusk side, respectively. The System III dependence is probably caused by the electron density variation due to about 7° tilted angle of the plasma torus to Io's orbital plane as well as about 0.1 R_J offset of magnetic dipole moment with respect to the rotational axis of Jupiter. This figure also shows Io's brightness of atomic oxygen emission at 630.0 nm in the dawn side is larger than that in the dusk side for all of the System III longitude range. Wolven et al. (2001) also showed that the mean atomic oxygen (135.6 nm) and sulfur (147.9 nm) brightness near λ = 130° (Orbit 3 in Figure 1.14) is larger than that near λ = 40° (Orbit 1) in both inner region (0 R_{Io} < R < 2 R_{Io}), and outer region (2 R_{Io} < R < 6 R_{Io}).

Table 1.3. Summary of observations of neutral oxygen corona and cloud.

Wavelength (nm)	Instruments	Slit position	Intensity (R)	Reference
630.0	Ground	1-5 RJ ahead from Io	8±4	Brown 1981
130.4	Rocket	IPA 180° far from Io	4.2±2.0	Durrance et al., 1983
630.0	Ground	5.2"×5.2" centered on Io	5-25 kR	Scherb & Smyth, 1993
630.0	Ground	Within 0.5 RJ from Io	8.8±1.7	Thomas 1996
130.4 135.6	STIS/HST	Io is in the slit		Roesler et al., 1999
135.6	STIS/HST	0-7 R_{Io} from Io	10-1000	Wolven et al., 2001

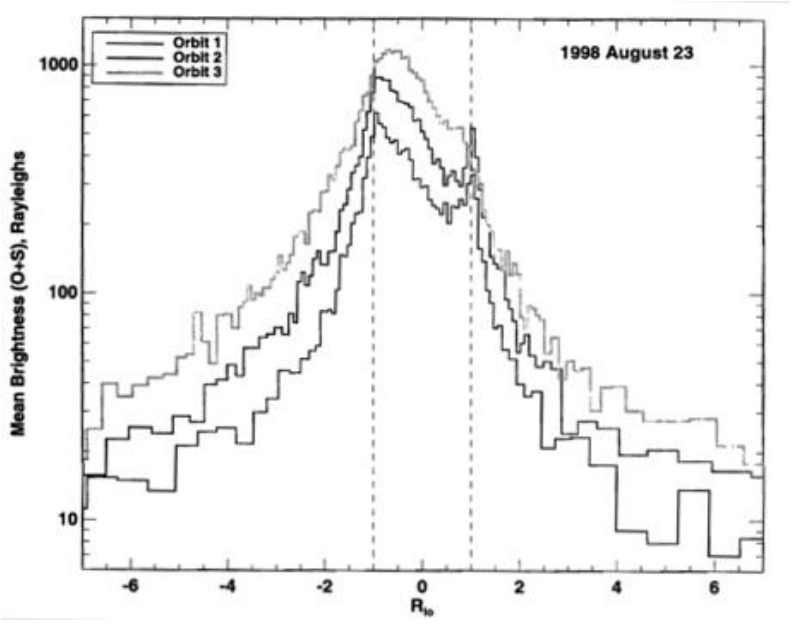

Figure 1.13. Examples of spatial distribution of oxygen and sulfur emissions at 135.6 nm and 147.9 nm obtained with HST/STIS. Orbit 1 to 3 indicates when Io's System III longitude are about 40°, 90° and 130°. Horizontal axis shows the distance from Io (Io radii) (Wolven et al., 2001).

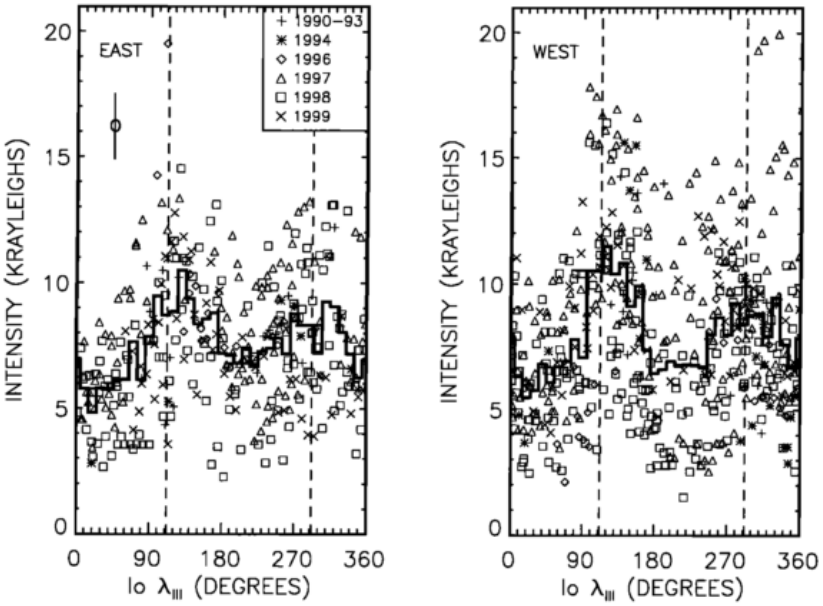

Figure 1.14. Dependence on brightness of atomic oxygen at 630.0 nm on the System III longitude. West and east indicate dawn side and dusk side, respectively. The mean error in brightness is 1.3 kR (Oliversen et al., 2001).

1.4.2 Neutral cloud model

Modeling studies resolved the detailed spatial structure of neutral oxygen and sulfur clouds in the Io torus (e.g., Burger (2006); Smyth and Marconi (2003)). According to the modeling study of Smith and Marconi (2003), the nominal lifetime of oxygen and sulfur atoms in the plasma torus at Io's orbital distance are 18 hours and 9 hours, respectively. These lifetimes are much shorter than characteristic orbital dynamic time to form complete 360° toroidal cloud around Jupiter (250 hours). Thus, they suggested that atomic oxygen column density of neutral cloud near Io is more than 10 times denser than that on the other side of Io (Figure 1.15). They also showed that sulfur and neutral oxygen clouds spread inward of Io's orbit and forward of Io, and the density rapidly decreases in trailing of Io. It is because the plasma density and temperature inside Io's orbit is smaller than those outside Io's orbit, and therefore the neutral loss rate there became smaller. On the other hand, Burger (2006) used in the model the lifetime of atomic oxygen which is longer than that of Smyth and Marconi (2003), and therefore, neutral oxygen cloud distributes almost uniformly around the Io torus. They examined the comparison between neutral cloud model of oxygen and that of sodium (Figure 1.16). Neutral oxygen cloud is much denser than the sodium neutral cloud, although it is governed by similar dynamics. Since the lifetime of atomic sodium in Io's orbit is much shorter than that of atomic oxygen, distribution of sodium neutral cloud is limited near Io compared to the neutral oxygen cloud. Thomas et al. (2004) also compared distribution of neutral clouds and Io plasma torus (Figure 1.17). They mentioned the longer lifetime species (S and O) are more extended from Io than other easily dissociated or ionized species (SO_2, SO and Na), and Io plasma torus distributes uniformly surrounding Jupiter because of its longer lifetime. Smyth and Marconi (2003) also shows radial distribution of neutral oxygen and sulfur cloud (Figure 1.18). The slopes inside Io's orbit is milder than that outside Io's orbit because of the presence of the forward cloud mainly spreading inside Io's orbit.

Distribution of neutral clouds also reflect ejection process from Io's exobase. We already explained the velocity distribution which can explain the sodium observation in subsection 1.3.2. Figure 1.19 shows the trajectory of atoms ejected from Io (Burger 2006). Atoms ejected from Io in the forward direction move outward from Io's orbit. Then, they slow down relative to Io and make up the trailing cloud. Atoms ejected from Io in the backward direction move inward from Io's orbit. Then, they speed up relative to Io and make up the forward cloud.

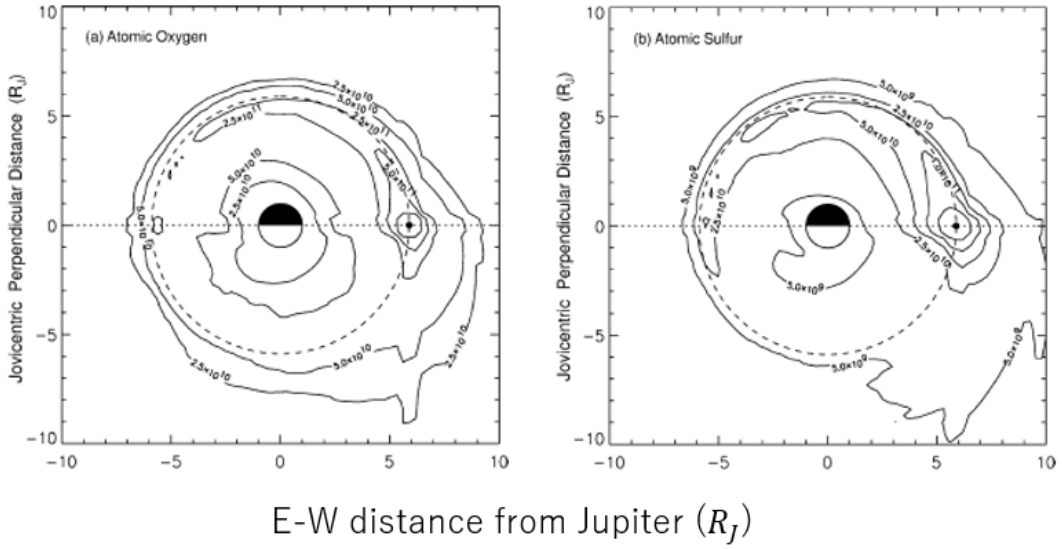

Figure 1.15. Distribution of oxygen (left) and sulfur neutral clouds (right) around Io's orbit obtained with a modeling (Smyth and Marconi 2003).

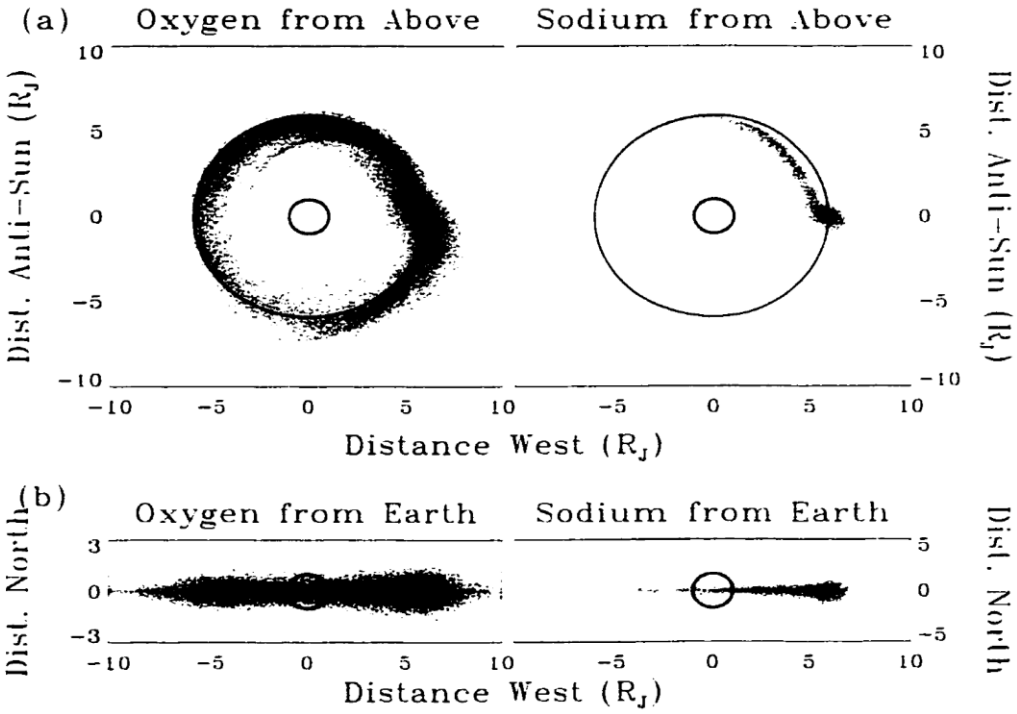

Figure 1.16. (a) Oxygen and sodium neutral clouds seen above Jupiter. (b) Same as (a) but seen from the Earth (Burger 2003).

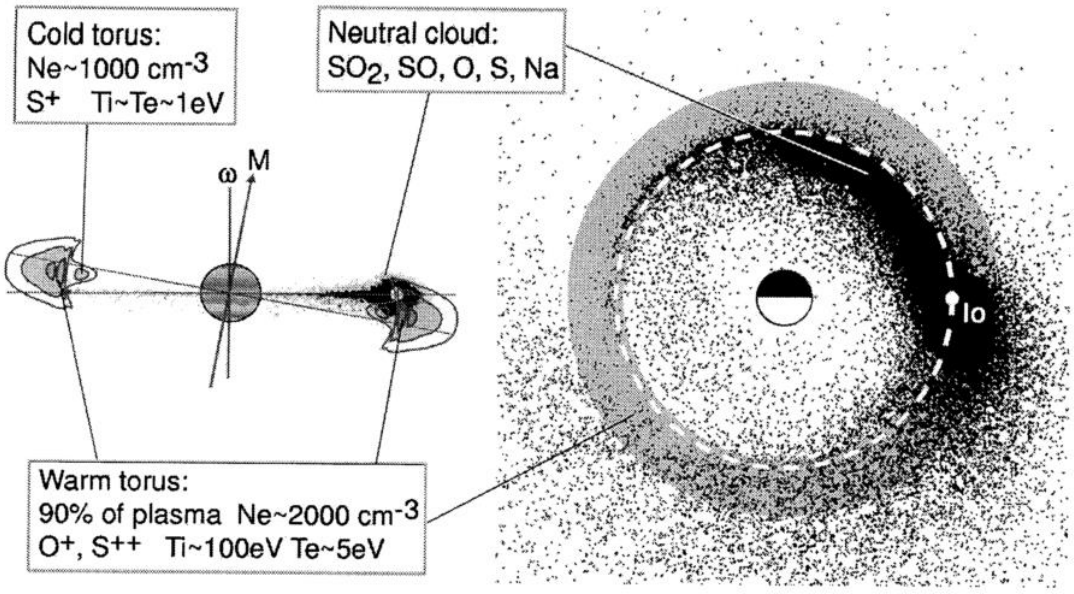

Figure 1.17. (left) Schematic image of neutral clouds and Io plasma torus seen from Central median longitude of 290°. (Right) Same seen from Jupiter's north pole. Both figures are reviewed by Thomas et al (2004). The plasma torus is tilted 9.6° from Io's orbit plane. The shape of neutral clouds varies between species. The longer lifetime species (S and O) are more extended from Io than other easily dissociated or ionized species (SO_2, SO and Na)

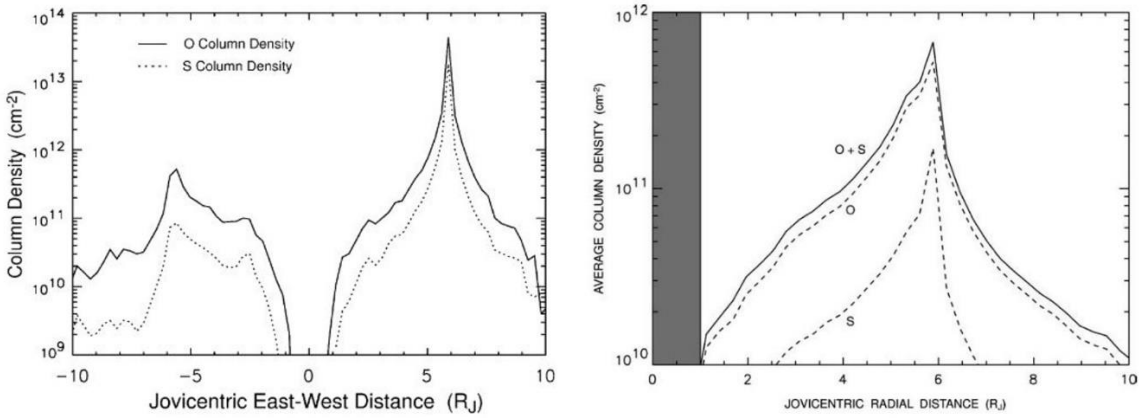

Figure 1.18. Radial profile of O and S in the torus (Smyth and Marconi, 2003). (Left) Column density profile along the horizontal dash lines in Figure 1.15. (Right) Average radial profile which is obtained by longitudinally integrating their two-dimensional distribution in Figure 1.15.

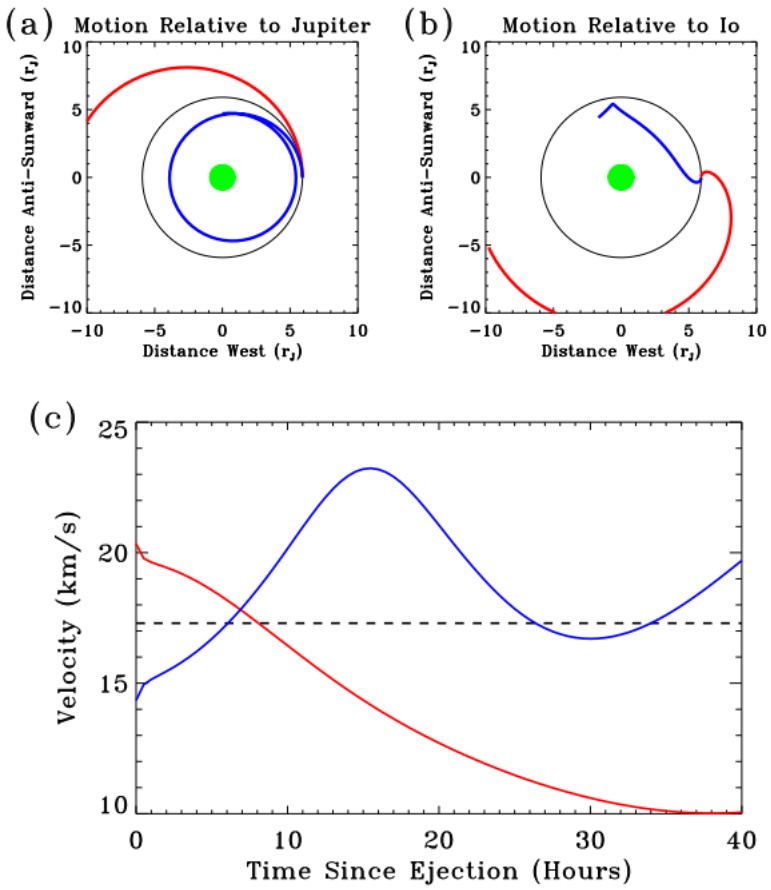

Figure 1.19. Trajectory of atoms ejected from Io modeled by Burger (2003). Red line is ejected in the forward direction, and blue line is ejected in the backward direction. Both initial velocity is 3 km/s. (a) Trajectory relative to Jupiter seen from above. (b) Trajectory relative to Io. (c) Relative revolution of the atoms relative to Jupiter.

1.5 Time variability of neutral and plasma torus

1.5.1 Observations before Hisaki era

Brown and Bouchez (1997) monitored sudden increase in Na brightness (a huge spike in several days) with ground-based observations, and also monitored gradual increase of S^+ brightness (over 30 days) in the same period (Figure 1.20). They argued that the difference of Na and S^+ increases is because the lifetime in the neutral cloud (less than a day) is shorter than the plasma lifetime (about 50 days). Yoneda et al. (2010) also observed increased Na emission with an ambiguous increase of S^+ brightness on the dusk side (Figure 1.21). The rate of the increase of Na observed by Yoneda et al. (2010) was much smaller than that observed by Brown and Bouchez (1997). There was no simultaneous observation of the same particle species, such as O and O^+, in the torus.

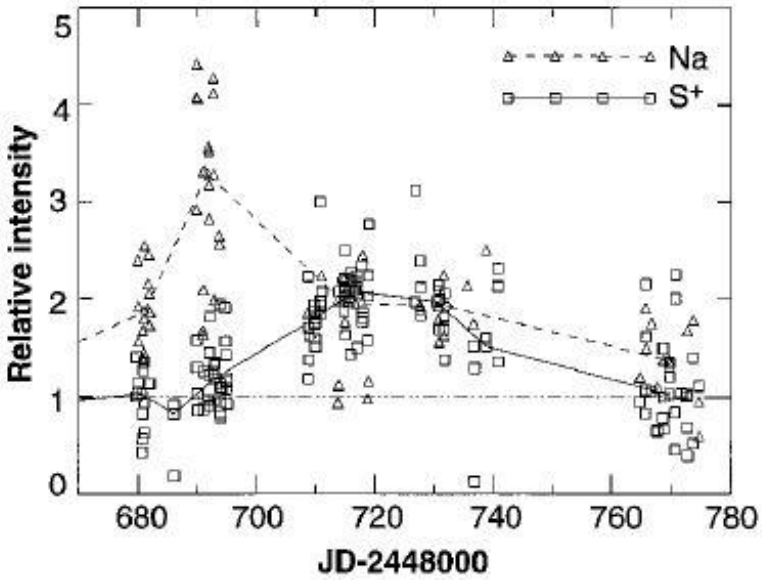

Figure 1.20. Time variations of Na (triangle, dash line) and S^+ (square, solid line) in the same period (Brown and Bouchez, 1997).

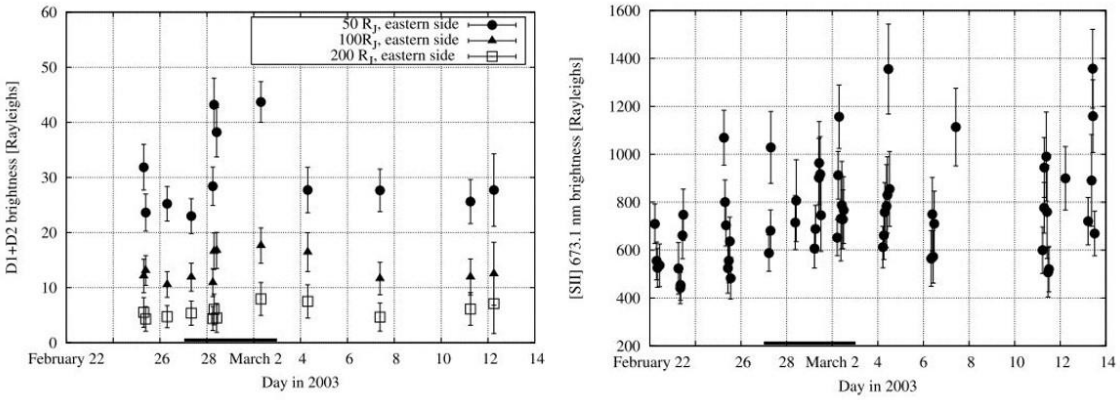

Figure 1.21. (Left) Time variations of Na nebula at 50 R_J, 100 R_J and 200 R_J from Jupiter. (Right) That of S^+ in the torus (Yoneda et al., 2010).

1.5.2 Observations during Hisaki era (2013-)

Hisaki observed IPT and Jupiter aurora continuously since December 2013, and observed large increase of neutral oxygen and oxygen and sulfur ions in the torus in the spring of 2015. Overview of the results are shown in Figure 1.22 (Tsuchiya et al., 2018). They showed OI 130.4 nm, OII 83.4 nm, SII 76.5 nm, SIII 67.9 nm started to increase in the middle of January, and SIV 65.7 nm started to increase over one month later. Kimura et al. (2018), Hikida et al. (2019), Tao et al. (2018), Tsuchiya et al. (2019), Yoshikawa et al. (2017), and Yoshioka et al. (2018) also showed the change of IPT in 2015. They interpreted that the enhancements in neutral and IPT emissions were caused by changes of Io's volcanic activity. de Kleer and de Peter (2016) observed a brightening of 3.8 μm emission from Kurdalagon Patera in late January in 2015 (Figure 1.23) which was consistent with the brightening of sodium emission observed by Yoneda et al. (2015).

Hisaki also observed IPT from January to August 2016. Tsuchiya et al (2019) showed SII 76.5 nm and SIII 68.0 nm started to increase from the middle of July 2016 (SIV 65.7 nm was stable, and OII 83.4 nm was not plotted because their integration time was short). However, there is no observation of infrared and sodium nebula emissions in the same period. Morgenthaler et al. (2019) observed the change in intensity of sodium nebula emission from February to May in 2018 (Figure 1.24). IPT on the dusk side also increased in the same period (Kita et al., 2019, private communication). There was no observation of infrared emission in the same period. We discussed the relation between Io's atmosphere and their variations (Na and IPT) in section 3.4.

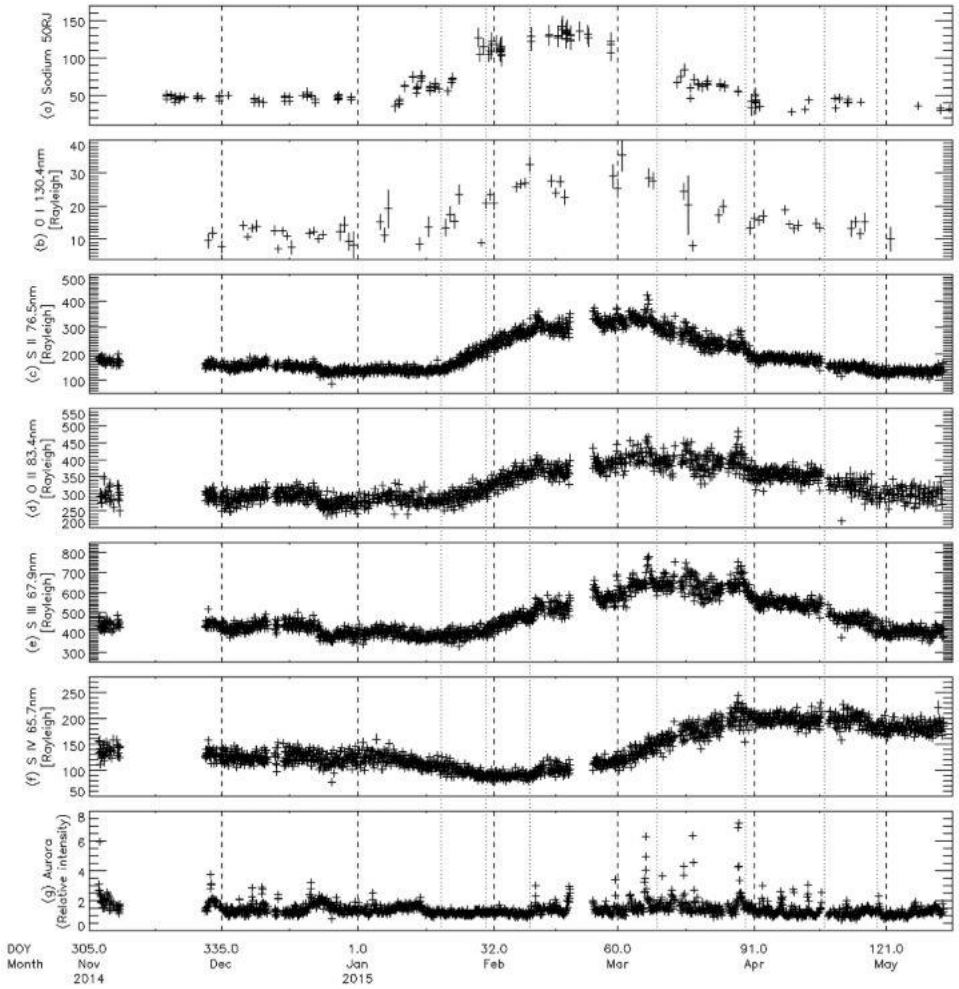

Figure 1.22. The Hisaki and ground-based observations of sodium nebula (a), neutral oxygen cloud (b), IPT (c-f) and Jovian UV aurora (g) variability from November 2014 to May 2015 (Tsuchiya et al., 2018).

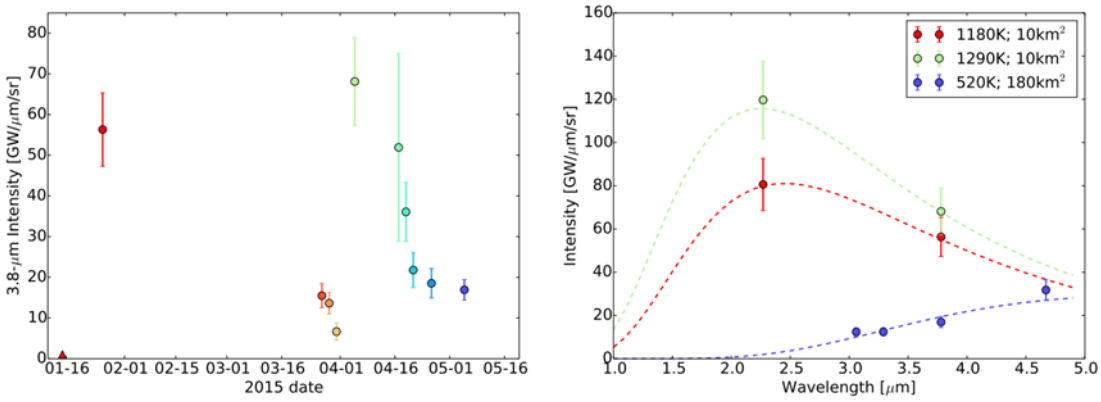

Figure 1.23. (Left) Timeline of 3.8 μm emission at Kurdalagon Patera in 2015 (de Kleer and de Peter, 2016). (Right) Best-fit temperature models on the dates when activity was detected at multiple wavelengths. Colors of points correspond between the two plots.

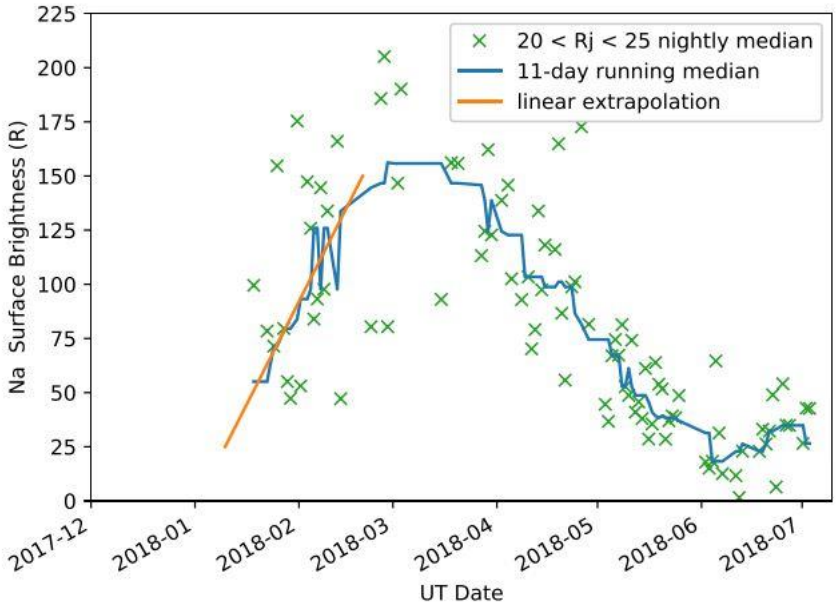

Figure 1.24. Time variation of sodium nebula emission at the range of 20-25 Jupiter radii from Jupiter (Morgenthaler et al., 2019).

1.5.3 Lifetime and radial transport timescale of O^+

Yoshioka et al., (2018) conducted plasma diagnosis using Hisaki EUV-UV observation data during high resolution slit was used. They estimated radial distribution of electron density, core electron temperature, hot electron fraction and density of ions (Figure 1.25). The periods are November 2013 and February 2015, which corresponds to volcanically quiet and active periods. Steffl et al. (2004, 2006, 2008) also conducted plasma diagnosis using Cassini UVIS (Ultraviolet Imaging Spectrograph) data, and showed distribution and temporal variability of electron and ions. Delamere et al. (2003, 2004, 2005) also showed the physical chemistry model of IPT and compared Cassini and Voyager observation results. Combination studies of plasma diagnosis and physical chemistry model can reveal various properties of IPT.

Delamere et al. (2005) estimated radial distribution of time scales of O^+ loss and showed that outward transport is a major loss process. Steffl et al. (2008) showed that the time scales of charge exchange (ex. $O^+ + S \rightarrow S^+ + O$ reaction is over 700 days) are much longer than the time scale of O^+ loss by outward transport (62.0 days). Delamere et al. (2003) showed the change of the outward transport time scales of IPT. They are 50 days during the Voyager 1 and Cassini observations and 23 days during the Voyager 2 observation. Delamere et al. (2004) showed the transport time scales during Cassini observations changed from 27 days in October 2000 to 64 days in January 2001. Yoshioka et al. (2017, 2018) showed the transport time scales of IPT are 34±7 days in November 2013, and 9.9±0.9 days in February 2015. Yoshioka et al. (2018) shows the volcanic activity in 2015 increased the neutral supply rates to IPT by about a

factor of 4.5. They suggested the increase of neutral production rate leads to the increase of electron impact ionization rates, and subsequently leads to heavier mass loading, which drives faster outward transport.

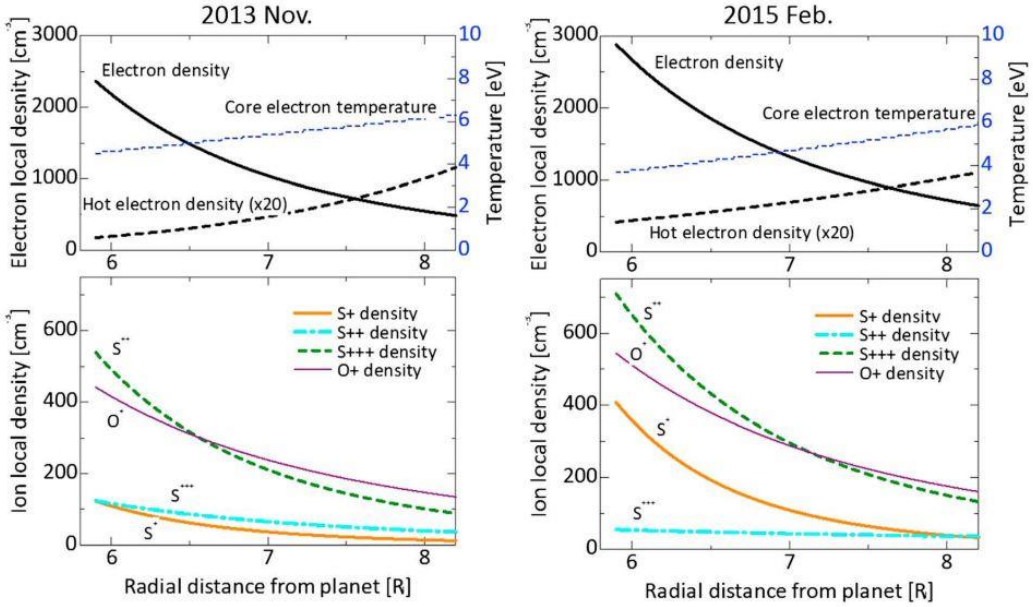

Figure 1.25. Radial distribution of electron density, core electron temperature, hot electron density, and density of S^+, S^{2+}, S^{3+} and O^+ during volcanically quiet (November 2013) and active periods (February 2015) (Yoshioka et al., 2018).

1.6 Purpose of this study

Final goal of this study is to understand the processes from the generation of gasses from geologically active bodies to the escape of the gasses into space. To meet the final goal, we focus on Jupiter moon Io's SO_2 atmosphere and escaped neutral oxygen atoms around Io's orbit. The main purposes are:

1. To discuss contribution of sublimation and direct volcanic eruption to generate Io's atmosphere, and temperature profile of the atmosphere before and after ingress using ALMA archive data. Previous eclipse observations also discuss whether volcanism or sublimation is dominant from the temporal variability of Io's atmosphere. However, they did not resolve Io's disk. Synthesis beam sizes of ALMA observation we used are 0.36" × 0.28" before the ingress, and 0.41" × 0.28" after the ingress. We can study changes of Io's atmosphere with spatially resolved image of Io (see Chapter 3).
2. To study the temporal and spatial variability of the neutral oxygen cloud which have never been observed so far. We did the discussion of Io's atmosphere and neutral and plasma torus and suggested the hypothesis of how the volcanic plume affects the neutral and plasma torus (see Chapter 4).
3. To study source and loss processes of Io oxygen plasma torus from the distribution of oxygen atom shown in Chapter 4 and electron and plasma distribution estimated by Hisaki and Voyager observations (see Chapter 5).

We described instrument information of Hisaki, Tohoku University telescope that observed the sodium nebula and ALMA in Chapter 2. We summarized the whole works in Chapter 6.

Chapter 2 Instruments

2.1 Hisaki/EXCEED

2.1.1 General information

The Hisaki satellite boarding extreme ultraviolet (EUV) spectrograph (EXtreme ultraviolet spectrosCope for Exospheric Dynamics: EXCEED) was launched on 14 September 2013 and started the scientific observation in November 2013 (Yamazaki et al., 2014; Yoshikawa et al., 2014). The Hisaki satellite is space EUV telescope, which aims to observe several planets (Mercury, Venus, Mars, Jupiter and Saturn) to characterize the planetary atmospheres and magnetospheres. Hisaki orbited around the Earth with an altitude between 950 km and 1150 km, an inclination of 29.7°, and a period of 106 min. Table 2.1 shows the major characteristics of the Hisaki satellite and Table 2.2 shows the specification of EXCEED. Yamazaki et al. (2014), Yoshikawa et al. (2014), and Yoshioka et al. (2013) provide detail explanations of the instrument and its performance.

A dumbbell-shaped slit with blank filter has been regularly used for observing Io plasma torus (IPT). Figure 2.2 (Yoshikawa et al., 2014) and 2.3 show schematic and actual spectral images observed with dumbbell-shaped slit. When observing the IPT, the center part of the slit is placed on the northern polar region of Jupiter (called "on-Jupiter mode" hereinafter) with the slit aligned perpendicular to the rotational axis of Jupiter. The slit length spans 8-9 R_J (R_J, Jupiter's equatorial radius is about 7.1×10^4 km) from the center of Jupiter on both the dawn and disk sides. The wavelength coverage is from 52.0 to 148.0 nm with a resolution of 0.3 - 0.9 nm in wavelength and 17 arcsec in spatial direction (this corresponds to ~0.8 R_J at Jupiter's opposition).

Spectroscopic imaging data used in this study were reduced in the pipeline system (Kimura et al., 2019). Figure 2.3 shows the spectral image of Io tours observed by EXCEED when Hisaki was in Earth shadow. Main target of this study is faint OI 130.4 nm emission. OII 83.4 nm was also used for comparison of time variation of OI. Hisaki/EXCEED also observes IPT by using a narrower slit width 10 arcsec width several times. In this mode, we can observe

the emission only from the equational part of IPT (0.5 R_J) with better spectral resolution (0.2 - 0.3 nm), which is better for plasma diagnosis. However, we did not use this mode for analyzing the faint OI emission because the observation was not continuous and the field of view (FOV) was limited in vertical direction.

Figure 2.1. Image of the Hisaki spacecraft
(JAXA homepage; http://jaxaglobal.jp/projects/sat/sprint_a/)

Table 2.1. Major Characteristics of Hisaki satellite
(JAXA homepage; http://www.jaxa.jp/projects/sas/sprint_a/index_j.html)

Launch	Time and Date	14:00 on 14 September 2013
	Location	Uchinoura Space Center (USC)
	Launch Vehicle	Epsilon
Configuration	Weight	348 kg
Orbit	Altitude	Apogee 950 km, Perigee 1150 km
	Inclination	31°
	Type of orbit	Elliptical
	Period	About 106 minutes

Table 2.2. The specification of EXCEED (Yoshikawa et al., 2014)

Wavelength coverage	52.0 - 148.0 nm
Wavelength resolution (FWHM)	0.3 - 0.9 nm
Spatial resolution (FWHM)	17"
Field of view (FOV)	360" × 60" (mode 3; dumbbell shape slit)
Filter	Blank (this study)
	Indium (transmittance 70 - 110 nm)
	CaF_2 (transmittance around 130 nm)

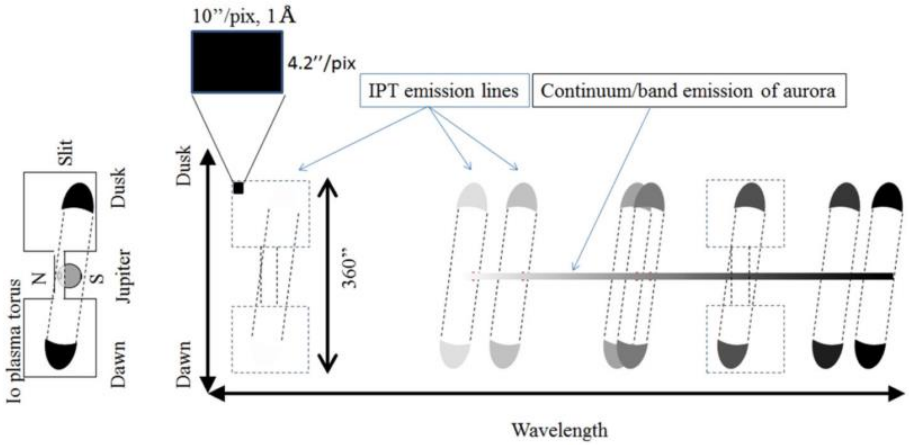

Figure 2.2. Schematic drawing of spectral image of dumbbell shape slit (Yoshikawa et al., 2014).

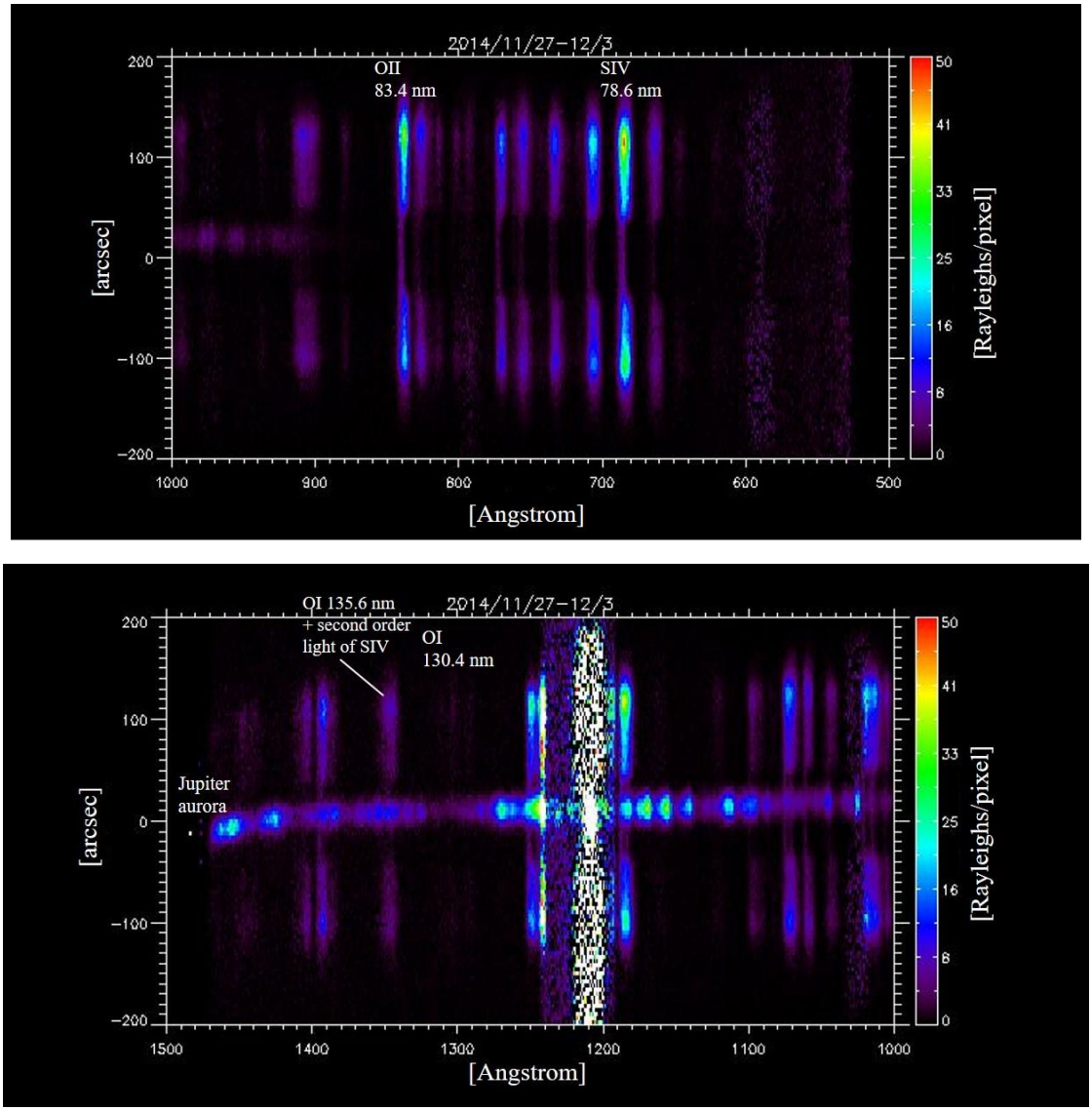

Figure 2.3. Example of spectral images of Io torus observed with a dumbbell-shape slit averaged from 27 November 2014 to 3 December 2014. The local time of Hisaki is limited in night side (local time range of 20-4 h). Geo-coronal emissions of oxygen atom, which distribute around the Earth (see section 4.2), were subtracted. Horizontal axis shows wavelength, while vertical axis shows spatial direction. Color contour shows brightness in Rayleighs per pixel.

2.1.2 Geo-corona

There are foreground emissions which are excited by solar resonance scattering of terrestrial ionosphere and geo-corona, when we look at the Io torus from the height of Hisaki orbit (950-1150 km). Foreground emissions of H and He are also originated from the interplanetary medium. Figure 2.4 shows a spectral image of foreground emission (Yoshikawa et al., 2014). Emissions of Lyman-α (121.6 nm), OII (83.4 nm), OI (130.4 nm) are clearly identified in the data. These emissions contaminate atomic oxygen or hydrogen emission from Io torus. Emission of He (58.4 nm) and its second order light (about 117 nm) are also identified. To subtract the geo-coronal emission, observation data at 5 arc min northward of Jupiter (called the off-Jupiter mode) was routinely obtained once every 3 revolutions of the satellite around Earth until 12 February 2014, and it was obtained once a day after that during the observation period of IPT.

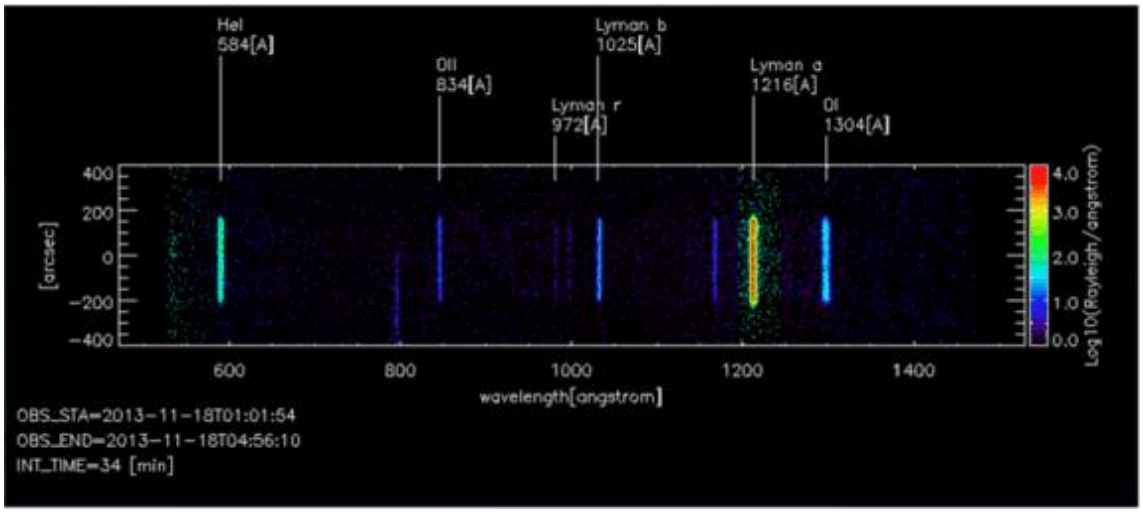

Figure 2.4. Spectral image of foreground emissions (geo-corona) obtained on 28 November 2013 (Yoshikawa et al., 2014).

2.1.3 Field of view in 2014-2015

Figure 2.5 shows distribution of HeI 58.4 nm as a function of Day of year in 2015 (Tsuchiya et al., 2018). The geo-coronal HeI is emitted by solar resonance scattering and can be assumed to be homogeneous inside the slit aperture. Therefore, the distribution along the vertical axis indicated FOV of the spectrograph. Just before February 13 in 2015, the limit of FOV on the dusk side is close to ~7 R_J from Jupiter, and that on the dawn side is over 9 R_J. The limit of ~7 R_J was switched to the dusk side after February 13 because of the altitude change of Hisaki satellite. In the whole period, the range of 5-7 R_J is in the FOV both on the dawn and dusk sides.

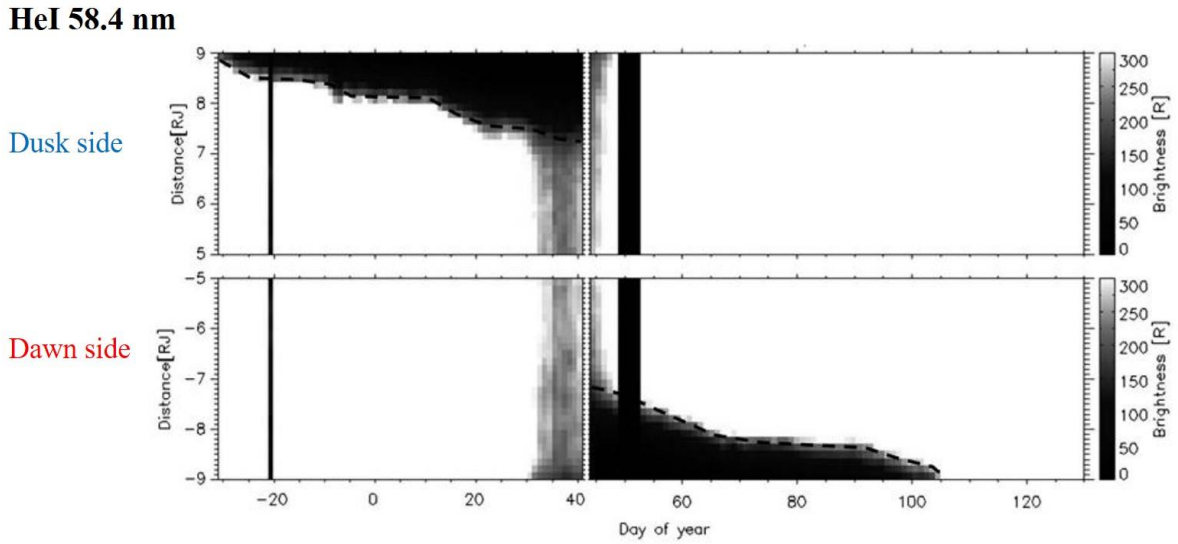

Figure 2.5. Distribution of HeI 58.4 nm as a function of Day of year in 2015 (Tsuchiya et al, 2018). The broken lines show the outer boundary of FOV.

Because the edges of FOV depend on wavelength due to the optical distortion (Tsuchiya et al., 2018). We evaluated the FOV at OI 130.4 nm in November 2014- May 2015. We integrated off-Jupiter mode data for two months to accumulate foreground emissions. Figure 2.6 shows the intensities of six foreground emissions as a function of a spatial axis along the slit. We smoothed the data with five pixels (red lines) to reduce the noise. We labeled outer edges of the dumbbell slit as P1 and P4, inner edges which correspond to the narrow parts of the slit as P2 and P3. We determined positions of four edges in such a way that the intensities of foreground emissions at P1-P4 were the same, and interval between P2 and P3 was 22.0 pixel. Relation between wavelength and the position of the edges of FOV is shown in Table 2.3 and Figure 2.7. We also analyzed daily variation of the position of P1-P4 relative to the Jupiter position using HeI 58.4 nm, and Jupiter aurora emission between 125.0-129.0 nm. The result is shown in left side of Figure 2.8. Correcting the distortion shown in Table 2.3, we show the position of P1-P4 at the wavelength of OI 130.4 nm in right side of Figure 2.8. The figure shows the FOV at OI 130.4 nm on either side during the period around the opposition was limited inside 6.8 R_J from

Jupiter. The range of 3-6.8 R_J on the both sides was always in the FOV in this period.

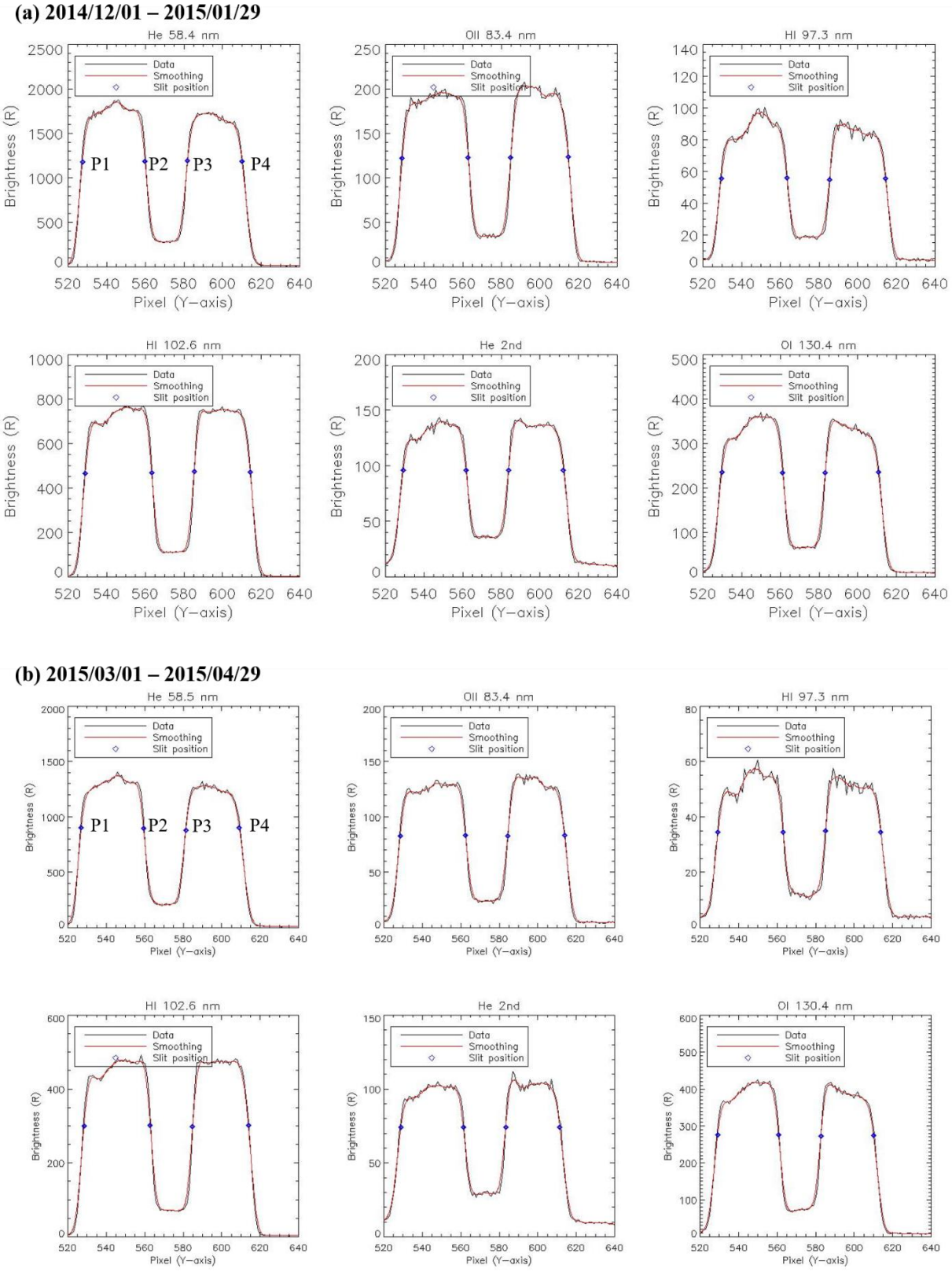

Figure 2.6. Distribution of geo-coronal HeI 58.4 nm, OII 83.4 nm, HI 97.3 nm, Ly-β 102.6 nm, OI 130.4 nm and second order light of HeI (around 117 nm) in the spectrograph. We define blue diamonds (P1-P4) as edges of FOV at each wavelength.

Table 2.3. The position of the edges (P1-P4) of FOV. The unit is pixel.

Lines	Period = 2014/12/01-2015/01/29				Period=2015/03/01-2015/04/29			
	P1	P2	P3	P4	P1	P2	P3	P4
He 58.4 nm	527.4	559.9	581.9	610.1	528	563.6	585.6	611.8
OII 83.4 nm	528.7	562.9	584.9	614.6	529	565.8	587.8	615.1
HI 97.3 nm	529.4	563.4	585.4	614.3	529.1	566.4	588.4	614.7
Ly-β 102.6 nm	528.9	563.3	585.3	614.3	529.5	566.8	588.8	615.2
He2nd 117 nm	529.2	561.7	583.7	612.2	529.5	565.1	587.1	613
OI 130.4 nm	529.7	561.2	583.2	610.6	530.2	564.6	586.6	612.5

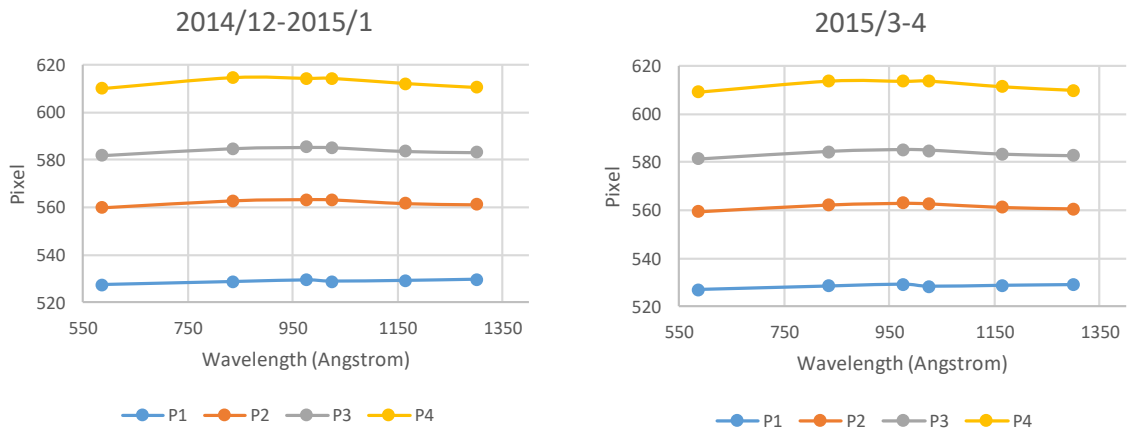

Figure 2.7. Plots of the position of the edges (P1-P4) of FOV vs. wavelength. Each point corresponds to Table 2.3.

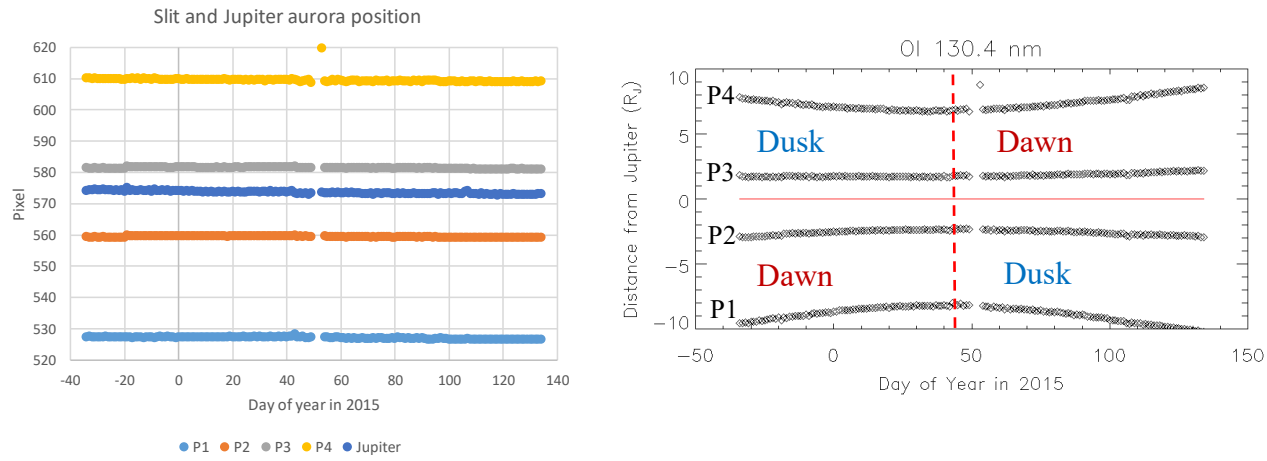

Figure 2.8. (Left) Plot of the position of the edges (P1-P4) of FOV and the peak position of Jupiter aurora vs. Day of year in 2015 at the wavelength of HeI 58.4 nm. (Right) The position of the edges at OI 130.4 nm as a function of the distance from Jupiter. Dashed vertical red line shows the date of y-axis altitude change of Hisaki.

2.2 Sodium nebula observation

To support international campaign of Hisaki mission, observation of Jupiter's sodium nebula has been made at the Haleakala High Altitude Observatory, which is on the summit of Mt. Haleakala, Maui, Hawaii. The optical instruments used for this observation are a small refractor (10 cm aperture), a CCD (Charge Coupled Device) camera, an interference filter for the sodium D-lines (center wavelength of 589.5 nm with full width at half maximum (FWHM) of 1.7 nm), a linear shape occulting mask made of neutral density filter (ND4) to mask the bright image of Jupiter, and a Na-off band filter (center wavelength of 620 nm with an FWHM of 10 nm) to discriminate scattered light. The detailed specifications of the sodium imager are shown in Table 2.3, and the pictures of these instruments are shown in Figure 2.8.

We used the inner region of sodium nebula (5-150 R_J), because outer region of sodium nebula (150 R_J-) is not expected to clearly show the variation. Na-on image includes Na D-line emissions from the sodium nebula, continuum light which is scattered from bright disk of Jupiter, and terrestrial sodium airglow. Na-off image only includes the continuum light. After subtracting dark images, flat-fielding reduction was made for both Na-on and Na-off images. D-line image is made to subtract Na-on image from Na-off image. Yoneda et al. (2007) and Yoneda et al. (2009) give more explanation for details.

Figure 2.10 shows the images of Jupiter's sodium nebula observed by the optical instrument explained above (Yoneda et al., 2015). In 22 December 2014, we can find the sodium nebula spread out near 100 R_J from the image. The enhancement and expansion of sodium nebula was clear seem in 20 February 2015. We compared time variations of OI 130.4 nm around Io and sodium nebula emission in 2013-2014 and 2014-2015 in section 3.2.

Table 2.3. Specifications of the sodium imager (Yoneda et al., 2007).

Objective lens	Nikkor 200 mm (F/2.0) ϕ100 mm
Collimating and imaging lenses	Nikkor 50 mm (F/1.2)
Detector	Andor DV434-BV CCD camera
Spatial resolution	11.45"/pixel (0.5 R_J/pixel)
Field of view	2.5° (400 R_J)
Interference filters	
Center/FWHM wavelength	
Na on-band	589.5/1.7 nm
Na off-band	620/10 nm
Exposure time	
Na on-band	900 sec
Na off-band	200 sec

Figure 2.9. Pictures of the observation system for sodium nebula. (Left) Picture of wide-FOV monochromatic imager used in the sodium nebula observation (red arrow). (Right) The imager is attached onto the T40 telescope in Tohoku university Haleakara observatory.

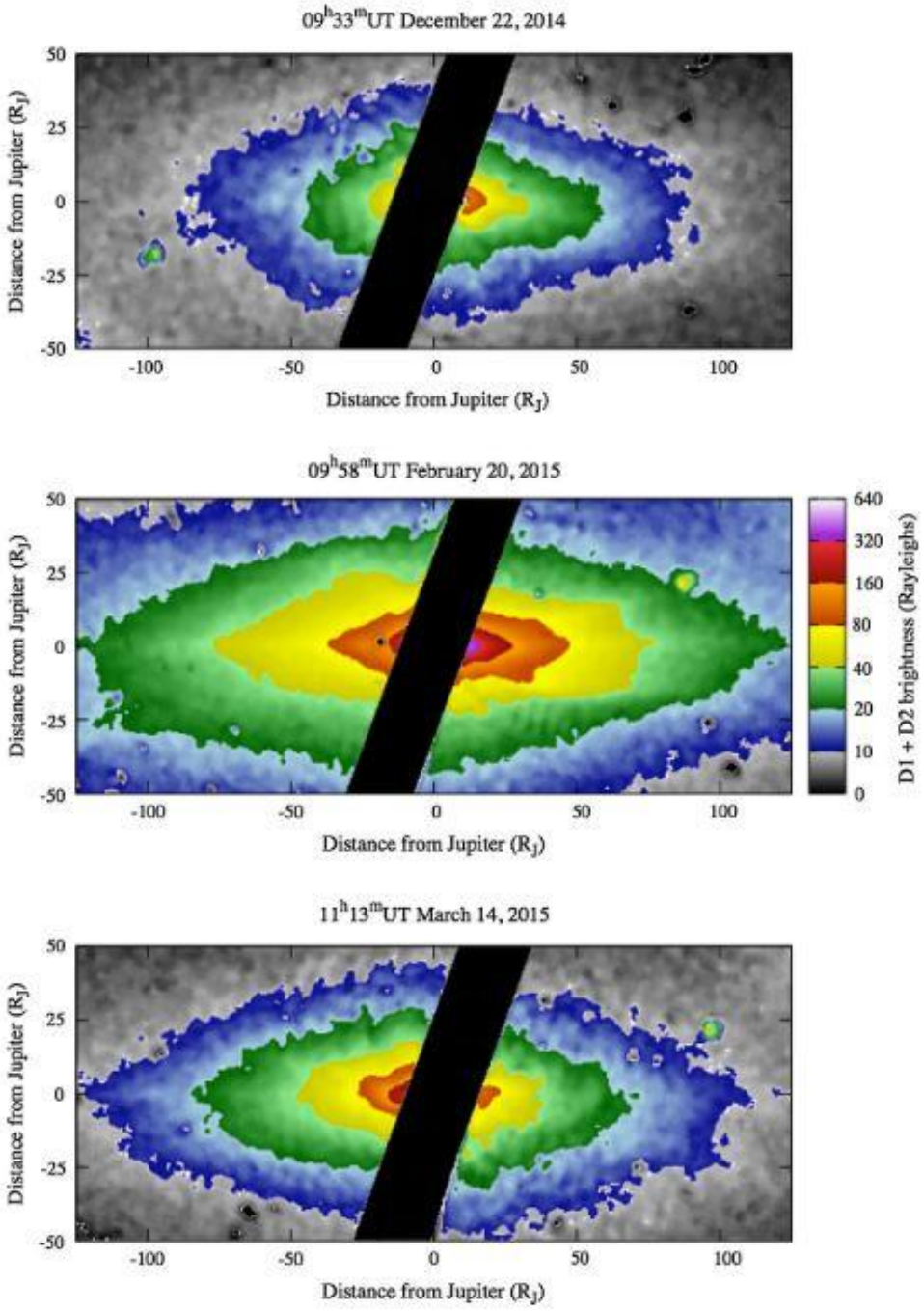

Figure 2.10. There images of Jupiter's sodium nebula observed by Tohoku university's optical instrument in 2014-2015 (Yoneda et al., 2015).

2.3 ALMA

The Atacama Millimeter/Submillimeter Array (ALMA) is an aperture synthesis radio telescope consisting 66 antennas (Figure 2.11). 12-m Array consists of fifty of these antennas whose diameter is 12 m, which is used for high sensitivity and angular resolution imaging. The Atacama Compact Array (ACA) are composed of twelve 7-m antennas (7-m Array) and four 12-m antennas. They are used for wide-field imaging of extended structure. Specification of ALMA is shown in Table 2.4. ALMA has observed planets, moons and small cold distant bodies in our solar system and imaged their surfaces and atmospheres with high angular and wavelength resolution.

ALMA is located on the Chajnantor plain of the Chilean Andes (latitude = -23.02917°, longitude = -67.754649°). The place is normally dry and in clear sky condition, suitable for millimeter and submillimeter observation. Atmospheric windows in the range of ALMA frequency coverage are shown in Figure 2.12. The broad and deep absorption features are mostly due to H_2O in lower atmosphere, and some features are due to O_2 in the atmosphere. ALMA archive data of Io used in this study is in Band 7 (275-373 GHz). Detail technical and science explanation about ALMA is shown in Schieven (2019) and Remijan et al (2019).

Figure 2.11. Picture of ALMA 12-m Array and ACA (Remijan et al., 2019). The ALMA 12-m array are distributed in left side of the image. ACA with all 7-m array antennas and four single-dish 12-m antennas are shown in dashed orange circles and blue circles, respectively.

Table 2.4. Specification of ALMA (Schieven 2019). ν is frequency (GHz)

Number of antennas	50×12 m (12-m Array)
	12×7 m & 4×12 m (ACA)
Maximum baselines lengths	0.16-16.2 km
Angular resolution (arcsec)	~0.2”×(300/ν GHz)×(1 km/maximum baseline)
12m primary beam (arcsec)	~20.6”×(300/ν GHz)
7m primary beam (arcsec)	~35”×(300/ν GHz)
Number of baselines	Up to 1225
Frequency coverage	All atmospheric windows from 84-950 GHz
Polarimetry	Full stokes parameter

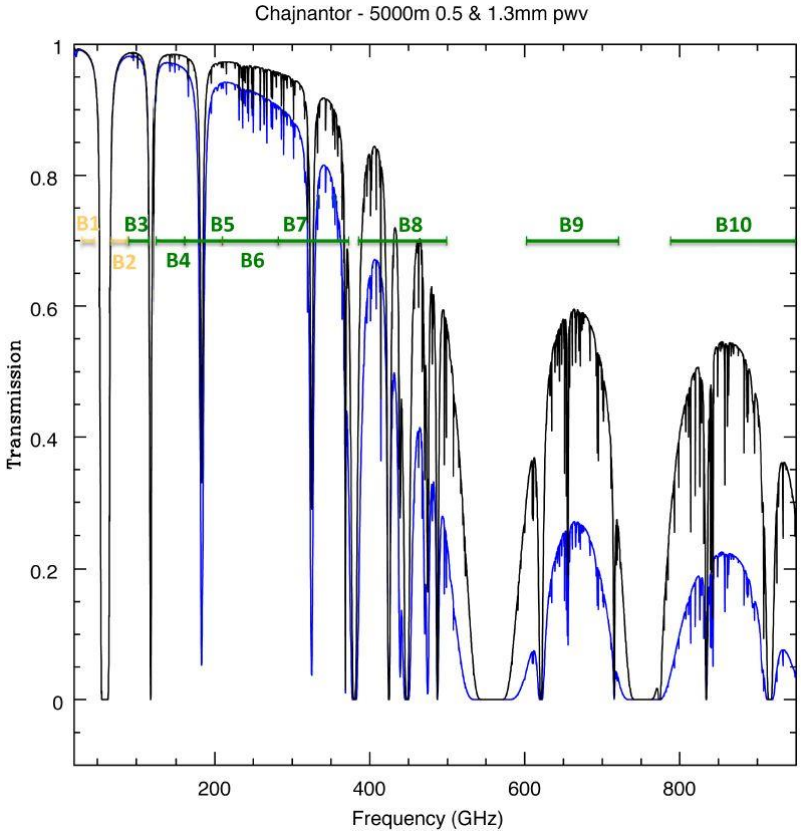

Figure 2.12. The ten ALMA receiver bands (B1-B10) with atmospheric transmission (Schieven 2019). Blue and black curves atmospheric transmission in case that precipitable water vapors are 1.3 mm and 0.5 mm, respectively.

Chapter 3 ALMA observation of Io's SO_2 atmosphere

3.1 Observation and data analysis

We analyzed the public open data obtained from ALMA Science Archive (Stoehr et al., 2019). The project code is 2017.1.00670.S. The observation was carried out 6 times on 20 March 2018, and the duration of each observation was about 7 minutes. We selected the data observed from 10:02 to 10:09 UT (before ingress), and that from 10:54 to 11:01 UT (after ingress). We used the HORIZONS database (Giorgini et al., 1996) to calculate the ephemeris of Io. Table 3.1 shows the position of Io during the observations. Angle of Sun-Jupiter-Io of the first data was ~170 degree, corresponding to several minutes before ingress of Jupiter shadow (the angle when Io enters Jupiter shadow is ~171 degree of Sun-Jupiter-Io angle). The angle of the fourth data was ~176 degree, ~40 minutes after ingress. Io is tidally locked by Jupiter's large gravity force, and the rotational period is the same as the revolution period. Therefore, ALMA observed the hemisphere of Io facing to Jupiter in this event. The channel spacing and spectral resolution were 122 kHz and 244 kHz, which correspond to 0.11km/s and 0.21 km/s at 332 GHz respectively.

Table 3.1. Coordinates of Io during the ALMA observations in 20 March 2018. The bold character shows the data analyzed in this study. We set Antofagasta in Chile (23°39'S, 70°24'W) as the observer to calculate right ascension and declination of Io.

Period	Right ascension (hour:min:sec)	Declination	Sun-Jupiter-Io angle (deg.)	Earth-Io-Jupiter angle (deg.)
10:02:28-10:09:04	**15:22:43.53**	**-17°16'12.8"**	**169.88**	**8.4739**
10:11:04-10:17:39	15:22:43.63	-17°16'13.1"	170.96	8.4734
10:19:39-10:21:40	15:22:43.72	-17°16'13.5"	171.75	8.4729
10:54:43-11:01:18	**15:22:44.20**	**-17°16'15.4"**	**175.81**	**8.4702**
11:03:18-11:09:53	15:22:44.30	-17°16'15.8"	176.71	8.4697
11:11:51-11:13:53	15:22:44.38	-17°16'16.1"	176.89	8.4692

We made subtraction of continuum and synthesis imaging with calibrated data by using the Common Astronomy Software Applications (CASA) version 5.1.1 package. The calibrated data was generated by running the program "ScriptForPI.py" in ALMA Quality Assurance (QA2) data, according to the explanation described in Petry et al. (2018). We separated the data into the line channel which include spectral lines of SO_2, SO, and the continuum channels in each spectral windows, for subtraction of continuum emission component. The molecular lines detected in the observation are summarized in Table. 3.2. The values of Einstein A coefficients and the upper state energies are referred from Splatalogue database. We conducted the *tclean* task in CASA and used Hogbom algorithm (Hogbom, 1974) with briggs weighting for deconvolution (cleaning). We set the image pixel sizes as 0.06" × 0.06". The resulting spatial resolutions (synthesis beam sizes) are 0.36" × 0.28" before the ingress, and 0.41" × 0.28" after the ingress. The typical rms (root square mean) noise level is 0.01- 0.02 Jy/beam.

Table 3.2. Summary of the information of the molecular lines of SO_2 and SO. E_{up} shows the upper state energy.

Species	Transition	Frequency (GHz)	A coefficient (A_{ul}, s^{-1})	E_{up}/k (K)
SO_2 (i)	$J(Ka, Kc)$ = 4(3,1)-3(2,2)	332.50524	3.29×10^{-3}	31.29
SO_2 (ii)	$J(Ka, Kc)$ = 16(4,12)-16(3,13)	346.52388	3.39×10^{-3}	164.46
SO_2 (iii)	$J(Ka, Kc)$ = 19(1,19)-18(0,18)	346.65217	5.22×10^{-3}	168.14
SO_2 (iv)	$J(Ka, Kc)$ = 21(2,20)-21(1,21)	332.09143	1.51×10^{-3}	219.53
SO	$J(N)$ = 8(8)-8(7)	344.31079	1.38×10^{-2}	49.32
SO	$J(N)$ = 9(8)-8(7)	346.52848	1.60×10^{-2}	43.19

3.2 Results

3.2.1 Synthesized integrated intensity maps

To investigate the spatial distribution of Io's atmosphere, we integrated the intensity of SO_2 346.652 GHz (J(*K*a, *K*c)=19(1,19)-18(0,18)) and SO 346.528 GHz ($J(N)$=9(8)-8(7)) emissions in the range of ~±1 km/s from the emission peak and draw maps (Figure 3.1a). The SO_2 emission at 346.652 GHz is most intense among the observed lines. Before integrating the intensity, we converted the unit from flux density S (Jy/beam) to brightness temperature T_{MB} (K) using the Rayleigh-Jeans relation as follows (ex. Wilson et al., Tools of Radio Astronomy Fifth Edition, 2009):

$$T_{MB} = \frac{\lambda^2 S}{2k\Omega} = 13.6\frac{\lambda^2 S}{b_{maj} \times b_{min}}, \tag{3.1}$$

where λ is wavelength (mm), k is the Boltzmann constant, and Ω is beam size, which is defined as:

$$\Omega_{\mathrm{beam}} = \frac{\pi b_{maj} \times b_{min}}{4In2}, \tag{3.2}$$

where b_{maj} and b_{min} are major and minor axes of the beam size, respectively. Disk averaged flux density, brightness temperature and parameters used to calculate the brightness temperature are summarized in Table 3.2.

Table 3.2. Disk average peak flux density (S) and brightness temperature (T_{MB}) of each lines used in this study.

Molecular lines	S (Jy/beam)	b_{maj} (")	b_{min} (")	λ (mm)	S => T_{MB}	T_{MB} (K)
Before ingress						
SO_2 332.505 GHz	0.083	0.359	0.282	0.901	109.13	9.03
SO_2 346.524 GHz	0.146	0.359	0.282	0.865	100.48	14.68
SO_2 346.652 GHz	0.203	0.359	0.282	0.865	100.41	20.37
SO_2 332.091 GHz	0.085	0.359	0.282	0.902	109.40	9.27
SO 346.528 GHz	0.044	0.359	0.282	0.865	100.48	4.44
After ingress						
SO_2 332.505 GHz	0.049	0.410	0.277	0.901	97.28	4.76
SO_2 346.524 GHz	0.091	0.410	0.277	0.865	89.57	8.12
SO_2 346.652 GHz	0.146	0.410	0.277	0.865	89.55	13.06
SO_2 332.091 GHz	0.053	0.410	0.277	0.902	97.52	5.19
SO 346.528 GHz	0.029	0.410	0.277	0.865	89.57	2.58

Before the ingress, SO_2 emission widely distributed around the equator of Io where the sublimation of the surface frost mainly occurs. This feature is consistent with the previous observation (ex. Feaga et al., (2009)). Near the equator, the emission on the western side was brighter than that on the east side. These features cannot be explained by sublimation from uniform surface frost, but reflect ununiformed frost distribution or are presumed to be generated by volcanism. We also find the brightest feature on the east side in the high latitude region of the north hemisphere. SO is not stable in solid phase, and its possible sources are direct volcanic input and photodissociation of gaseous SO_2 (Moullet et al., 2008). The distribution of SO emission is similar to that of SO_2. However, the maximum emission peak of SO was on the western side near the equator, different from that of SO_2. After ingress, the both disk average intensities of SO_2 and SO emissions decreased significantly. It is interpreted to be due to condensation of the sublimation atmosphere. However, both emissions survived in the presumed volcanically active areas as mentioned above.

Figure 3.1b shows the distribution of hot spots observed by Cantrall et al. (2018) on Io's disk before and after ingress. There are many hot spots in the high intensity areas of SO_2 and SO emissions (on the west side near equator and on the east side near limb). On the other hands, there are few hot spots around the center of Io's disk. Before ingress, the position of consistently active hot spot Jasus Patera (37.5°W, 4.4°S) coincides with the position of peak emissions of SO_2 and SO on the west side. The positions of another active volcanoes Loki (308.5°W, 13.4°N) and Pele Patera (254.7°W, 18.4°S) do not coincide the position of the

emission peak on the east side.

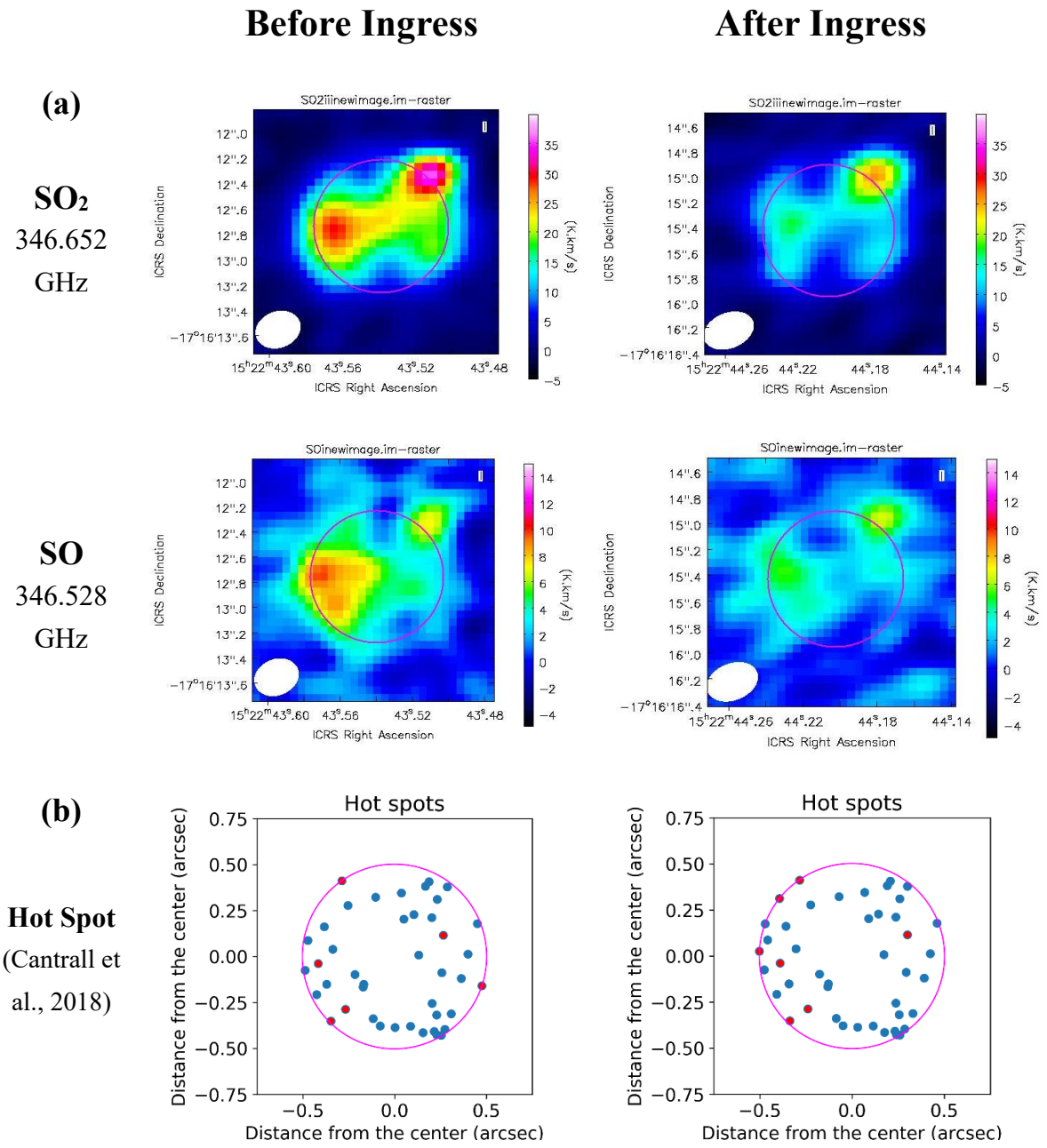

Figure 3.1. (a) Integrated intensity maps of SO_2 346.652 GHz (19(1,19)-18(0,18)) and SO 346.528 GHz (9(8)-8(7)) emissions before and after Ingress. Unit is K·km/s. Red circles show Io's disk and white ovals show the beam size. (b) Distribution of hot spots on Io's disk in the same periods. Longitude and latitude of hot spots are referred from Cantrall et al. (2018). Red marks show consistent hot spots whose detection rates are high (see Chapter 1.2.1).

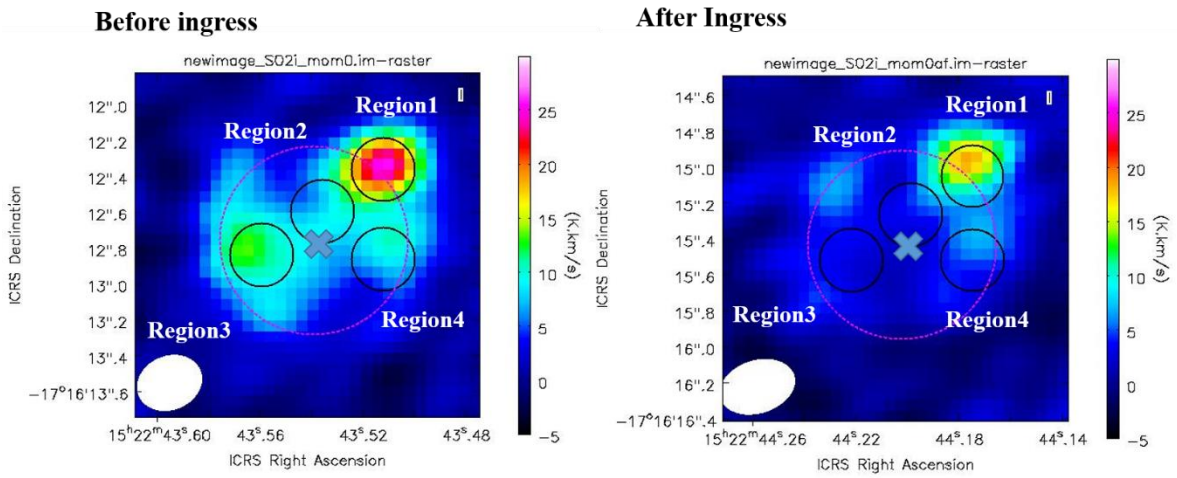

Figure 3.2. The position of each region which we set in this study. The transition is SO_2 332.505 GHz (4(3,1)-3(2,2)). Dashed lines show the position of Io's disk. Cross marks show the centers of Io's disk.

We define the four regions as indicated in Figure 3.2 and Table 3.3 to derive velocity distribution (section 3.2), column density and rotational temperature (section 3.3) of molecular gases in each region. We labeled presumed volcanically active areas in the east side northern high latitude and the west side of the equator as Region 1 and 3, respectively. For comparison with these regions, we labeled the area near Io's center where sublimation is expected to be dominant as Region 2, and labeled the area south from Region 1 as Region 4.

Table 3.3. Coordinate and range of each region. The diameter of the average area of Io's disk corresponds to the sum of Io's diameter and the beam size.

	Before Ingress		After Ingress		Range
Region	Right ascension (hour:min:sec)	Declination	Right ascension (hour:min:sec)	Declination	Diameter (")
Full disk	15:22:43.539	-17°16'12.754"	15:22:44.202	-17°16'15.429"	1.4
1	15:22:43.512	-17°16'12.365"	15:22:44.175	-17°16'15.030"	0.35
2	15:22:43.536	-17°16'12.591"	15:22:44.199	-17°16'15.266"	0.35
3	15:22:43.559	-17°16'12.837"	15:22:44.222	-17°16'15.512"	0.35
4	15:22:43.512	-17°16'12.838"	15:22:44.175	-17°16'15.513"	0.35

3.2.2 Velocity distribution in each region

Figure 3.3 shows the velocity distribution of SO_2 346.652 GHz (19(1,19)-18(0,18)) emissions in the four regions. We fitted the observed line profile by using Gaussian function ($f_1(x)$) as follows:

$$f_1(x) = T_B \cdot exp\left(-\frac{(x-x_0)^2}{2B^2}\right), \tag{3.3}$$

where x is velocity (km/s), T_B, x_0 and B are fitting parameters. Shapes of velocity distribution in Region 2-4 are symmetry and fitted well. However, the shape of velocity distribution in Region 1 is asymmetry and cannot be fitted well compared with Region 2-4. We also found the asymmetry feature of Region 1 at the other lines.

We evaluated line width (W) and integrated intensity (I_{int}),

$$W = 2\sqrt{2ln2}B, \tag{3.4}$$

$$I_{int} = \sqrt{2\pi}AB. \tag{3.5}$$

Variance−Covariance matrix of parameters ($pcov$) is

$$pcov = \begin{pmatrix} \sigma_A^2 & \sigma_{Ax_0} & \sigma_{AB} \\ \sigma_{Ax_0} & \sigma_{x_0}^2 & \sigma_{Bx_0} \\ \sigma_{AB} & \sigma_{Bx_0} & \sigma_B^2 \end{pmatrix}. \tag{3.6}$$

In this case, fitting parameters are correlated each other. Errors of integrated intensity (E_{int}) are

$$E_{int}^2 = \left(\frac{\partial I_{int}}{\partial A}\right)^2 \sigma_B^2 + \left(\frac{\partial I_{int}}{\partial B}\right)^2 \sigma_A^2 + 2\left(\frac{\partial I_{int}}{\partial A}\right)\left(\frac{\partial I_{int}}{\partial B}\right)\sigma_{AB}, \tag{3.7}$$

$$E_{int} = \sqrt{2\pi} \cdot \sqrt{B^2\sigma_A^2 + A^2\sigma_B^2 + 2BA\sigma_{AB}}. \tag{3.8}$$

Line widths, integrated intensities and their errors are summarized in Table 3.4. Before and after ingress, the line widths of Region 1 are broader than those of the other regions at all emission lines. FWHM of the velocity distribution due to the Doppler broadening (W_D) is given by

$$W_D = \sqrt{\frac{8RTIn2}{Mc^2}}v_0 \approx 7.16 \times 10^{-7}\sqrt{\frac{T}{M}}\ (Hz), \tag{3.9}$$

where R is gas constant, T is temperature, M is molecular weight, c is light speed. Assuming that the line width was only determined by the Doppler broadening, disk average gas temperature of Io's atmosphere is evaluated to 656 K. It is much higher than previous

observation result (160-210 K) (Moullet et al., 2008). Therefore, both gas temperature and atmospheric dynamics (the Doppler shift due to bulk gas motion) contribute to determine the line width.

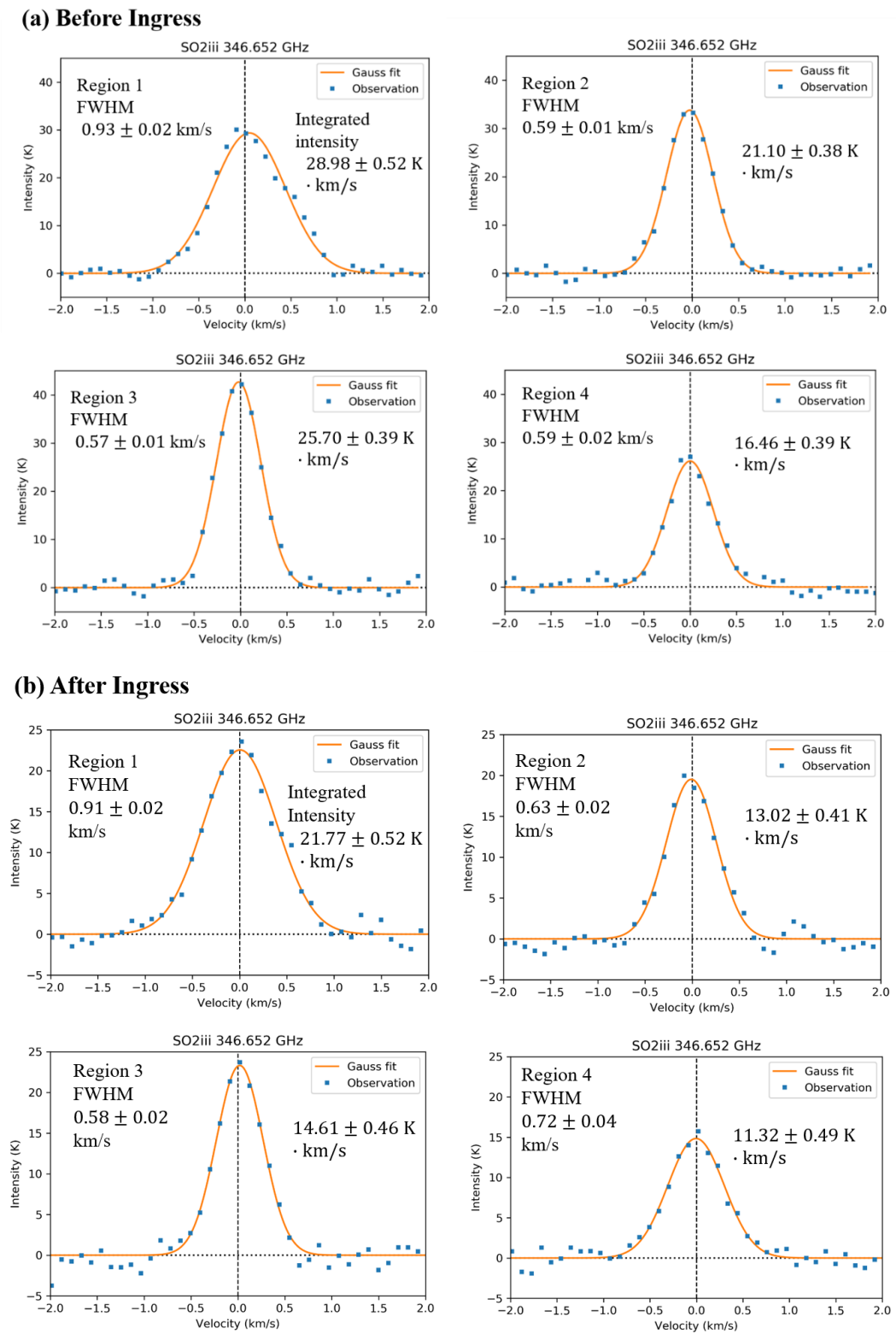

Figure 3.3. Velocity distribution of SO_2 346.652 GHz (19(1,19)-18(0,18)) emissions in four regions ((a) before ingress, (b) after ingress). x-axis shows the offset from the velocity where Io's disk average velocity distribution is peak (positive shows line of sight direction far from Earth). Solid lines show Gauss fitting to the observed distribution.

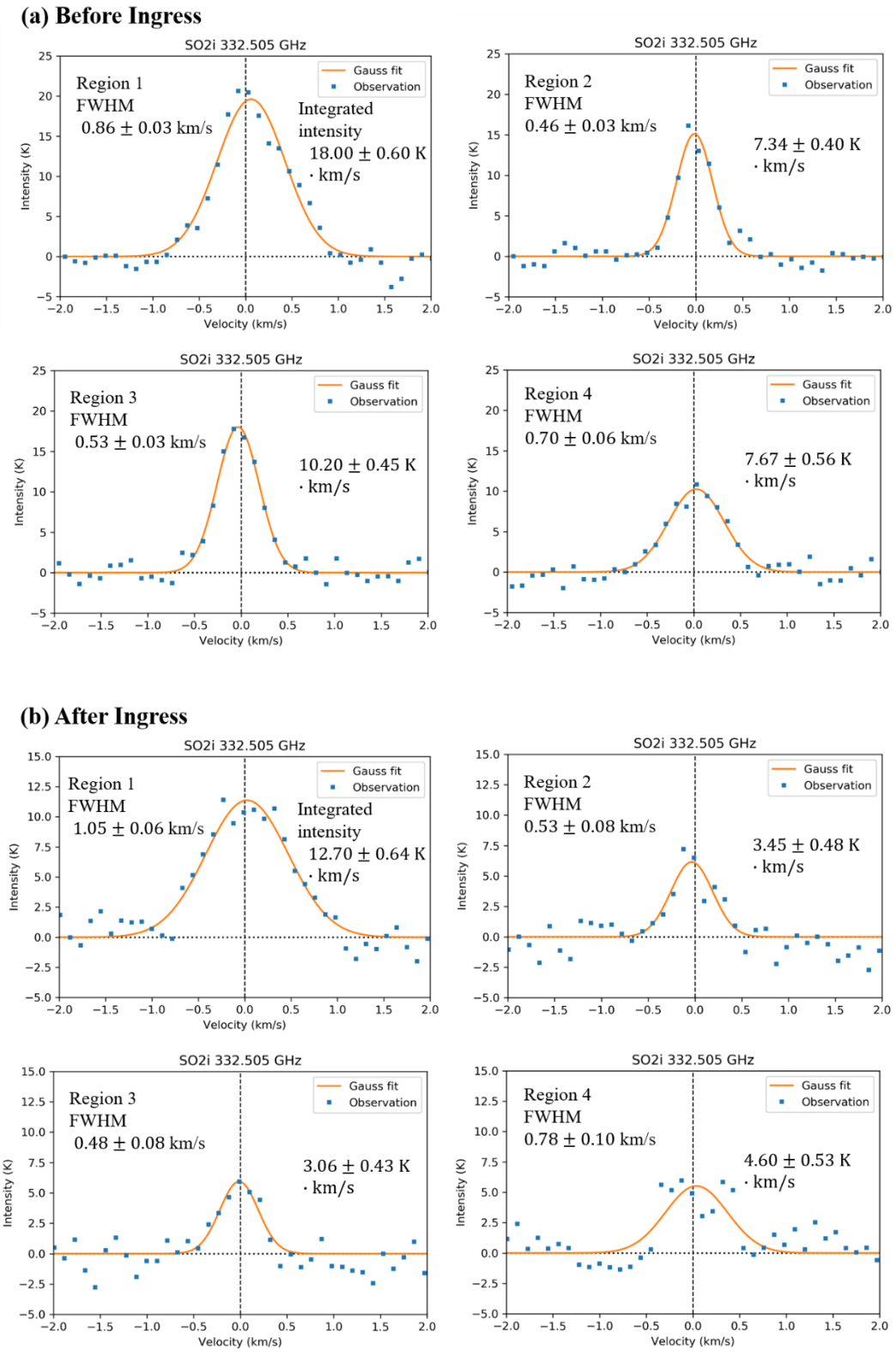

Figure 3.4. Same as Figure 3.3, but the transition is SO_2 346.505 GHz (4(3,1)-3(2,2)).

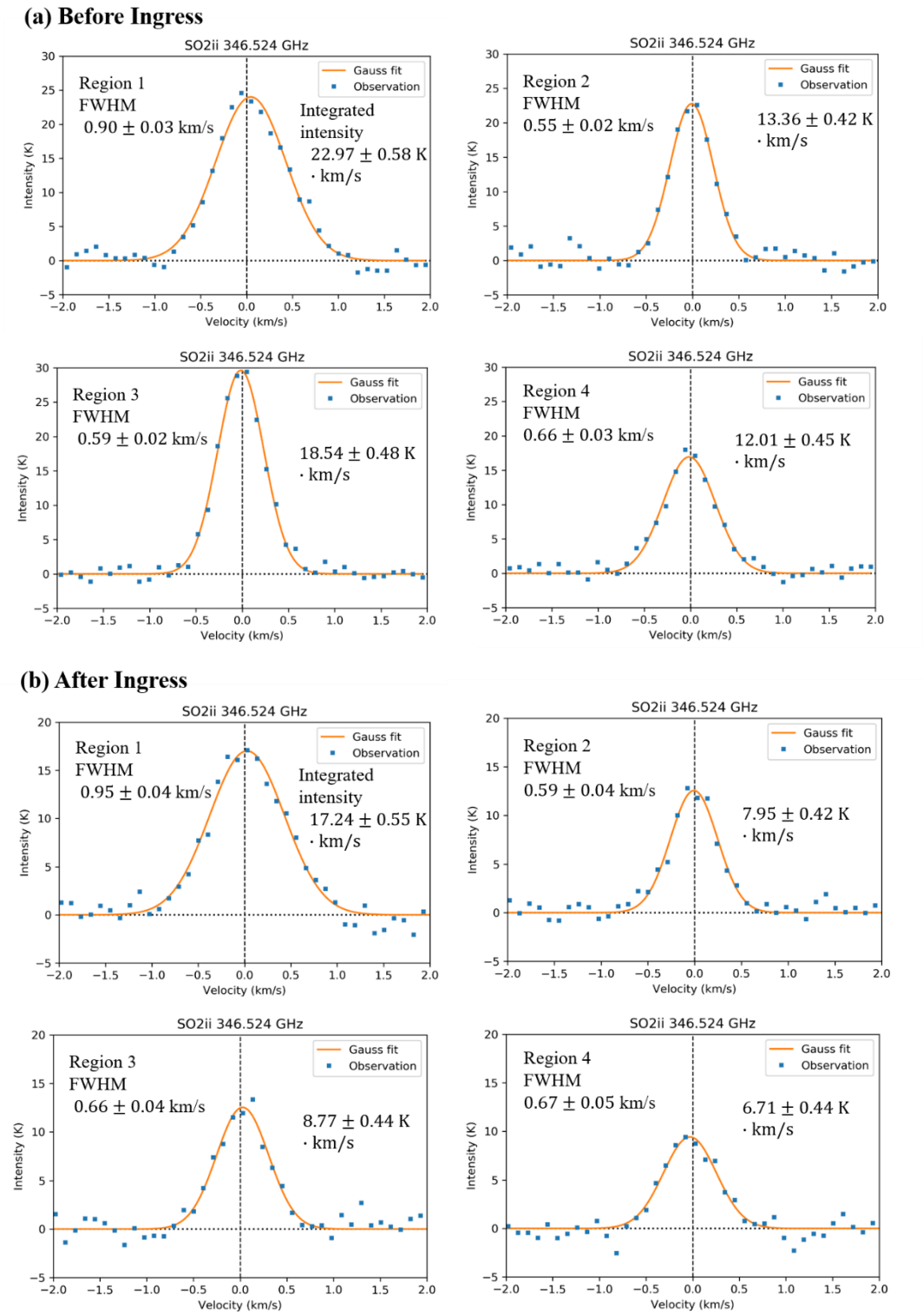

Figure 3.5. Same as Figure 3.3, but the transition is SO_2 346.524 GHz (16(4,12)-16(3,13)).

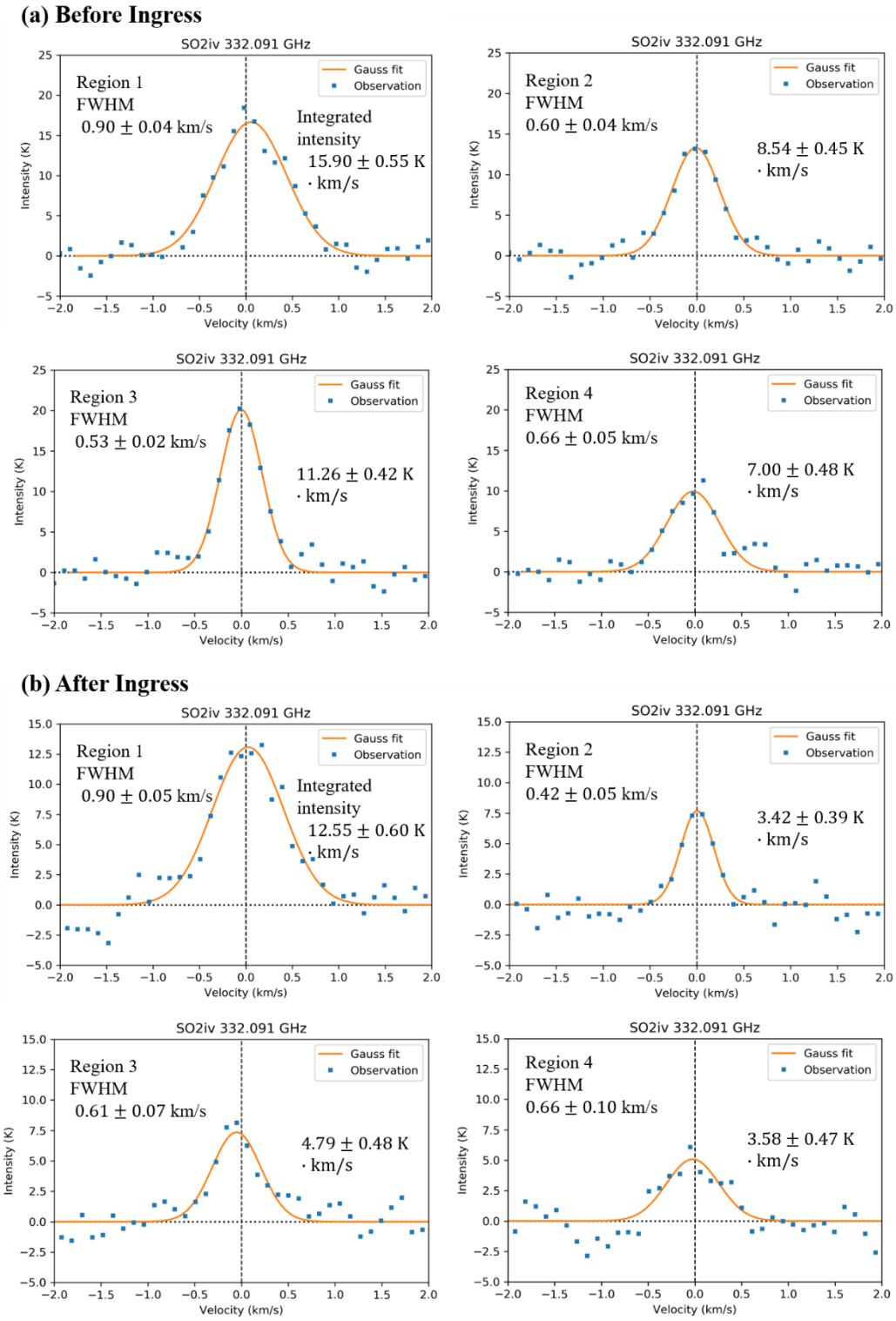

Figure 3.6. Same as Figure 3.3, but the transition is SO_2 332.091 GHz (21(2,20)-21(1,21)).

Table 3.4. Peak intensity (T_B), line width (W) and integrated intensity (I_{int}) in each region and transition. The values in parentheses denote one standard deviation in last digits. For example, 0.86(3) and 0.78(10) mean 0.86±0.03 and 0.78±0.10.

	Transition for SO_2											
	(i) 332.505 GHz			(ii) 346.524 GHz			(iii) 346.652 GHz			(iv) 332.091 GHz		
Before Ingress	T_B (K)	W (km/s)	I_{int} (K·km/s)	T_B (K)	W (km/s)	I_{int} (K·km/s)	T_B (K)	W (km/s)	I_{int} (K·km/s)	T_B (K)	W (km/s)	I_{int} (K·km/s)
Region 1	19.60(65)	0.86(3)	18.00(60)	24.01(60)	0.90(3)	22.97(58)	29.35(53)	0.93(2)	28.98(52)	16.66(58)	0.90(4)	15.90(55)
Region 2	15.12(83)	0.46(3)	7.34(40)	22.76(71)	0.55(2)	13.36(42)	33.78(61)	0.59(1)	21.10(38)	13.30(70)	0.60(4)	8.54(45)
Region 3	18.01(80)	0.53(3)	10.20(45)	29.63(77)	0.59(2)	18.54(48)	42.67(65)	0.57(1)	25.70(39)	20.10(76)	0.53(2)	11.26(42)
Region 4	10.25(75)	0.70(6)	7.67(56)	16.94(63)	0.66(3)	12.01(45)	26.12(62)	0.59(2)	16.45(39)	9.93(69)	0.66(5)	7.00(48)
After Ingress	T_B (K)	W (km/s)	I_{int} (K·km/s)	T_B (K)	W (km/s)	I_{int} (K·km/s)	T_B (K)	W (km/s)	I_{int} (K·km/s)	T_B (K)	W (km/s)	I_{int} (K·km/s)
Region 1	11.37(58)	1.05(6)	12.70(64)	17.03(54)	0.95(4)	17.24(55)	22.55(90)	0.91(2)	21.77(52)	13.08(63)	0.90(5)	12.55(60)
Region 2	6.15(85)	0.53(8)	3.45(48)	12.56(67)	0.59(4)	7.95(42)	19.52(62)	0.63(2)	13.02(41)	7.68(87)	0.42(5)	3.42(39)
Region 3	5.93(84)	0.48(8)	3.06(43)	12.54(64)	0.66(4)	8.77(44)	23.32(73)	0.58(2)	14.61(46)	7.35(74)	0.61(7)	4.79(48)
Region 4	5.52(63)	0.78(10)	4.60(53)	9.43(61)	0.67(5)	6.71(44)	14.84(64)	0.72(4)	11.32(49)	5.08(67)	0.66(10)	3.58(47)

3.2.3 Composite Gaussian model in Region 1

Here, we considered the asymmetry line shape in Region 1. The broader line profile in Region 1 show there are at least two velocity components in SO_2 gas. Figure 3.7 and 3.8 show the observed velocity distribution of Region 1 before and after ingress with fitting lines of the composite Gaussian function. The function is represented as

$$f_2(x) = f_{low}(x) + f_{high}(x) = T_{B\ low} \cdot exp\left(-\frac{(x-x_0)^2}{2B_{low}^2}\right) + T_{B\ high} \cdot exp\left(-\frac{(x-x_1)^2}{2B_{high}^2}\right) \quad (3.10)$$

where f_{low}, f_{high} are Gaussian functions of low and high velocity components, $T_{B\ low}$, B_{low}, x_0, x_1, $T_{B\ high}$ and B_{high} are fitting parameters ($x_0 < x_1$). We estimated Doppler shift of the high velocity component from $l = x_1 - x_0$. Before ingress, two velocity components are clearly identified at SO_2 346.652 GHz, and the composite Gaussian function (f_2) is well fitted to the velocity distribution better than the single Gaussian function (f_1). Doppler shift of high velocity component is 0.60±0.03 km/s (red shift). We also succeeded to detect low and high velocity components at the other frequencies (Figure 3.8). Doppler shifts of high velocity component are almost the same for all lines (0.57±0.06 km/s at 332.505 GHz, 0.56±0.14 km/s at 346.524 GHz and 0.53±0.06 km/s at 332.091 GHz). Peak intensity, line width and integrated intensity at each frequency are shown in Table 3.6. Intensity ratios of high and low velocity components are 1:4-7. The result shows large volcanic plume generated complex atmospheric dynamics and some part of SO_2 gas flew at the line of sight direction.

After ingress, the high velocity component of SO_2 346.652 GHz became very weak. The intensity ratio was ~1:29. The high velocity faint emission was detected at 346.524 GHz, but not detected at 332.505 GHz, 332.091 GHz. It may be because the lifetime of SO_2 gases phase became short due to the condensation and volcanic gases did not expand in the large area.

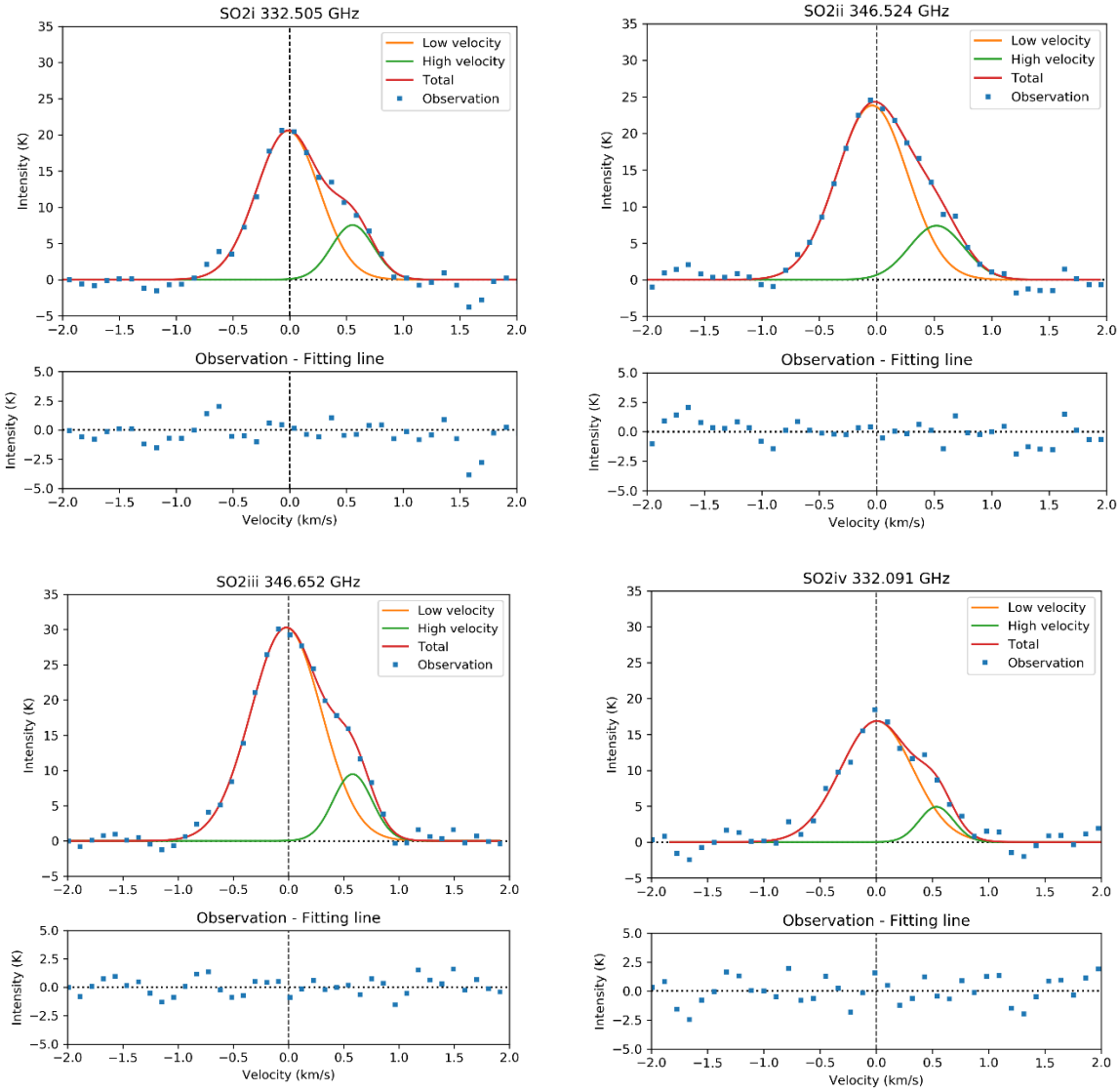

Figure 3.7. (Upper figures) Velocity distribution of SO_2 emissions in Region 1 before ingress in each transition. Solid line shows composite fitting line of Gaussian function (red line), low (orange) and high velocity components (green). (Lower figures) Plot of the fitting line subtracted from the observation.

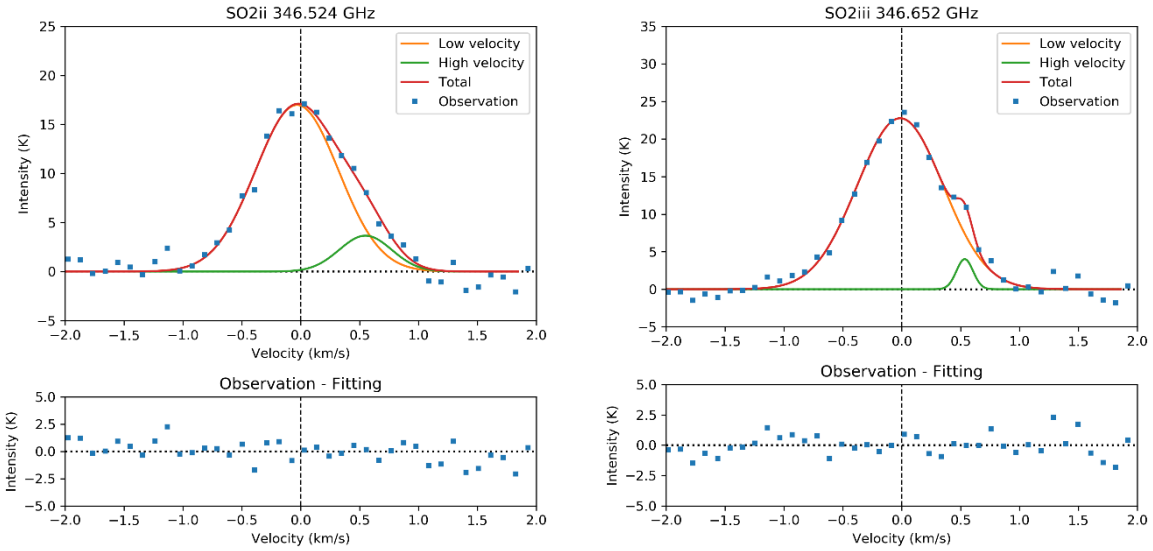

Figure 3.8. Same as Figure 3.7, but the period is after ingress and the transitions are only SO_2 3 GHz, SO_2 346.652 GHz. We cloud not detect the high velocity component of SO_2 332.505 GHz and SO_2 332.091 GHz.

Table 3.6. Line width and integrated intensity of low and high velocity components, and Doppler shift of the high velocity component relative to the low velocity component in Region 1 before the ingress (inside round bracket shows one sigma error). Unit is K·km/s. The value of the total integrated intensity in this table is slightly different to that in Table 3.5 because of using the different fitting lines (Table 3.5; the line represented as the normal Gaussian function, Table 3.6; the composite line of two Gaussian functions).

Region 1	Transition for SO_2											
	(i) 332.505 GHz			(ii) 346.524 GHz			(iii) 346.652 GHz			(iv) 332.091 GHz		
Before Ingress	T_B (K)	W (km/s)	I_{int} (K·km/s)	T_B (K)	W (km/s)	I_{int} (K·km/s)	T_B (K)	W (km/s)	I_{int} (K·km/s)	T_B (K)	W (km/s)	I_{int} (K·km/s)
High	7.54 (1.64)	0.44 (0.10)	3.50 (1.33)	7.39 (3.60)	0.56 (0.16)	4.40 (3.22)	9.48 (1.11)	0.42 (0.05)	4.20 (0.82)	4.92 (2.04)	0.36 (0.13)	1.91 (1.29)
Low	20.56 (0.82)	0.65 (0.06)	14.23 (1.40)	23.83 (1.83)	0.73 (0.08)	18.42 (3.26)	30.27 (0.47)	0.76 (0.03)	24.34 (0.89)	16.87 (0.68)	00.76 (0.08)	13.61 (1.44)
Total			17.73 (1.93)			22.81 (4.59)			28.54 (1.21)			15.51 (1.93)
After Ingress	T_B (K)	W (km/s)	I_{int} (K·km/s)	T_B (K)	W (km/s)	I_{int} (K·km/s)	T_B (K)	W (km/s)	I_{int} (K·km/s)	T_B (K)	W (km/s)	I_{int} (K·km/s)
High	No detection			3.66 (4.86)	0.52 (0.40)	4.86 (4.01)	4.01 (1.31)	0.17 (0.06)	0.71 (0.34)	No detection		
Low				16.99 (1.74)	0.83 (0.17)	15.02 (4.14)	22.77 (0.54)	0.86 (0.03)	20.85 (0.63)			
Total						17.07 (5.76)			21.55 (0.71)			

3.3 Discussion

3.3.1 Population diagram

We used population diagrams (Goldsmith and Langer, 1999) to evaluate whether the atmosphere consists of multiple temperature gases, or the atmosphere is in local thermodynamic equilibrium (LTE, the condition that all excitation temperatures are the same). If the source is optical thin, the upper level column density (N_u) is expressed as

$$N_u = \frac{8\pi k \nu^2 W}{hc^3 A_{ul}} = \gamma_u W, \tag{3.11}$$

where ν is frequency (Hz), h is Plank constant, c is light velocity (m/s), A_{ul} is Einstein A coefficient (s^{-1}, shown in Table 3.2), W is integrated intensity of the emission line (K·km/s). If a molecule in the atmosphere is in LTE, the population of each level is written as

$$N_u = \frac{N}{Z} g_u e^{-\frac{E_u}{kT}}, \tag{3.12}$$

where N is the total column density, Z is the partition function, g_u is the statistical weight, E_u is the upper state energy, T is the rotational temperature. We can rewrite the equation (3.12) as

$$In\frac{\gamma_u W}{g_u} = In\frac{N}{Z} - \frac{E_u}{kT}. \tag{3.13}$$

There is a linear relation between the logarithm of the upper state column density per statistical weight ($\mathrm{In}(\gamma_u W/g_u)$) and the upper state energy (E_u/k) under the LTE condition. Fitting the observation with Equation (3.13), we can determine column density and rotational temperature with high accuracy. The temperature derived from the population diagram reflect rotational temperature of gas and independent of the bulk motion of gas.

Figure 3.9 shows the plot of $\mathrm{In}(\gamma_u W/g_u)$ which is derived from the observed integrated intensity before and after ingress as a function of the upper state energy of SO_2 (Table 3.2). Partition function of SO_2 is referred from Exomol database (http://exomol.com/db/SO2/32S-16O2/ExoAmes/32S-16O2__ExoAmes.pf, see also Underwood et al., 2016). We also plot the linear regression lines with solid line.

Before ingress, the observations with lower three upper state energies matched to the linear lines in all region. The derived temperatures are from 100 to 160 K. The points of SO_2 332.091 GHz emission which has highest upper state energy (E_U/k = 219.53 K) greatly deviated from the fitted lines. The result shows the dayside atmosphere consists of multiple gases with different temperatures. This suggests that the atmosphere has different sources of volcanism and sublimation, and/or non-uniform vertical temperature profile. On the other

hand, after ingress, the observations in Region 2 and 3 are fitted by a linear line well. It shows the atmosphere in these regions had a single temperature and with RTE (Rotational Thermal Equilibrium). The temperature in Region 3 (311±41 K) became much hotter than that in Region 2 (182±16 K). The observation in Region 4 also closed in RTE relative to that before ingress. Only in Region 1, the observation did not follow the linear line and the atmosphere kept the same temperature characteristics as before ingress.

We speculate properties of the atmosphere in each region from observation results mentioned above. In Region 2, the main source of the atmosphere was sublimation. Before ingress, temperature of the upper atmosphere is higher than that of the lower atmosphere because of plasma collisional heating. As shown in subsection 1.2.3, the modeling study of Wong and Smyth (2000) shows atmospheric temperature increases from 400 K near the surface to 2300 K at 500 km in the low density case. The increase in the temperature in high altitude is caused by the plasma impact to Io's dayside atmosphere. After ingress, the high altitude atmosphere diminished extremely and the source of emission was dominated by the sublimation atmosphere at lower altitude. Wong and Smyth (2000) also shows the exobase height is 465 km (maximum) near the subsolar point, but drop by 30 km (minimum) at SZA = 90 degrees. These modeling study supports the diminish of the sublimation atmosphere at high altitude in eclipse. In Region 3, before ingress, both sublimation and volcanism generated the atmosphere. After ingress, sublimation atmosphere and upper atmosphere diminished, and the atmosphere is dominated by gases heated by the lava or emitted from volcanic vent. We did not detect high velocity component in Region 3 before and after ingress. It is speculated that gases did not have velocity enough to reach high altitude even if the plume was present. In Region 1, direct volcanic input mainly generated the atmosphere. The gases had the velocity enough to supply neutrals to Io's upper atmosphere directly. Therefore, the upper atmosphere did not decrease significantly and consisted of multiple temperature gases after ingress. The situation of Region 4 is similar to Region 2. However, the contribution of volcanism in Region 4 is a bit larger than in Region 2.

We also plotted the population diagram of low and high velocity components in Region 1 (Figure 3.10). If the multiple temperature is due to the source of sublimation and volcanism, temperature of the high velocity component was expected to be higher than that of the low velocity component. However, we could not detect the difference of temperature from the observation.

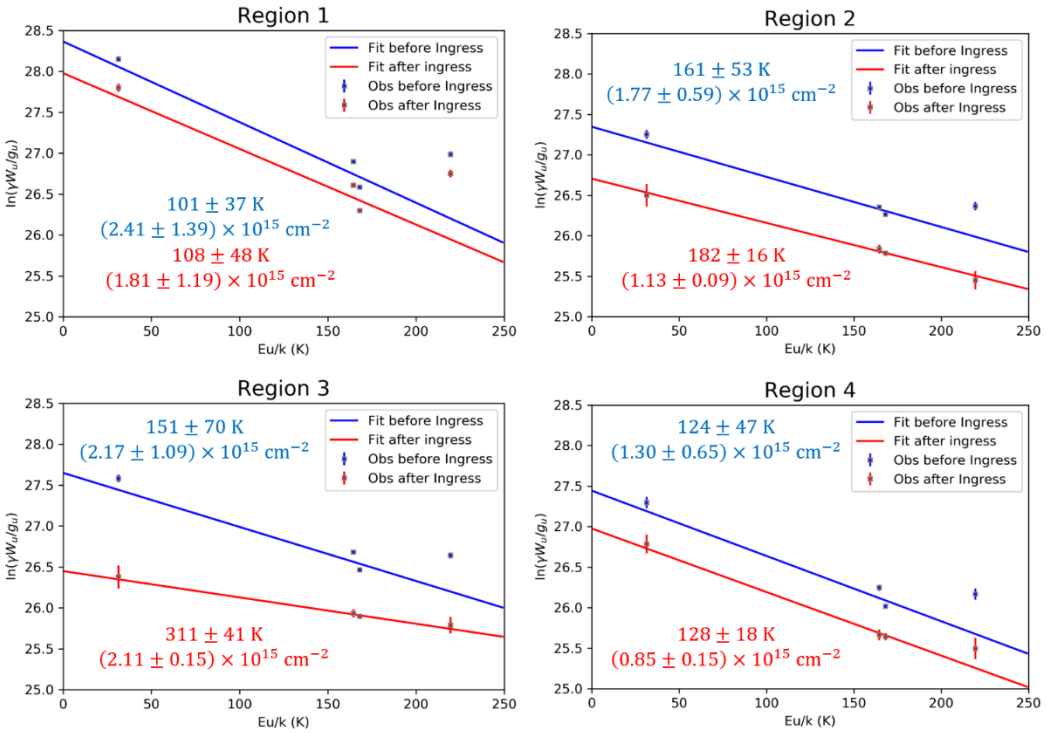

Figure 3.9. Population diagrams of Io's SO_2 atmosphere in four regions before (blue) after ingress (red). The values in the top or bottom are estimated rotational temperature and column density. Definitions of x and y axis are shown in the text. Square marks with error bars show the observation results and solid lines show linear fitting of the observation.

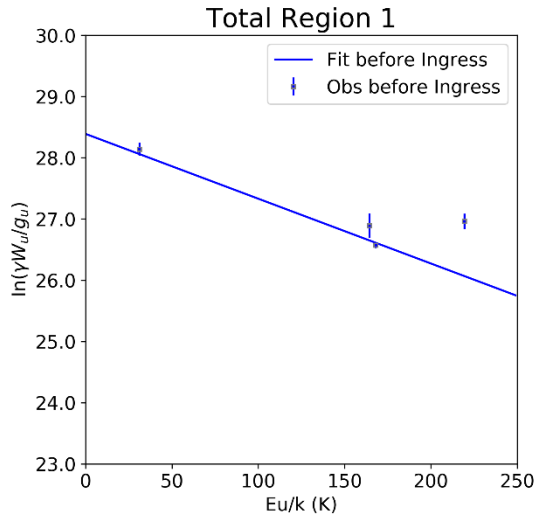

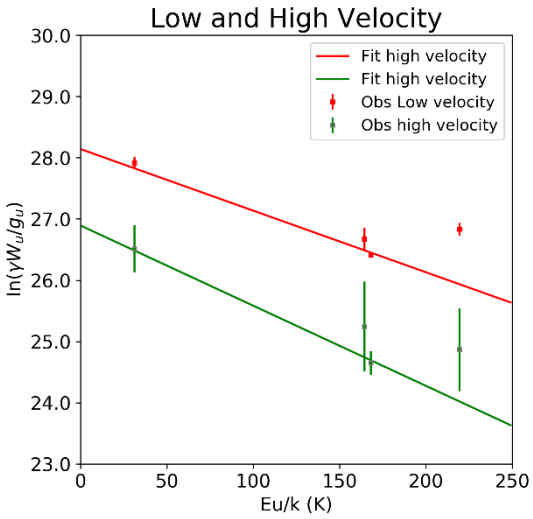

Total column density and temperature
95±28 K, (2.21±1.12)×10^{15} cm^{-2}

Low velocity
99±33 K, (1.87±1.01)×10^{15} cm^{-2}
High velocity
76±13 K, (0.36±0.13)×10^{15} cm^{-2}

Figure 3.10. (Right) Same as Figure 3.9 in Region 1, but the fitting line is the composite line of two Gaussian functions explained in Section 3.2.3 (Left) Population diagram of low (red) and high velocity components (green) of SO_2 emissions in Region 1. Solid lines show the best fitting lines and dotted lines show the range of error bars of the rotational temperature.

3.3.2 Hisaki and ground-based observations in the same period

Finally, we show the changes of IPT and sodium nebula emissions around the ALMA observation (Figure 3.11) to identify the response of neutrals and ions in the torus to volcanism. ALMA observation period was March 3 (Day of year (DOY) 79) in 2018. We could not find the change of IPT intensity on the dawn side. However, the brightness on the dusk side gradually increased from about DOY 240 in 2017 and the peak emission lasted from DOY 340 in 2017 to DOY 120 in 2018. Morgenthaler et al. (2019) also observed the change of 11-day running median of intensity of Na emission between 20-25 R_J from Jupiter in the same period. The Na emission increased from January to the beginning of March in 2018, and the peak lasted for one month. McGrath and Johnson (1986) showed supply rate of material from Io's atmosphere to IPT increases with the exobase height increasing. We estimated the initial velocity of neutrals from volcanic vent is 0.6 km/s from Doppler shift of low and high velocity component in Region 1 shown in section 3.2. We consider that the plume increased the exobase height, atmospheric sputtering area increased and then supply rate of neutrals and ions to the torus increased.

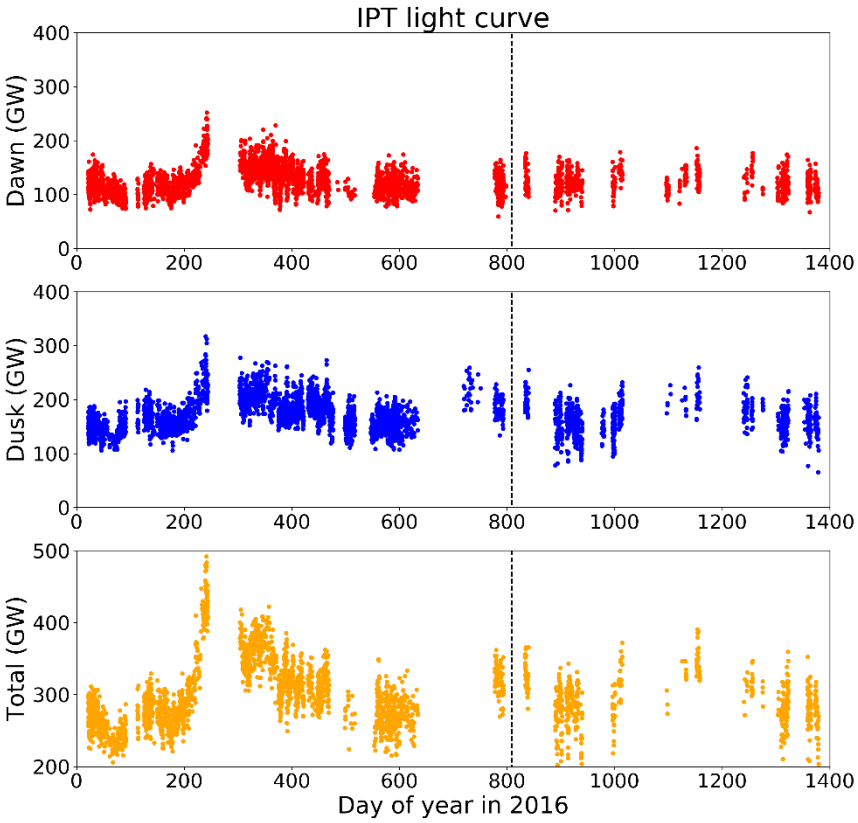

Figure 3.11. IPT light curve on the dawn and dusk sides in 2017-2018 (Kita et al., 2019, private communication).

3.4 Summary

We showed spatial and velocity distribution and the ratios of integrated intensity of SO_2 emissions by analyzing ALMA archive data. Summary of this chapter is as follows;

1. SO_2 emission maps showed the gases widely distributed around the equator of Io where the sublimation of the surface frost mainly occurs. We also found presumed volcanically active areas in the east side northern high latitude (Region 1) and the west side near the equator (Region 3).
2. Before ingress, high and low velocity components are clearly identified in Region 1. The result shows large volcanic plume generated complex atmospheric dynamics and some part of SO_2 gas flew at the line of sight direction.
3. After ingress, rotational temperature of SO_2 in Region 3 is 311±41 K, much higher than temperature of sublimation atmosphere. It might reflect the temperature of gases which are emitted form volcanoes or/and heated by hot lava lake.
4. Enhancements of sodium nebula and IPT were observed in the same period of the ALMA observation. The direct volcanic input of SO_2 gases may trigger the enhancement of Io neutral and plasma torus.

Chapter 4 Io's neutral oxygen cloud

In this chapter, we examine the detailed spatial distribution and transient change in ultraviolet emissions from Io's extended neutral oxygen cloud by using Hisaki/EXCEED data. The data analysis methods are presented in Section 4.1. Distribution of equilibrium neutral oxygen cloud estimated from azimuthal and radial distribution of OI around Io's orbit is described in Section 4.3. First detection of the time variation of the neutral cloud around Io in 2015 is given in Section 4.2. Transient change of neutral oxygen cloud is shown in Section 4.4.

4.1 Data analysis

4.1.1 Contamination of foreground emissions

Airglow emissions of oxygen ions (83.4 nm) and oxygen atoms (130.4 nm) in the terrestrial ionosphere and exosphere (geo-corona) are mainly excited by resonant scattering of sunlight. To research the influence of the foreground emissions in the geo-corona compared to emissions from the Io plasma torus and the neutral cloud, spectral images were observed at 5 arc min (13 R_J) offset position from Jupiter (hereinafter called "off-Jupiter mode") once a day from November 2014 to May 2015. Figure 4.1 indicates the schematic drawing of Hisaki observation, and counts of HeI 58.4 nm, O II 83.4 nm, Ly-α 121.6 nm and OI 130.4 nm as a function of Hisaki local time. The figures show that the foreground emissions at OII 83.4 nm and OI 130.4 nm are significantly reduced when the Hisaki's local times are between 20:00 and 04:00. In this study, we only used the Hisaki's local time to avoid contamination of the foreground emissions, in the same fashion as Yoshioka et al. (2017).

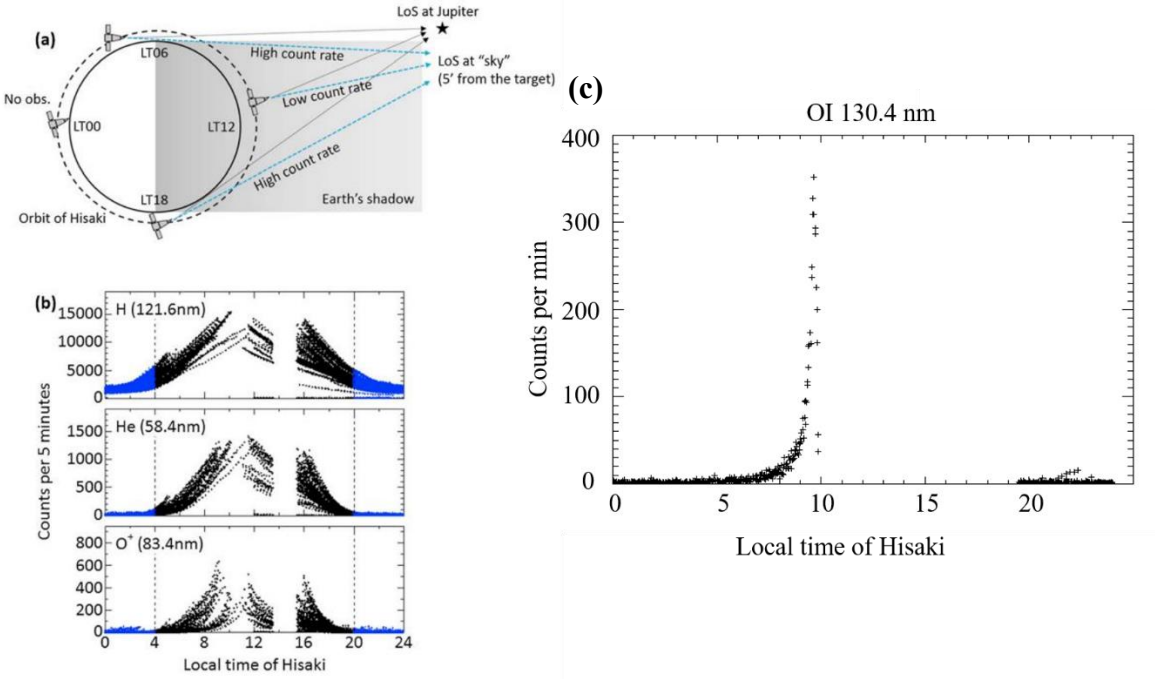

Figure 4.1. (a) Geometry of Hisaki observation viewed from the north of Earth (Yoshioka et al., 2017) (b) Counts rate of HI 121.6 nm (top), HeI 58.4 nm (middle) and OII 83.4 nm (bottom) as a function of Hisaki local time (Yoshioka et al., 2017) (c) Counts rate of OI 130.4 nm as a function of the local time. The period is from 27 November 2014 to 31 December 2014.

4.1.2 Oxygen corona and neutral cloud around Io

An example of spectral image composited around Io is shown in Figure 4.2. To monitor change of main component of Io's atmosphere, we tracked the integration range to Io's motion. There are two major oxygen emissions at 130.4 and 135.6 nm in the wavelength range of EXCEED. However, only 130.4 nm emission was used in this study because the second order of SIII 68.0 nm overlapped with the 135.6 nm emission (疋田他 2017). Figure 4.3 shows spectra averaged within ±23 arcsec (±~1.2 R_J) around Io in the wavelength range of 129.0-131.0 nm before and after subtracting geo-corona. The OI 130.4 nm line is composed of triplet of 130.217 nm, 130.486 nm, and 130.603 nm components. EXCEED cannot resolve the triplet but the triplet broadens the total line profile in the spectral image. Notably, the data still contained the emissions from atomic oxygen in the geo-corona and contamination by high-energy electrons trapped in the radiation belt. The contamination was not negligible compared to the emissions from a neutral cloud and was removed by subtracting the data collected in off-Jupiter mode from that collected in on-Jupiter mode.

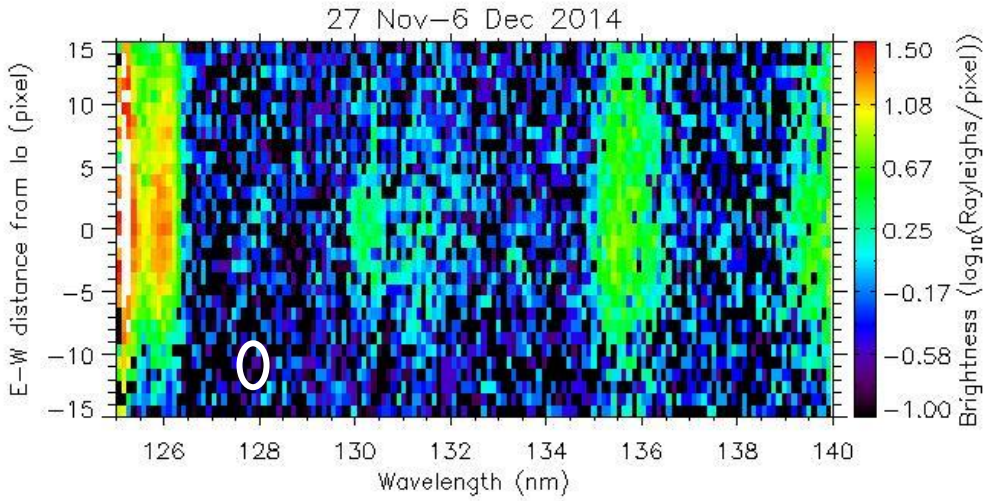

Figure 4.2. Spectral image taken at ±60 arc sec (±~3.0 R_J) around Io in case of the dawn side (Io's orbital phase was 45-135°) obtained by EXCEED averaged from 27 November 2014 to 6 December 2014 as a function of wavelength and east-west pixel distance from Io. One pixel corresponds to about 4.2 arc sec in the spatial direction and 0.1 nm in the wavelength direction. White ovals indicate typical point spread functions of EXCEED. Color contours of brightness are logarithmic. Geo-corona emission is subtracted. This spectral image shows atomic oxygen emission at 130.4 nm was mainly distributed within 1 R_J around Io.

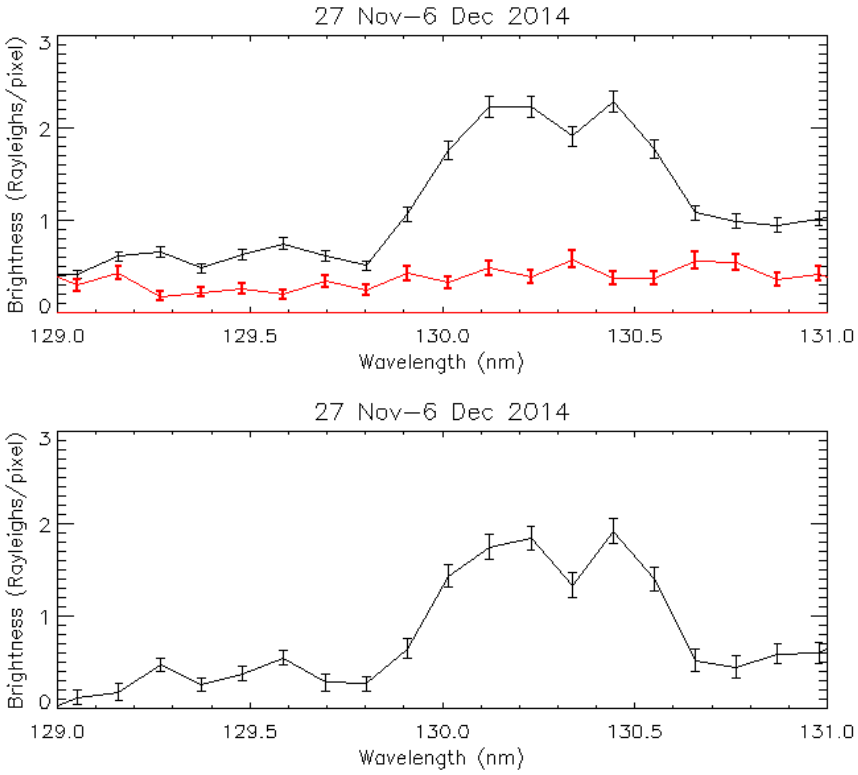

Figure 4.3. (Top) The spectrum obtained by EXCEED averaged from 27 November 2014 to 6 December 2014. The black line was taken at ±23 arc sec (~1.2 R_J) around Io from 129.0 nm to 131.0 nm (on-Jupiter mode). That of red line was taken when EXCEED observed only geo-corona (off-Jupiter mode). (Bottom) The spectrum of the atomic oxygen emission around Io. We subtracted red line from Black line.

4.1.3 Neutral oxygen cloud around Io's orbit

Figure 4.4 shows a spectral image for the on-Jupiter mode before the subtraction of off-Jupiter mode data (top left), a spectral image for the off-Jupiter mode (top right), and a spectral image in which the off-Jupiter mode data were subtracted from the on-Jupiter mode data (bottom left). The top left panel shows faint emission spreads out the whole area of the dumbbell-shaped slit (between 129.4-131.4 nm) and the emission brighter than the foreground emission distributes narrower than the slit in the wavelength direction. The spectral image contains emissions from both geo-corona and from neutral oxygen cloud. The top right panel shows that geo-corona emissions of atomic oxygen at 130.4 nm are also spread out over the whole area of the slit and have a uniform distribution inside the slit aperture. On the other hand, the spatial and spectral distribution of emissions at 130.4 nm in the on-Jupiter image (bottom) was narrower than the width of 129.9 - 130.8 nm and the length of the slit. These figures show that the atomic oxygen emission at 130.4 nm along Io's orbit can be derived successfully.

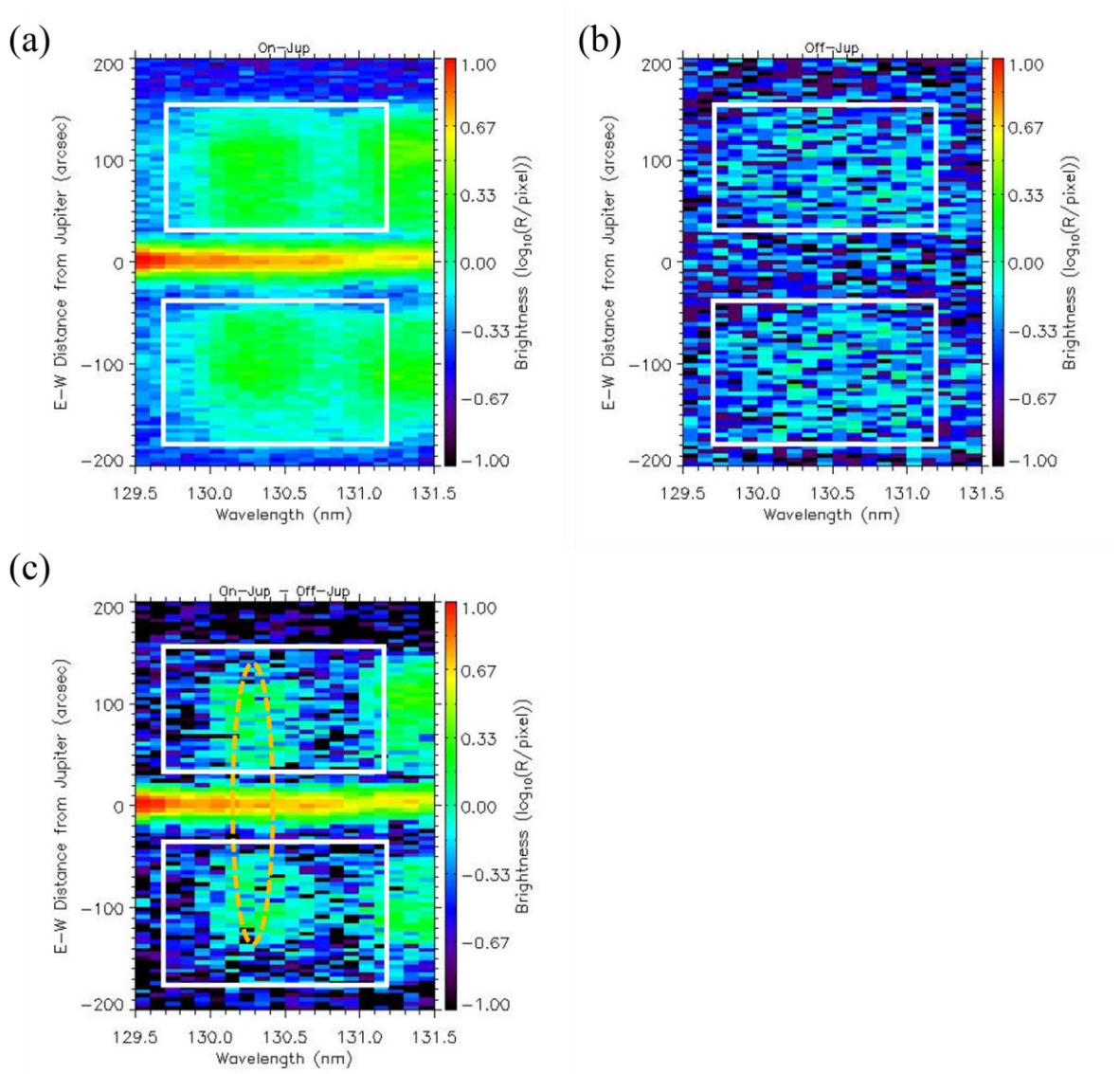

Figure 4.4 (a) Hisaki spectral image around OI 130.4 nm obtained by using a dumbbell-shaped slit from 27 November 2014 to 31 December 2014. The image is from before the subtraction of the image using the off-Jupiter mode. Logarithmic color scale shows the brightness in Rayleighs (R) per pixel. The continuous emission around the center of the slit (0 arcsec) is from Jupiter's aurora. The emissions from 131.0 nm to 131.5 nm are the second order emission of the SIV 65.7 nm multiplet. (b) Spectral image using the off-Jupiter mode for the same slit. (c) Spectral image around OI 130.4 nm using the same slit after the image from the off-Jupiter mode was subtracted from that of the on-Jupiter mode. White solid lines show the FOV for OI 130.4 nm emission. The dashed orange oval shows the expected position of Io's neutral oxygen cloud.

4.2 Equilibrium distribution of neutral oxygen cloud

In this section, we derive equilibrium spatial distribution of Io's neutral oxygen cloud observed from 27 November 2014 to 31 December 2014 (35 days). This period was volcanically quiet because atomic oxygen and sodium emissions originating from Io were weak and stable compared to the volcanically active period around February 2015 (see subsection 4.2.1).

4.2.1 Result 1 - Azimuthal distribution

Figure 4.5 shows the dependence of atomic oxygen emissions at 130.4 nm on the Io phase angle (IPA) averaged over the radial distance ranges of 4-5 R_J, 5-6 R_J and 6-7 R_J from Jupiter on the dawn and dusk sides. Two important features can be derived from these figures. First, the emissions show asymmetry with respect to IPAs of 90° and 270° (green lines in Figure 4.12). The averaged brightness in the IPA range of 60-90° on the dawn side and that of 240-270° on the dusk side are significant between 5-6 R_J and 6-7 R_J. Only the emissions at 6-7 R_J on the dusk side show symmetric distribution around the peak. Second, a weak and longitudinally uniform (or homogeneous) emission of atomic oxygen is clearly visible.

We propose a simple model to explain these observations (Figure 4.6). The oxygen cloud consists of two components, namely, a dense region distributed around Io (often called the "banana cloud") and a longitudinally uniform, diffuse region distributed along Io's orbit. The candidates of the distribution of the banana cloud that could cause asymmetric distribution with respect to IPA are as follows (Figure 4.7):

1. A leading cloud that spreads inside Io's orbit (cloud A)
2. A leading cloud that spreads outside Io's orbit (cloud B)
3. A trailing cloud that spreads inside Io's orbit (cloud C)
4. A trailing cloud that spreads outside Io's orbit (cloud D)

In the cases of cloud B and cloud C, the averaged brightness at 5-6 R_J in the IPA range of 60-90° should be smaller than that of 90-120° on the dawn side, which does not match the observations. In the case of cloud A and cloud D, the averaged brightness at 5-6 R_J of 60-90° is larger than that of 90-120° on the dawn side, which is consistent with the observations. However, in the case of cloud D, the averaged brightness at 6-7 R_J of 60-90° is smaller than that of 90-120° on the dawn side; this does not match the observations. Cloud A, a leading cloud that spreads inside Io's orbit, is thus the most plausible distribution that can explain the observations in the dawn side. We can explain that cloud A is also the most plausible distribution in the dusk side by similar explanation. This shape of the cloud estimated by Hisaki observations is generally consistent with previous models (Smyth & Marconi, 2003; Smyth & Shemansky, 1983).

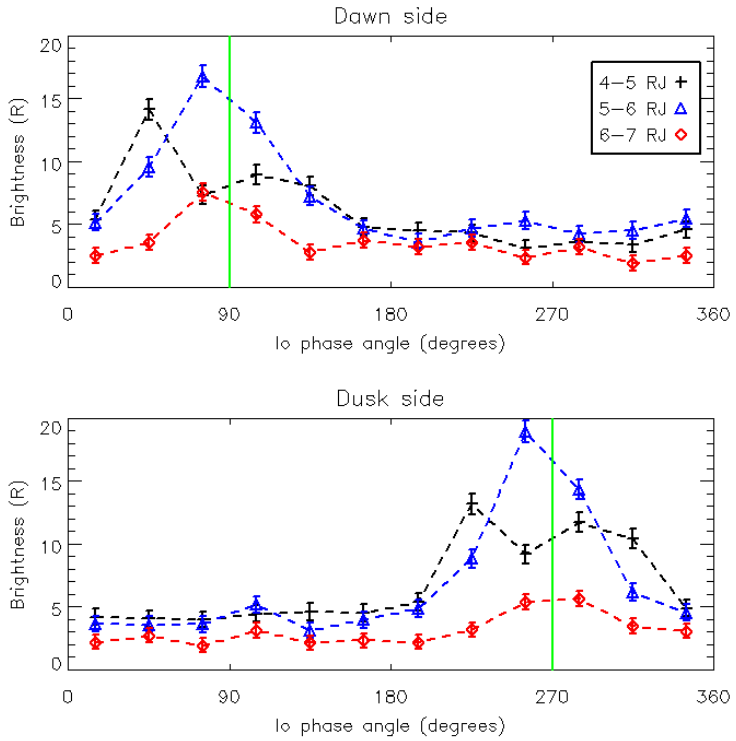

Figure 4.5. (Top) The Io phase angle dependence of atomic oxygen emissions at 130.4 nm at the radial distance of 4-5 R_J (black), 5-6 R_J (blue), and 6-7 R_J (red) from Jupiter on the dawn side. Each data point was averaged in the Io phase angle (IPA) of every 30°. (Bottom) Same but on the dusk side. The longitudinal distribution show the brightness asymmetry with respect to the IPA of 90° (dawn side) and 270° (dusk side).

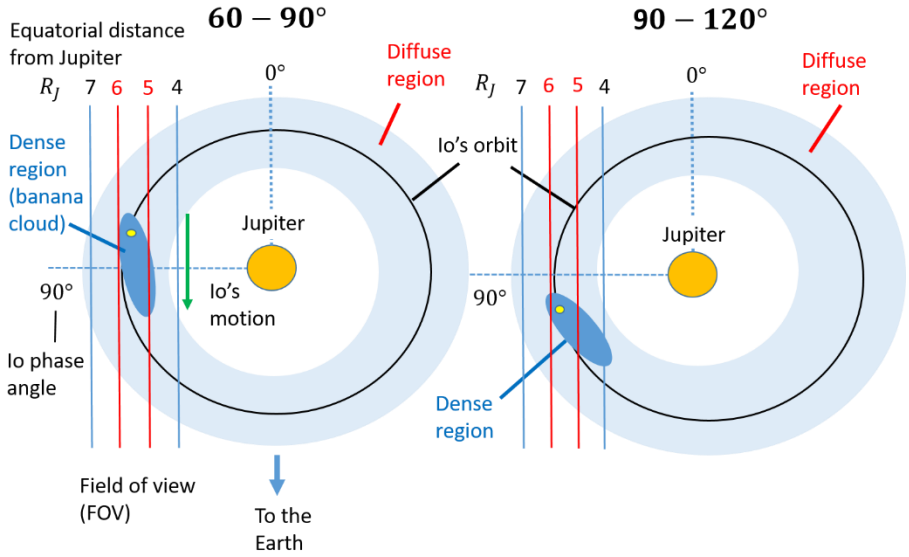

Figure 4.6. Schematic drawings of the distribution of atomic oxygen for the cases of the Io phase angle of 60-90° (left) and that of 90-120° (right). The dense region (banana cloud) mainly extends forward and inside Io's orbit. The diffuse region is distributed uniformly in the azimuthal direction, and the brightness decreases with increasing distance from Io's orbit.

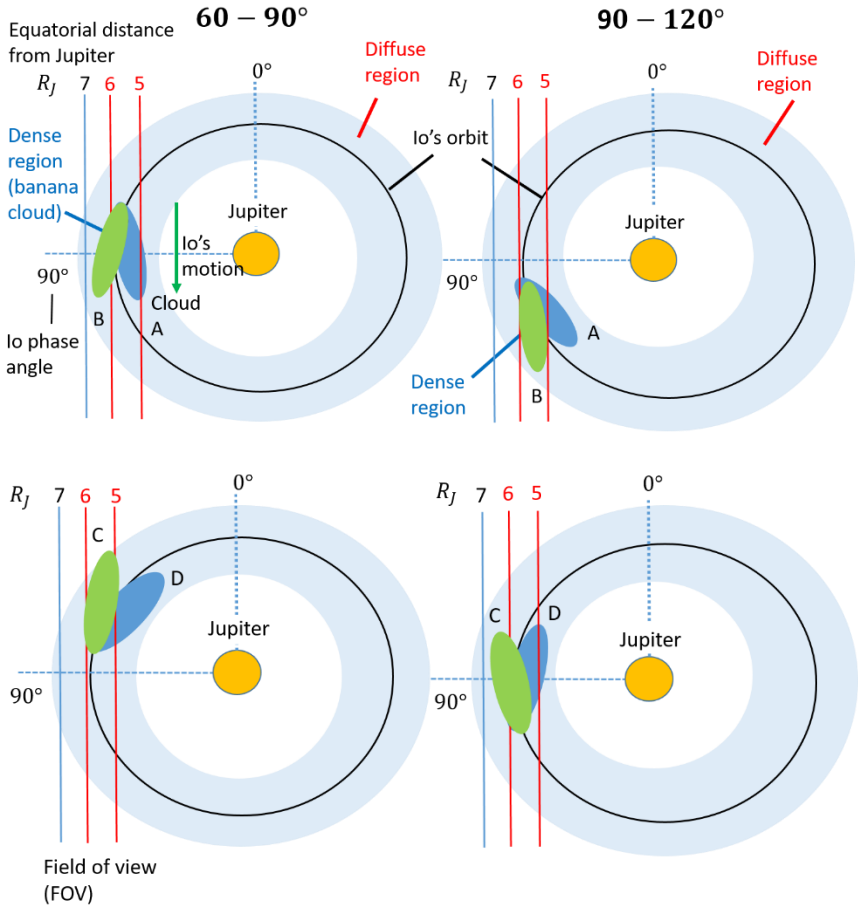

Figure 4.7. Schematic images of candidates of Io's neutral oxygen banana cloud (Cloud A-D, see text) and the diffuse region around Io's orbit. Blue (green) clouds mainly distribute inside (outside) Io's orbit.

4.2.2 Result 2 – Radial distribution

Figure 4.8 shows the radial distribution of atomic oxygen emissions as a function of the radial distance from 4 to 8 R_J on the dawn and dusk sides. The apparent radius of Jupiter changed from 19.7 to 21.6 arcsec over the observation period. To correct for the influence of this apparent scale change, we resampled the spatial step of the Hisaki data to be 0.2 R_J each day before accumulating images Red and blue marks in the figure show the radial profiles in the IPA ranges of 60-90° (Io is on the dawn side) and 240-270° (Io is on the dusk side), respectively. Black marks show the longitudinally averaged radial profile. The profile of atomic oxygen emissions around Io changes at around 6 R_J. This indicates that there is a boundary near 6 R_J between the inner banana cloud and the outer diffuse region.

The maximum brightness of atomic oxygen emissions is found inside Io's orbit. This suggests that the dense region extends inside Io's orbit rather than outside. The brightness of atomic oxygen around Io on the dusk side is larger than that on the dawn side, especially

between 5.0-5.8 R_J. Atomic oxygen emissions are partly excited by electron impact. Electron temperatures also shows a dawn–dusk asymmetry which may be due to the dawn–dusk electric field in the Jovian magnetosphere (Barbosa & Kivelson, 1983; Ip & Goertz, 1983), and the electron temperature is higher on the dusk side than on the dawn side. The dawn–dusk asymmetry of the atomic oxygen cloud emissions reflects the asymmetry of the electron temperature similar to that reported by Oliversen et al. (2001) near Io. The asymmetry of the atomic oxygen emissions around Io was found continuously throughout the period from November 2014 to May 2015. The detail discussion of the asymmetry is shown in section 5.1.

We also found that the observed emissions extend out to 7.6 R_J. Radial and azimuthal distributions of OI 130.4 nm emissions observed in this study suggest that the atomic oxygen is not confined in the Io corona and the banana cloud but is also distributed around equational plane in the Jovian inner magnetosphere.

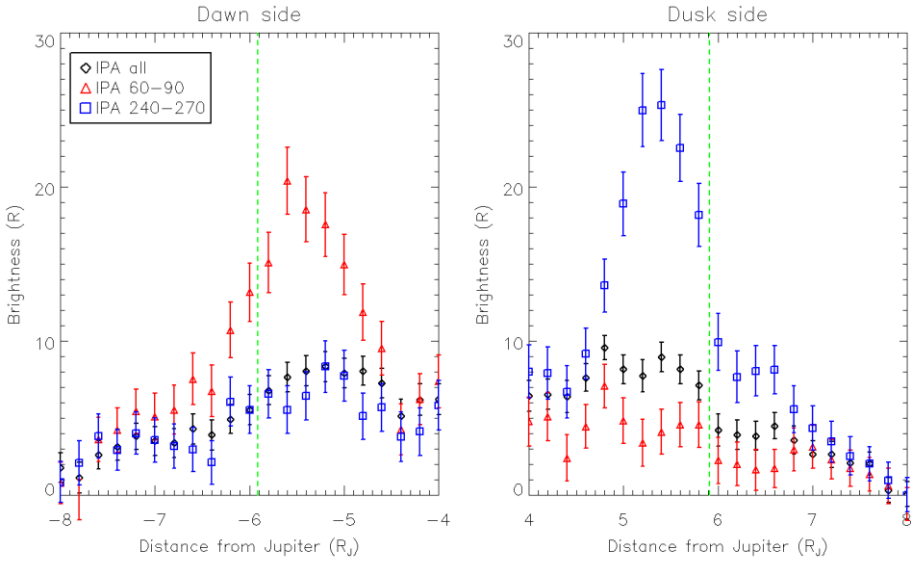

Figure 4.8. (Left) The radial distribution of dawn side atomic oxygen emissions at 130.4 nm. The radial range was chosen as 4 to 8 R_J from Jupiter on the dawn side. Red triangles represent the profile averaged in the Io phase angle (IPA) range of 60-90°, and blue squares represent the profile averaged in the IPA range of 240-270°. Black diamonds represent the profile averaged over the entire IPA range. The observation period is the same as Figure 1. Green broken line shows the position of Io's orbit. (Right) same as the left panel but on the dusk side.

4.2.3 Radial profile of oxygen number density

We have developed an emission model of atomic oxygen that enabled us to calculate the radial profile of atomic oxygen emissions as seen by an observer. The radial distribution of the atomic number density, the electron density, and the electron temperature are used as input parameters. By comparing the longitudinally-averaged radial profile observed by Hisaki with the distribution of model brightness, we estimated the radial distribution of the atomic oxygen number density. In this study, we assumed that the plasma parameters are longitudinally uniform. We then used the following equation to calculate the model brightness:

$$\mathrm{B}(r) = \frac{2}{10^6} \int_{s=0}^{s=\sqrt{R_{out}^2 - r^2}} \epsilon\left(\sqrt{r^2+s^2}\right) \cdot n_O\left(\sqrt{r^2+s^2}\right) ds\,. \tag{4.1}$$

where r is the equatorial distance from Jupiter; s is the line of sight distance; R_{out} is the distance of the outer edge of the cloud; we assumed R_{out} = 10.0 R_J in this study; ϵ is the emissivity of atomic oxygen emissions per oxygen atom (photons/s). n_0 is the number density of oxygen atoms (cm^{-3}). The geometry of the line of sight integration is shown in Figure 4.9.

Atomic oxygen emissions at 130.4 nm are excited by both solar resonant scattering and electron impact. The emissivity of per atom (ϵ, photon/s) in the Io plasma torus is given by (Skinner & Durrance, 1986)

$$\epsilon = \mathrm{n_e}\alpha(T_e) + g_i, \tag{4.2}$$

where n_e and T_e are the electron density and temperature in the torus, respectively, α is the rate coefficient of electron impact excitation of oxygen atoms, and g_i is the unit emission rate for solar resonance scattering. Figure 4.10 shows the radial profile of electron density, temperature, and emissivity at 130.4 nm. We used the electron temperature and density parameters of Bagenal (1994) (derived from the Voyager data) for inside Io's orbit. Outside Io's orbit we use the profile derived from Hisaki data by Yoshioka et al. (2017) which is similar to that of Bagenal (1994) between 6 and 7.5 R_J but, unlike at Voyager, does not drop between 7.5 and 8.0 R_J (which is called the "ramp" region), but continues with a constant slope. We then used the CHIANTI database version 8.0 (Del Zanna et al., 2015) to calculate the emissivity by electron impact excitation ($n_e\alpha(T_e)$). We calculated the emissivity by resonance scattering with the solar spectral irradiance data from the Solar Radiation and Climate Experiment (SORCE, Woods & Rottman, 2005) satellite (g_i = 5.37×10^{-7} photons/s). A detailed method to calculate the emissivity is described in subsection 4.2.2.

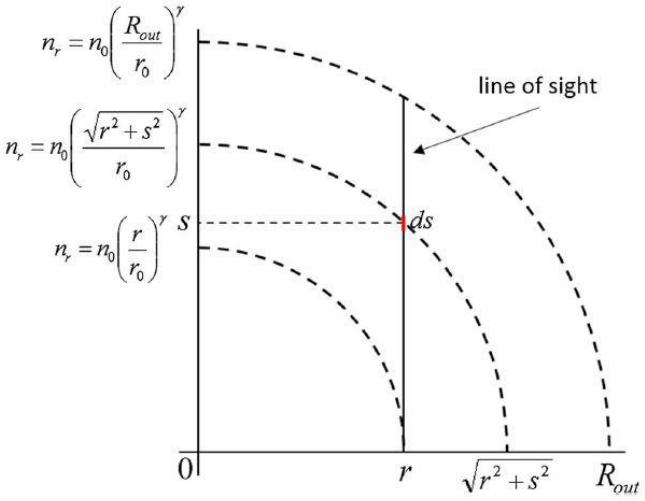

Figure 4.9. Geometry for the line of integration (Yoshioka et al., 2017).

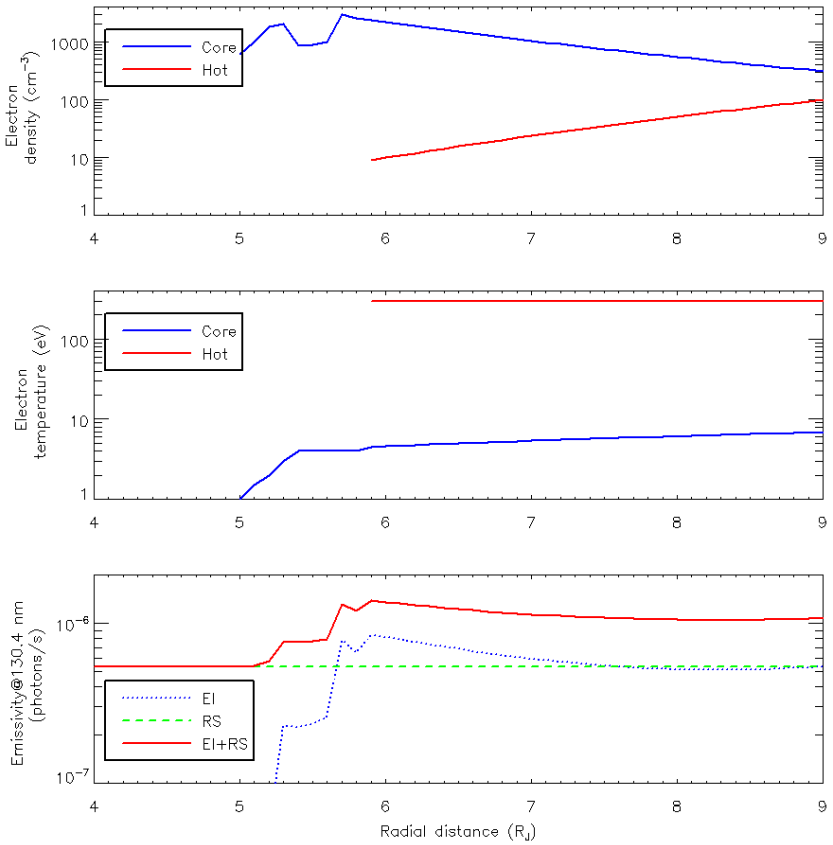

Figure 4.10. (Top and middle) The radial profile of electron density and temperature. The electron density and temperature profiles inside Io's orbit are from Bagenal (1994), and those outside Io's orbit are from Yoshioka et al. (2017). (Bottom) The emissivity of atomic oxygen emissions at 130.4 nm. The EI (blue dots), RS (green dashes) cases are where only electron impact excitation and solar resonance scattering were considered, respectively. EI + RS (red line) shows the case where both effects were considered.

We searched for a radial profile of the oxygen number density that matched the profile of atomic oxygen emissions observed by Hisaki. In this study, we assumed that the north–south thickness of Io's neutral oxygen cloud is 24 arcsec (which corresponds to approximately ±0.6 R_J). Another assumption was that the radial profile of the oxygen number density could be approximated by a power law with inflection points at 5.7 R_J and 5.9 R_J. Figure 4.11 shows the best fit radial profile of the number density (red line in the top panel) and the corresponding radial profile of atomic oxygen emissions (red line in the bottom panel). The red and blue diamonds with error bars show the observed profile of OI 130.4 nm on the dawn and dusk sides, respectively. The estimated oxygen number densities are 80 cm^{-3} at 5.7 R_J and 40 cm^{-3} at 5.9 R_J, and the power law slope from 4.0 R_J to 5.7 R_J is 5.3. This result is larger than the lower limit (29±16 cm^{-3}) estimated from rocket-borne FOT (Faint Object Telescope) observations (Skinner & Durrance, 1986). The black line of the top panel shows the oxygen density profile used in the model of Schreier et al. (1998). We found that there are more oxygen atoms in this study compared to the Schreier et al. (1998) modeling study (tied to Voyager observations), especially inside 5.7 R_J. Delamere et al. (2004) used a physical chemistry model matched to Cassini Ultraviolet Imaging Spectrometer (UVIS) observations to estimate the atomic oxygen density at ~6.0 R_J. They found that the density was about 25 cm^{-3} during inactive periods, rising to 120 cm^{-3} during the volcanically active period observed as Cassini approached Jupiter. Our results are in the range of their estimation.

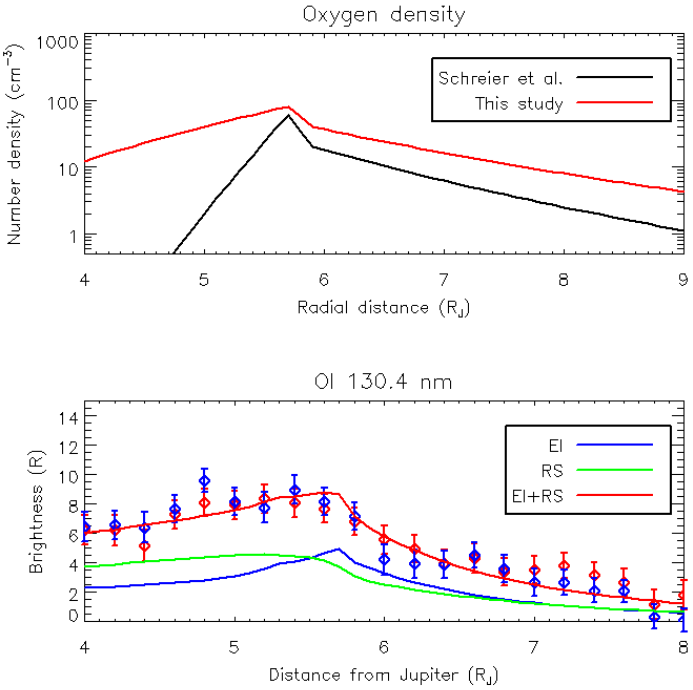

Figure 4.11. (Top) The radial profile of oxygen atoms. The black line shows the profile used by Schreier et al. (1998). The red line shows the profile derived in this study based on the Hisaki observations. (Bottom) The radial profiles of observed atomic oxygen emissions at 130.4 nm are shown for the dawn side (red diamond) and dusk side (blue diamond). Red solid line (EI + RS) shows the model brightness where the oxygen density profile given by the red line in the top panel was used. EI (blue) and RS (green) show contributions of electron impact excitation (EI) and solar resonance scattering (RS), respectively.

4.2.4 Discussion

Primary loss process of atomic oxygen in the Io plasma torus is electron impact ionization. The ionization rate depends on both electron density and temperature. Since the electron density and temperature both decrease inward from 5.7 R_J, more oxygen atoms survive inside Io's orbit. Outside Io's orbit, oxygen atoms are ionized by electron impacts more frequently. Therefore, the banana cloud mainly extends inside Io's orbit rather than outside Io's orbit. The distribution of Io's neutral clouds caused by the non-uniform interaction with the Io plasma torus has been explained in the case of sodium (Burger & Johnson, 2004; Smyth & Combi, 1988) and in the case of sulfur and oxygen (Smyth & Marconi, 2003, 2005).

Neutrals escaping from Io's atmosphere and from Io's gravity comprise two populations: slow neutrals (with velocities of several kilometers per second) and faster neutrals (with velocities of many tens to hundreds of kilometers per second) (Smyth & Marconi, 2003). The slow neutrals are produced by atmospheric sputtering. The faster neutrals are the tail component of

the sputtering distribution or are produced by chemical reactions such as charge exchange processes between corotating oxygen ions and neutrals. The neutral clouds around Io's orbit are mainly populated by slow velocity neutrals. Fast neutrals tend to move quickly both radially inward and outward from Io's orbit and contribute to the formation of more extended neutral clouds around Jupiter (Smyth & Marconi, 2003).

The observations by Hisaki show that the banana cloud near Io spreads in the leading direction (Subsection 4.3.1). The ejection velocity and direction from Io are considered to make a difference between the banana cloud and the diffuse region in Io's neutral oxygen cloud. It is possible that oxygen atoms whose initial velocity is near 2.6 km/s (Smyth and Marconi, 2003) and that are ejected on the trailing side, may mainly create the banana cloud, and oxygen atoms whose initial velocity is much larger than 2.6 km/s or those that are ejected on the leading side may mainly create the diffuse region. However, to test this hypothesis, we need a model that we can compare with the observations of Io's neutral oxygen cloud in order to constrain the velocity distribution of escaping neutrals from Io.

4.3 Time variations of O around Io

4.3.1 Results

We analyzed time variations of OI emission around Io during two observation periods from 19 December 2013 to 24 April 2014 ("season 1") and from 27 November 2014 to 14 May 2015 ("season 2"). The spectrograph data observed when Io's phase angle was 45-135° (225-315°) was treated as the dawn (dusk) side data.

The time variation of atomic oxygen emission at 130.4 nm (±23 arcsec (±~1.2 R_J) around Io) and brightness of sodium nebula emission at the D-lines (50 R_J from Jupiter) observed from the ground during seasons 1 and 2 are shown in Figures 4.12 and 4.13, respectively. Atomic oxygen emission did not vary remarkably during season 1. On the other hand, both atomic oxygen and sodium emissions vary significantly during season 2. The brightness of atomic oxygen emission stayed within 10–15 R until Day of Year (DOY) 20 in 2015 but then started to increase and reached a maximum intensity of more than 30 R from DOY 40 to DOY 60 in 2015. The oxygen emissions decreased to the quiet value (~10 R) by DOY 110 in 2015. These results suggest that the brightness of atomic oxygen emission around Io increased by a factor of 2.5. We also compared the spectral images taken at ±60 arc sec (±~3.0 R_J) around Io from 27 November to 6 December and from 2 February to 11 February 2015 in Figure 4.14. The figure shows the emission not only near Io but also in the torus far from Io increased in the high density period (February 2019). de Kleer and de Peter (2016) observed a brightening of 3.8-μm emission from Kurdalagon Patera in late January in 2015 which coincides well with the brightening of sodium emission as well as of atomic oxygen. The result strongly supports that the enhanced atomic oxygen emission in season 2 is associated with the volcanic activity on Io. During season 2, the duration of the atomic oxygen brightness increasing from the volcanically quiet level to the maximum and that for the sodium nebula were almost the same (30 days). On the other hand, the duration in which atomic oxygen brightness returns from the maximum to the quiet level was 60 days and that for the sodium nebula was only about 40 days. The atomic oxygen emission when Io was on the dusk side was larger than that when Io was on the dawn side throughout the periods, except around DOY 30 and DOY 105 in 2014 (season 1). The brightness of atomic oxygen emission temporary decreased from DOY 43 to DOY 48 and from DOY 54 to DOY 57 in 2015. However, this short decrease was only observed on the dawn side.

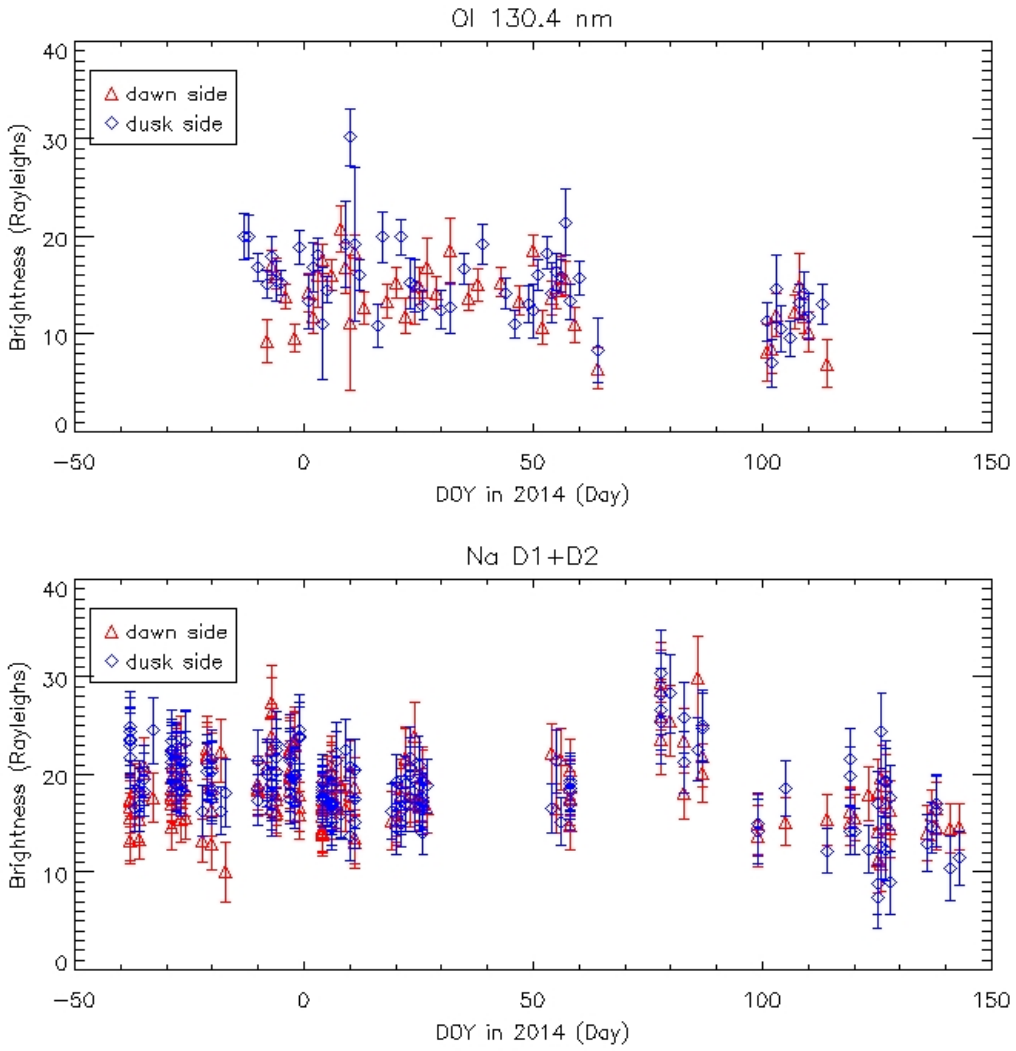

Figure 4.12. (Top) Time variations of atomic oxygen emission at 130.4 nm on the dawn and dusk sides integrated for the range of ±23 arcsec (±1.2 R_J at Jupiter's opposition) around Io and (Bottom) D1+D2 neutral sodium nebula emission obtained with ground-based monochromatic imager. The plotted period is from 19 December 2013 to 24 April 2014. Day of year (DOY) 1 2014 = 1 January 2014.

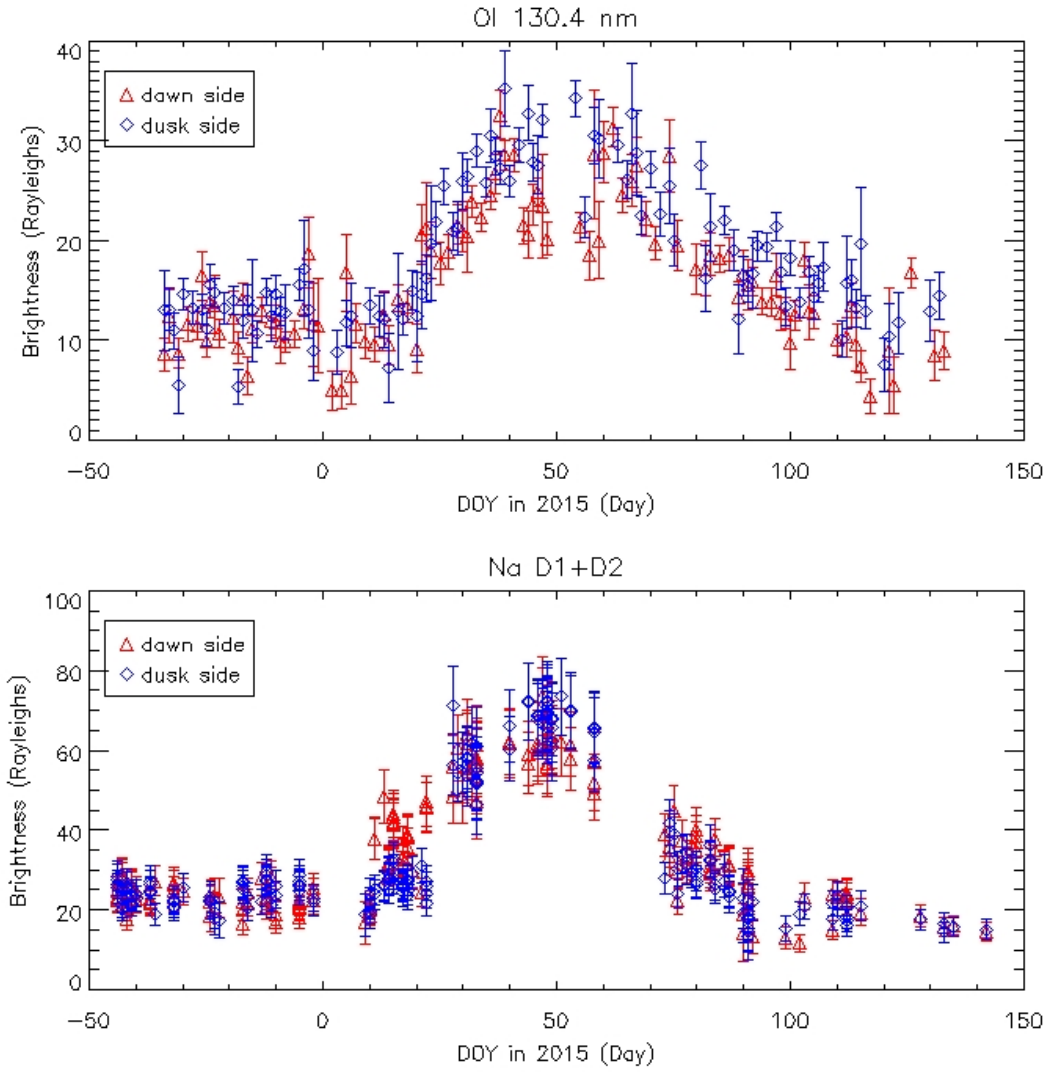

Figure 4.13. Same as Figure 4.5. But the period is from 27 November 2014 to 14 May 2015 ("season 2"). Day of year (DOY) 1 2014 = 1 January 2015.

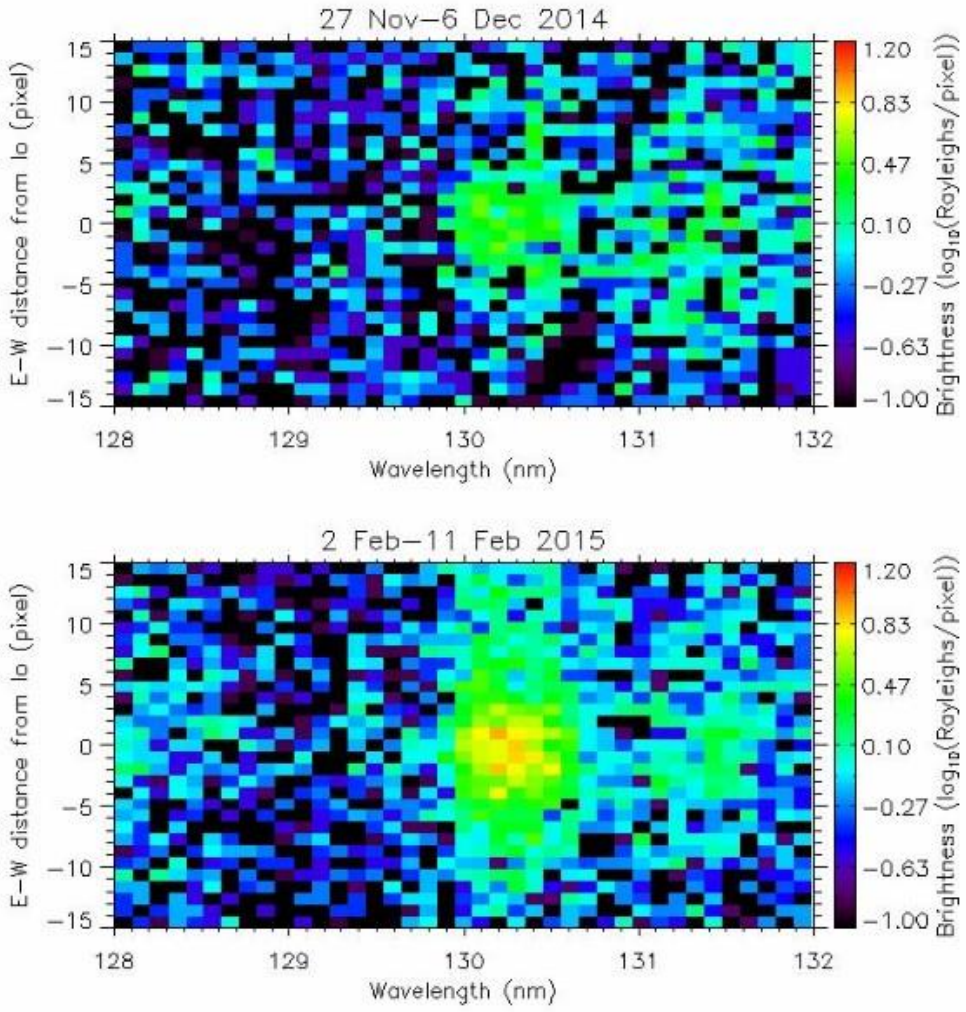

Figure 4.14. (Top) Spectral image taken at ±60 arcsec (±~3.0 R_J) around Io. Geo-corona emission is subtracted. (Bottom) Spectral image is same as top figure. However, the observation period is from 2 February to 11 February 2015.

4.3.2 O number density around Io

Since both solar resonant scattering and electron impact excitation contribute to atomic oxygen emission at 130.4 nm, the contribution from both mechanisms is estimated as follows. The brightness of solar resonant scattering (B_{RS}) can be written as (Skinner and Durrance, 1986)

$$B_{RS} = \frac{1}{10^6}\int n(z)g\,dz = \frac{1}{10^6}N(O)g \quad \text{(R)}, \tag{4.3}$$

where n(z) is the number density of atomic oxygen (cm^{-3}), N(O) is the column density of atomic oxygen (cm^{-2}) and g is the g-factor related to solar irradiance. The g-factor is given by (Barth, 1969)

$$\mathrm{g} = \pi F_\lambda \left(\frac{\pi e^2}{mc^2}\right) f \quad (\text{photons} \cdot \mathrm{s}^{-1}), \tag{4.4}$$

where f is oscillator strength (0.047, (Stone and Zipf, 1974)), $\pi e^2/mc^2$ = 8.829×10^{-13} cm, λ is wavelength, and πF_λ is solar flux of the triplet at 130.4 nm. According to measurements by the Solar Maximum Mission (SMM) around the Earth (Gladstone (1992), see Figure 4.8 and 4.9), each shape of the solar spectrum for the triplet is almost symmetric, and its line width (>0.02 nm in full width at half maximum (FWHM)) is broad compared to the range of Doppler shift of atomic oxygen emission line caused by Io's orbital motion (±~0.007 nm). According to HORIZONS database, velocities of Jupiter relative to Earth center changed from -26.5 km/s to 27.6 km/s (negative is that Jupiter is moving toward the Earth) from 27 November 2014 to 1 May 2015. They correspond to Doppler shifts of ~0.012 and ~-0.012 nm. The variation of solar irradiance for the triplet lines was smaller than 10% for Io's orbital phases 45-135° and 225-315°. Referring to the Solar Radiation and Climate Experiment (SORCE) solar spectral irradiance data (with 1.0 nm resolution) (Woods and Rottman, 2005), we set the absolute value of total solar irradiance for the triplet at 130.4 nm during the observation period as 1.75×10^{-4} (Wm^{-2}). Thus, the g-factor value is calculated as 5.36×10^{-7} (photons/s), and the brightness caused by solar resonant scattering is estimated as $B_{RS} = 5.36 \times 10^{-13} N(O)$ (R).

Atomic oxygen emission caused by electron impact excitation is estimated using two Maxwellian electron distributions. Sitter and Strobel (1987) reported two such Maxwellian distributions with different densities and temperatures in Voyager 1 data. This assumption is similar to that made in past studies based on the Hisaki data (Yoshioka et al., 2014, 2017, 2018; Tsuchiya et al., 2015, Hikida et al., 2019). Most of the electron populations consist of a core distribution of thermal electrons (around 5 eV) with a few percent of hot electrons (50-200 eV). CHIANTI (version 8.0); an atomic database allowing computation of emissivity (Zanna et al., 2015). The brightness of atomic oxygen emission at 130.4 nm depends on the core electron temperature (T_c) and hot electron fraction (f_H). However, these emissions do not vary with hot electron temperature (T_H) as long as long as this temperature remains between 50 – 200 eV (see Figure 4.10). Based on the calculations using CHIANTI, the brightness caused by electron impact excitation is estimated as:

$$B_{EI} = 7.69 \times 10^{-13} N(O) - 1.29 \times 10^{-12} N(O) \text{ (R)}, \quad (4.5)$$

under the conditions T_c = 4.5-5.5 eV, f_h = 1-3 %, T_H = 100 eV and electron density n_e = 2000 cm^{-3}. The assumed electron density was referred from Thomas et al. (2004). The assumed ranges of core electron temperature and hot electron fraction are based on Yoshioka et al. (2014).

The ratio of the contribution of electron impact excitation to that of solar resonance scattering is estimated to be 1.43-2.40. Based on this assumption, the total brightness of atomic oxygen emission at 130.4 nm is

$$B_{RS} + B_{EI} = 1.31 \times 10^{-12} - 1.83 \times 10^{-12} N(O) \text{ (R)}, \quad (4.6)$$

The brightness during the volcanically quiet periods is calculated as 12.9 R (averaged from November 27 to December 30, 2014), and the nominal atomic oxygen column density around Io (±23 arcsec (±~1.2 R_J)) was calculated as (7.05-9.85)×10^{12} cm^{-2}. Thus, a total of (3.64-5.08)×10^{32} oxygen atoms exist in the region of the field of view (46 arcsec along radial direction × 10 arcsec along north-south direction, which corresponds to 2.3 R_J × 0.4 R_J at Jupiter's opposition) surrounding Io.

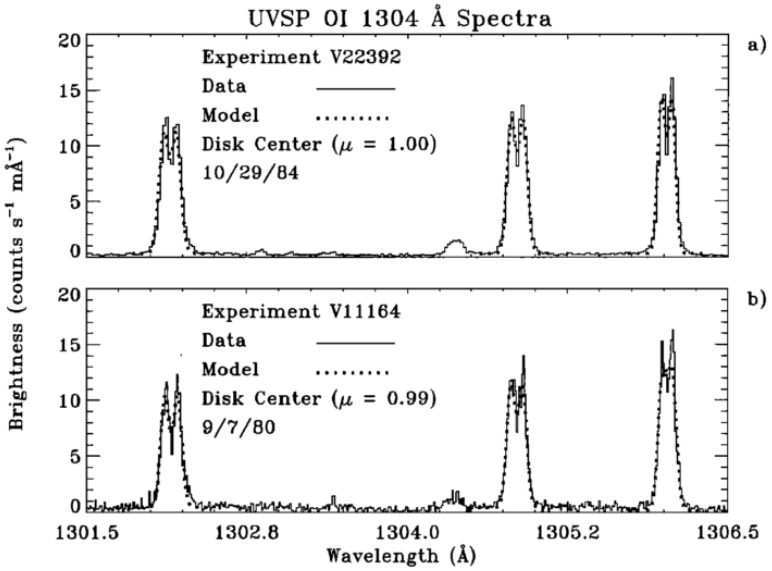

Figure 4.15. (a) SMM-measured line profiles for the disk center OI 130.4 nm triplet for solar maximum. (b) Same but for solar minimum (Gladstone 1992).

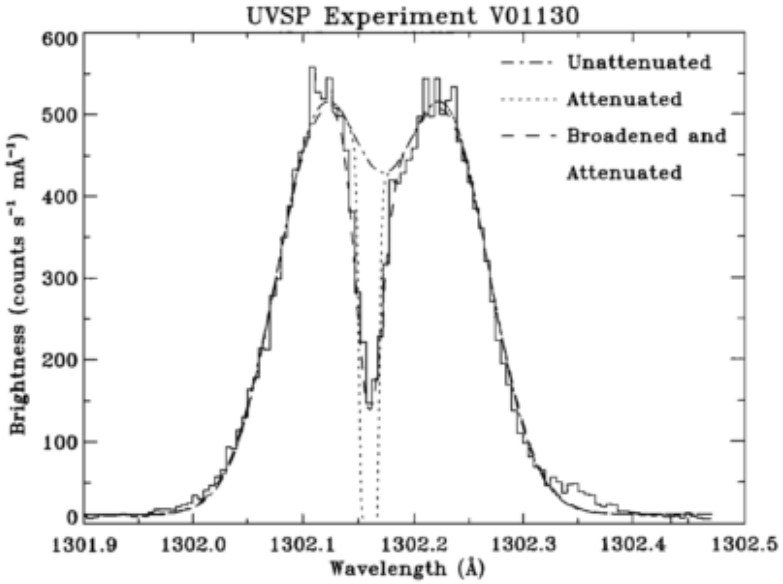

Figure 4.16. Line profiles of emission around 130.2 nm measured with SMM. The solid line histograms in the data, the dot-dash line shows the nonlinear least squares fit to the data outside the terrestrial absorption feature (Gladstone 1992).

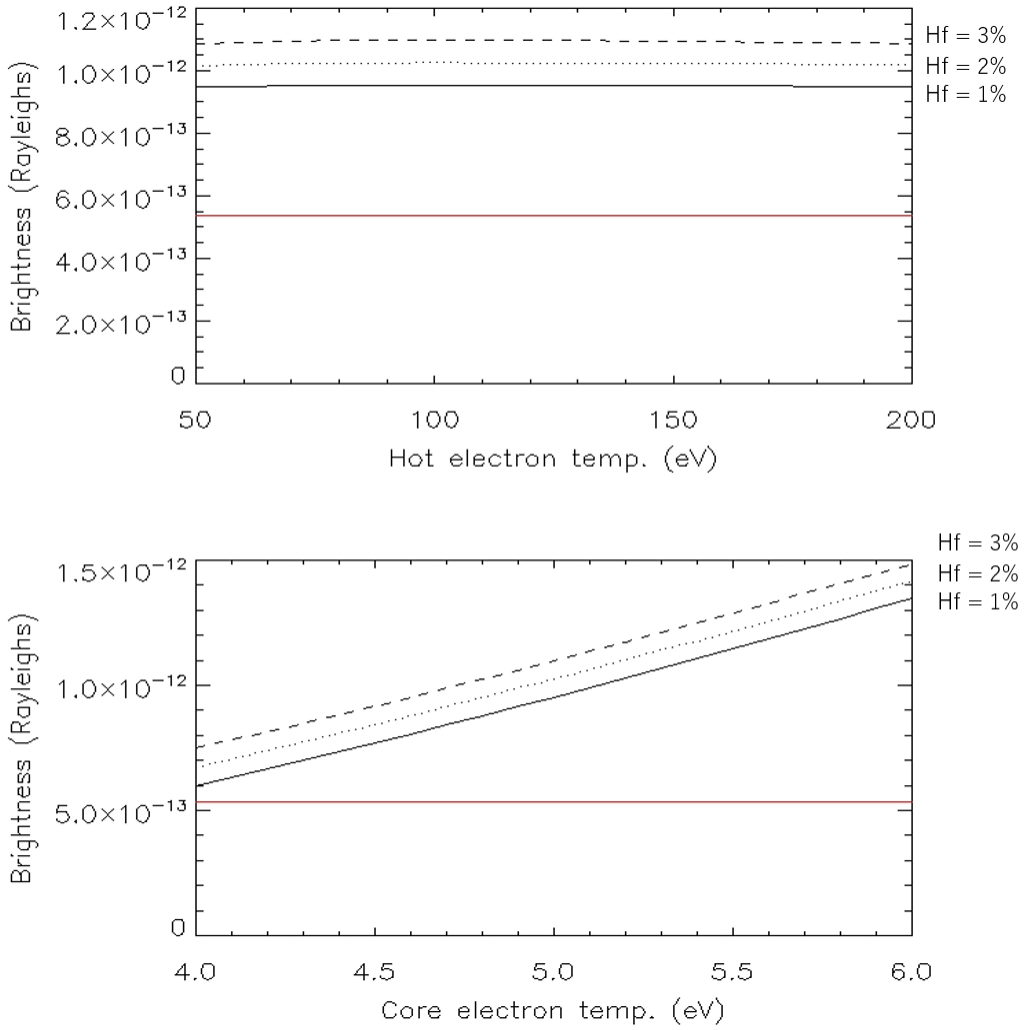

Figure 4.17. (Top) Black lines indicates the relationships between the hot electron temperature and atomic oxygen emission at 130.4 nm per atom due to electron impact excitation for the cases of hot electron fractions (f_H) 1% (solid line), 2% (dot line), and 3 % (dashed line). Core electron temperature is fixed (5 eV). (Bottom) Black lines indicates the relationship between the core electron temperature and atomic oxygen emission at 130.4 nm per atom due to electron impact excitation for the cases of electron fractions 1% (solid line), 2% (dot line), and 3 % (dashed line). Hot electron temperature is fixed (100 eV). Red line indicates atomic oxygen emission at 130.4 nm due to solar resonance scattering.

4.3.3 Discussion

Two possible factors could cause the difference in emission recovery duration (from peak to quiet volcanic activity) between atomic oxygen emission at 130.4 nm and sodium nebula emission observed in season 2. The first factor is time variation of electron density and/or

electron temperature in the Io plasma torus. Sodium emission caused by solar resonant scattering faithfully reflects the sodium column density, while atomic oxygen emission at 130.4 nm is influenced by both electron density and temperature. Temporal and/or spatial increase in electron density or hot electron fraction during the declining period of atomic oxygen emission (at 130.4 nm) could contribute to decrease the declining rate of oxygen emission, but not to decrease that of sodium emission.

The second factor is the difference in the characteristics of source regions of NaCl and SO_2 (Figure 4.11). The sodium nebula consists of fast sodium atoms, which are mainly produced by dissociative recombination of NaCl with an electron ($NaCl^+ + e^- \rightarrow Na + Cl$) (Wilson and Schneider, 1994; Wilson et al., 2002). NaCl is emitted mainly by the hot spot (Moses et al., 2002) because of its extremely high sublimation point (650 K under 1.0×10^{-12} bar (Ewing and Stern, 1974)). Thus, the fact that sodium nebula emission returned to the original level around DOY 90 suggests the end of plume-type volcanic activity. On the other hand, as mentioned in Section 1.1, atomic oxygen is dissociated from SO_2. It is assumed that a large area around volcanic craters is heated by lava lakes (Lopes et al., 2004). SO_2 is emitted from hot spots as well as by evaporation due to lava lakes because its sublimation point is relatively low (113 K under 6.0×10^{-10} bar (Ingersoll, 1989)). Therefore, hot lava lakes may have still have existed after DOY 90 and contributed to the evaporation of SO_2 from the surface.

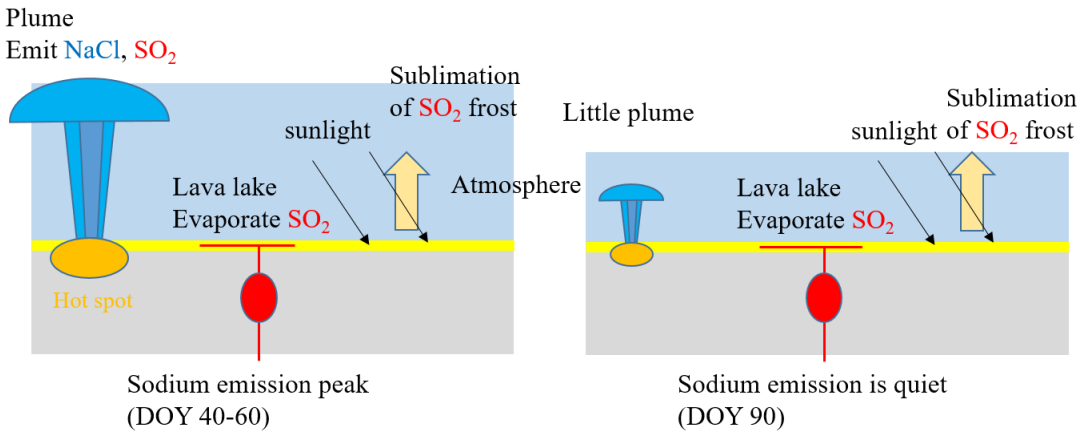

Figure 4.18. Suggestion of Io's atmospheric generation process after the emission peak in 2015.

4.4 Evolution of spatial distribution of the neutral oxygen cloud

4.4.1 Overview of the observation

Figure 4.18 shows the evolution of the spatial distribution of OI 130.4 nm in November 2014 – May 2015. The upper half of the figure is on the dusk side and lower half is on the dawn side. The data between Day of year (DOY) 50.0-53.5 was eliminated because the slit used for this period was not the dumbbell-shaped slit, but a narrower slit of 10 arcsec width (see Yoshioka et al. (2018)). The figure shows that the OI 130.4 nm emission increased from DOY 17 to 108 (called high density period hereafter). We define normal and high density periods as Table 4.1 form the brightness of OI 130.4 nm emissions around Io's orbit. Subsection 4.4.2, we analyze the radial distribution of the OI emission. In subsection 4.4.3, we analyze the azimuthal distribution of OI emission averaged 5-6 R_J on both the dawn and dusk sides, which is binned every 10 days.

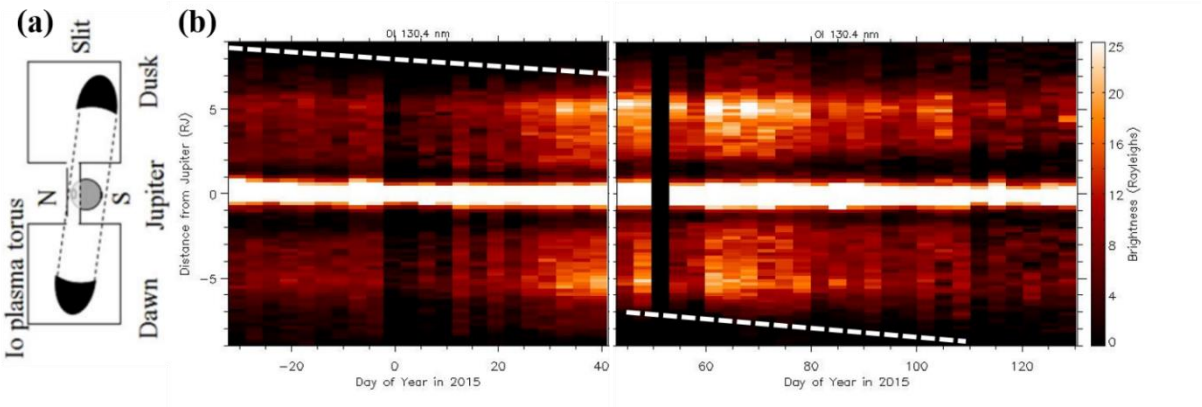

Figure 4.19. (a) Schematic image of the dumbbell-shaped slit during observation (Yoshikawa et al., 2014). (b) Brightness of OI 130.4 nm emissions as a function of time and radial distance from Jupiter in November 2014 – May 2015. White line shows the border of field of view.

Table 4.1. Normal and high density period defined in this section

	Hisaki observation periods	Neutral oxygen density	Major volcanic eruption (de Kleer et al., 2016)
Season 1	Nov. 2013 – Apr. 2014	Normal	Quiet
Season 2	Nov. 2014 – Dec. 2014	Normal	Loki (311°W, 10°N)
	Jan. 2015 – Apr. 2015	High	Kurdalagon (221°W, 49°S)

4.4.2 Evolution of the radial distribution

Figure 4.19 shows the evolution of the radial distribution of OI 130.4 nm. To improve the signal to noise ratio, the data are binned every 10 days. The field of view was limited to the region inside 7-8 R_J from Jupiter before DOY 42 on the dusk side and after DOY 42 on the dawn side (see the white line of Figure 4.18b). We show the radial distribution on the dawn side for DOY -7 in 2015 (DOY 258 in 2014) – DOY 42 in 2015 and that on the dusk side for DOY 43-113 in 2015. We also explained the field of view limitation in subsection 2.1.3. The brightness inside Io's orbit gradually increased from DOY 23 to 73, then decreased from DOY 74 to 103. The emission peak did not move very much (mainly in the range of 5.4-5.6 R_J) for the whole duration. The outer edges of the OI emission were 6.2 R_J in DOY 3-12 and 6.6 R_J in DOY 13-23. We define the outer edge where the brightness of OI emission is comparable with the 1-σ error bars (about 2-4 R). The outer edge moved to around 8 R_J in DOY 23-32. The edge reached the farthest distance of around 8.6 R_J during DOY 64-73 and then returned to 7 R_J afterwards (DOY 84-103).

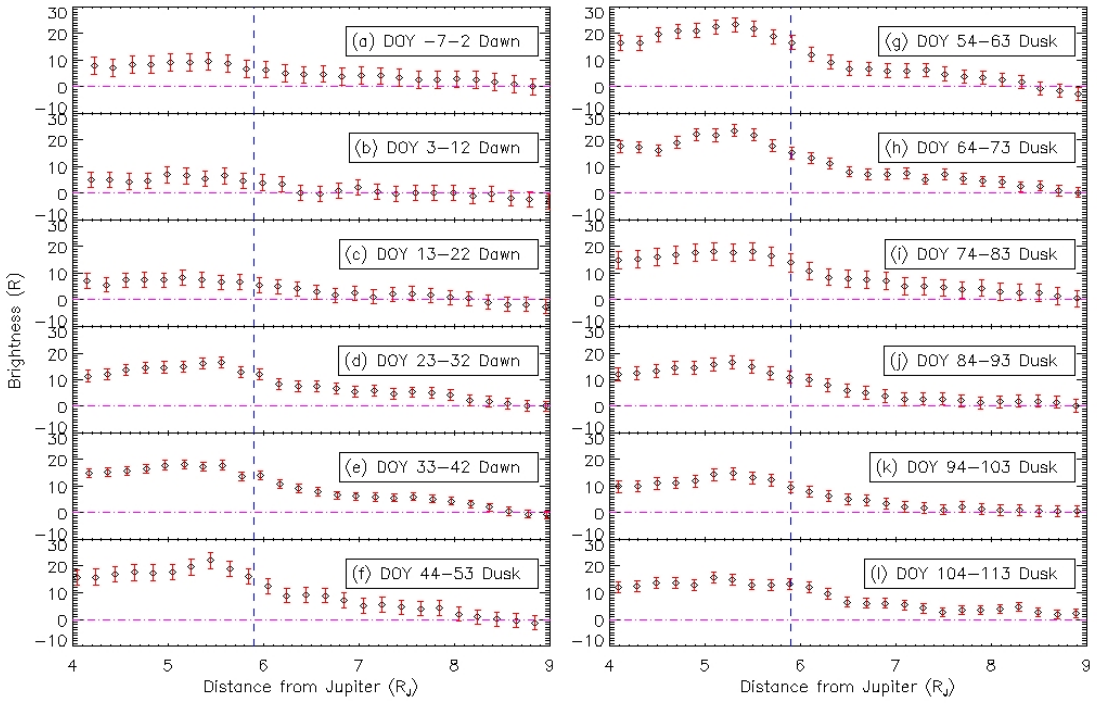

Figure 4.20. Evolution of the radial distribution of OI emission during the volcanic event. The radial distribution shown in the figure is on the dawn side for DOY -7-42, and on the dusk side for DOY 44-113.

Here, we derive the radial distribution of oxygen atom density from the OI emission during the high density period. The electron density (n_e), temperature (T_e), and hot electron density (n_h) outside Io's orbit (5.9 R_J) are derived by Yoshioka et al. (2017, 2018) during the normal (November 2013) and high density periods (February 2015) from IPT observation by Hisaki.

They estimated n_e = 2350±340 cm^{-3}, T_e = 4.5±0.9 eV, n_h = 8.9±7.4 cm^{-3} at 5.91 R_J in November 2013, and n_e = 2860±260 cm^{-3}, T_e = 3.7±0.6 eV, n_h = 21±7.1 cm^{-3} at 5.91 R_J in February 2015. Using electron parameters estimated by Yoshioka et al. (2018) and the CHIANTI atomic database version 8.0 (Del Zanna et al. 2015), we estimated the emissivity for the emission by electron impact (EI) are 8.48×10^{-7} photons/s (normal density period) and 6.86×10^{-7} photons/s (high density period) at Io's orbit. We estimated the emissivity for the emission by solar resonance scattering (RS) is 5.36×10^{-7} photon/s (see subsection 4.2.2). Estimated total emissivities (EI+RS) are 1.39×10^{-6} photons/s (normal density period) and 1.22×10^{-6} photons/s (high density period), the difference between these emissivities being about 10%. Figure 4.20 shows the radial profile of electron density, temperature, and emissivity of OI 130.4 nm in the high density period. We show those in the normal density period in Figure 4.16.

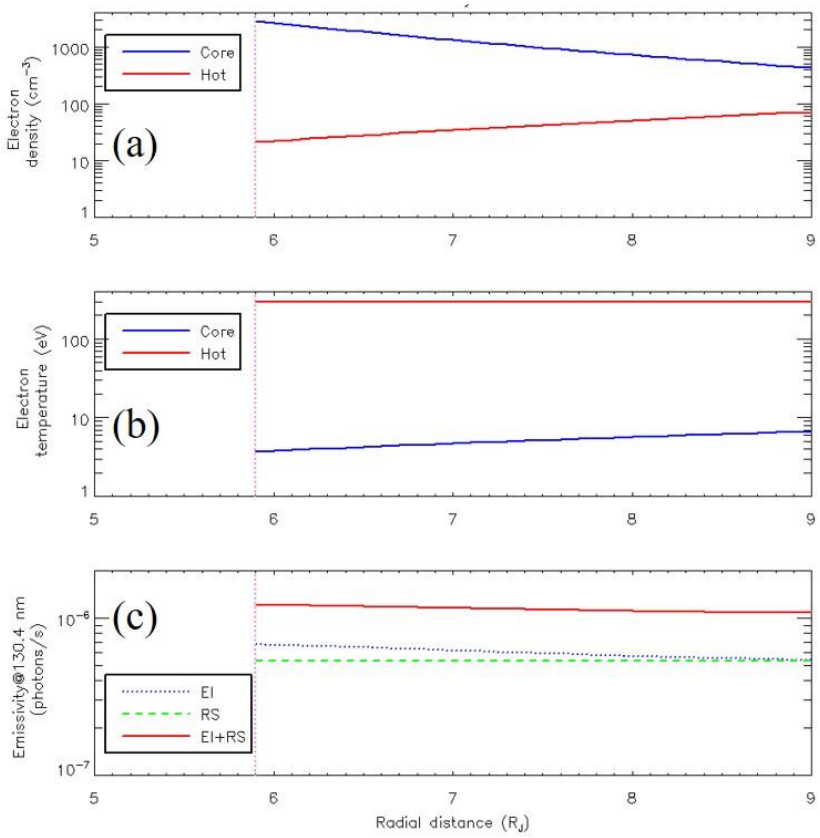

Figure 4.21. (a, b) The radial profile of electron density and temperature in February 2015 (Yoshioka et al., 2018). The vertical dotted line shows the position of Io's orbit (same in later figures). (c) The emissivity of OI 130.4 nm. The blue dotted line (EI) shows the case where only electron impact is considered. The green dashed line (RS) shows the case where only solar resonance scattering is considered. The red solid line (EI+RS) shows the case where both effects are considered.

We estimated the radial profile of atomic oxygen density during the high density period using the emissivity (EI+RS case) shown in Figure 4.20c (red solid line). The period of the data observed by Hisaki (red diamond in Figure 4.21b) was between DOY 44 and 58 in February 2015, partly overlapping with the period of the Hisaki observation which was used for plasma diagnosis by Yoshioka et al. (2018). Because there are no available data of electron density and temperature inside Io's orbit, we only consider the profile outside Io's orbit. We assume that the atomic oxygen number density outside Io's orbit (n) is as follows:

$$\mathrm{n(r)} = \mathrm{n_0}\left(\frac{r}{r_0}\right)^{\gamma}, \tag{4.7}$$

where r_0 is 5.9 R_J (orbit of Io), n_0 is a number density at 5.9 R_J, and γ is a power law slope of the profile. We used the equation (4.5) to calculate the model brightness. The red line in Figure 4.22a shows the radial profile of atomic oxygen density during the high density period. The best-fit parameters are $n_0 = 91^{+29}_{-25}$ cm^{-3} (where the north-south thickness of the cloud is assumed to be 24 arcsec, corresponding to about ±0.6 R_J) and γ = -5.7±1.5 in the high density period. The errors of the number density and power law slope are evaluated by the least squares method (see Press et al. (1992)). We calculated the Chi-square (X^2) from the models and observations of the radial profile outside Io's orbit to estimate values and errors of a number density at 5.9 R_J (n_0) and power law slope (γ).

$$\mathrm{X^2}(n_0, \gamma) = \sum_{i=1}^{N}\left(\frac{x_i - y_i(n_0,\gamma)}{\sigma_i(n_0,\gamma)}\right)^2, \tag{4.8}$$

where x_i is the observation data point, y_i is the model data point, σ_i is the observation error, and N is the number of the data points. Figure 4.23 shows the Chi-square distributions during the normal and high density periods. The errors used in this section are taken from 1-sigma ranges for one parameter.

We refer to the Smyth and Marconi, (2000) model of the OI distribution for the thickness of the cloud. We also estimated the radial profile of atomic oxygen density during the normal density period (black solid line in Figure 4.22a) from the radial profile of OI emission outside Io's orbit on the dusk side in November and December 2014 (Figure 4.22c). We used the emissivity (EI+RS case) in the bottom of Figure 4.16. The densities during the high density period ($n_0 = 91^{+29}_{-25}$ cm^{-3}) are more than three times the values during the low density period ($n_0 = 27^{+8}_{-7}$ cm^{-3}). The power law slope during the high density period (γ = -5.7±1.5) is larger than that during the low density period (γ = -3.6±1.2).

Delamere et al. (2004) estimated atomic oxygen number densities change from 30 to 120 cm^{-3} during the Cassini eruptive event at the end of 2000. The atomic oxygen densities at Io's orbit estimated from Hisaki observations during both high and low density periods are

almost within the range of the Delamere et al. (2004) result. Delamere et al. (2005) showed profiles of the latitudinally integrated O column density, which are consistent to Cassini observation results. According to Delamere et al. (2005) (Figure 4.24), the column density at 6.0 R_J is ~7.3×10^{11} cm^{-2} and the power law slope within 6-8 R_J is ~-8.5 (larger slope case), and the density is 8.2×10^{11} cm^{-2} and the slope is ~-15.9 (smaller slope case). The column density during the high density period at 6.0 R_J estimated in this study is ~7.1×10^{11} cm^{-2} (82.7 cm^{-3} × 1.2 R_J), similar to the result of Delamere et al. (2005). However, the power law slopes during normal and high density periods are much larger than their results. Hisaki observation shows densities of O during both periods decrease with the increase of radial distance more gradual than previous studies.

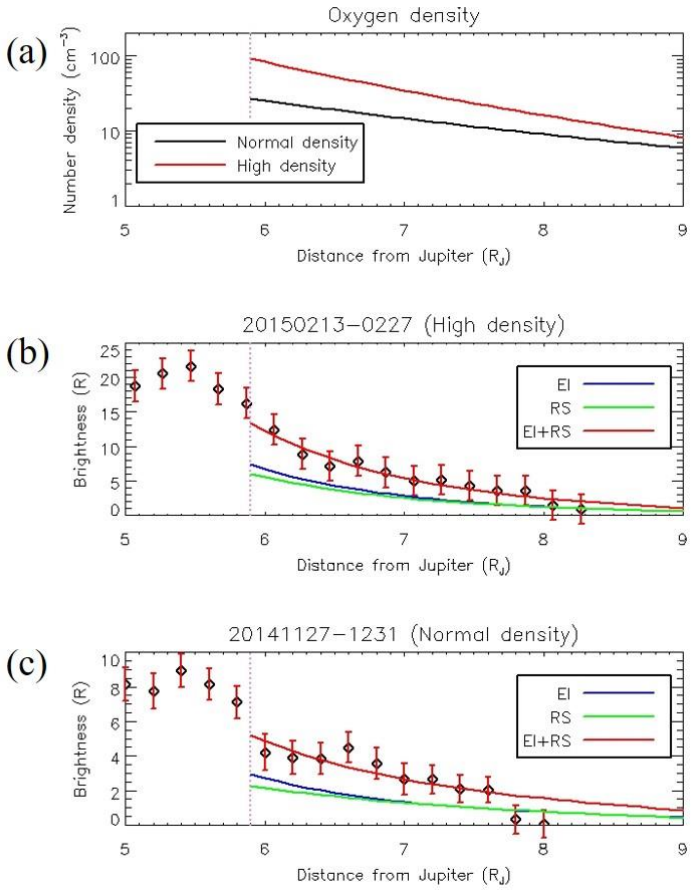

Figure 4.22 (a) The radial profile of atomic oxygen number density during the normal density period in November and December 2014 (black line) and that during the high density period in February 2015 (red line). (b) The radial profile of OI 130.4 nm during the high density period observed by Hisaki (black diamonds with red error bars). EI (blue) and RS (green) show contributions of electron impact excitation (EI) and solar resonance scattering (RS), respectively. The red solid line (EI + RS) shows the model brightness when the density profile given by the red line in the top panel is applied. (c) The radial profile of OI during the normal density period. The profiles during both the periods are on the dusk side.

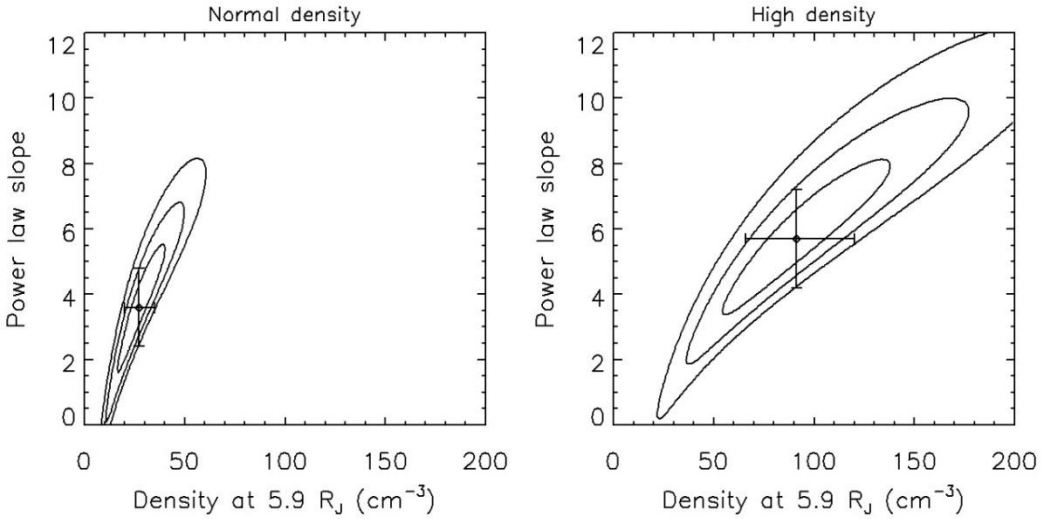

Figure 4.23. Plots of Chi-square for two parameters (the density at 5.9 R_J and the power law slope) during the normal (left) and high density periods (right). The diamond mark is where the value of Chi-square is minimum ($\Delta X^2 = 0$). Ellipsoidal lines correspond to 1-sigma, 2-sigma, and 3-sigma ($\Delta X^2 = 2.3, 6.17, 11.8$). The 1-sigma ranges for the single parameter fit are over-plotted as a cross marking $\Delta X^2 = 1.0$.

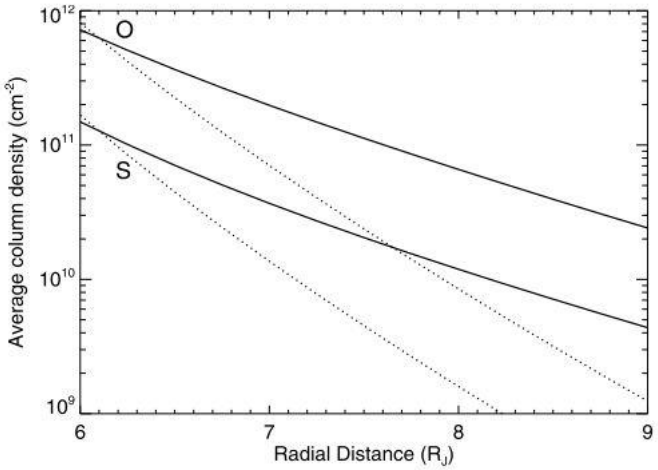

Figure 4.24. Modeled column density profile of neutral oxygen and sulfur clouds as a function of radial distance (Delamere et al., 2005).

4.4.3 Evolution of the azimuthal distribution

Figures 4.25 and 4.26 show the evolution of Io phase angle (IPA) dependence of OI emission brightness in the range of 5-6 R_J on the dusk and dawn sides. We averaged the brightness every 30 degrees of IPA. In section 4.3, we showed the equilibrium neutral oxygen cloud consists of a dense region distributed around Io (the "banana cloud") and a longitudinally uniform, diffuse region distributed along Io's orbit. In Figure 4.24, the emission in IPA 0-180° consists of the diffuse region. The emission around IPA 240-300° consists of both contributions but the banana cloud dominates. In Figure 4.25, the emission on the dawn side shows the same behavior as the dusk side.

To evaluate changes of the banana cloud and the diffuse region during the volcanic event, we fit a Gaussian to the azimuthal structure of the OI emission (solid lines in Figures 4.25 and 4.26) and illustrate the variations in the fitting parameters. The Gaussian function we used is as follows:

$$f = A_4 + A_1 exp\left[-\frac{(x - A_2)^2}{2A_3^2}\right], \tag{4.9}$$

where x is the Io phase angle. Figure 4.27 shows the variations of Gaussian parameters (A_1-A_4) during DOY -7 to 113 in 2015. The parameters A_1, A_2, A_3, and A_4 correspond to the peak brightness of the banana cloud, the IPA at the emission peak, the width of the banana cloud, and the average brightness of the diffuse region. In the case of the dusk side (left figure), the peak brightness (A_1) and the brightness of the diffuse region (A_4) during DOY 23-42 were higher than those before DOY 22. It shows that the densities of the banana cloud and the diffuse region increased in the same period. We found the maximum value of the emission peak (A_1) was in the period DOY 44-53, while the diffuse region (A_4) peaked in the period DOY 64-73. The period when the diffusion region peaked matches the time when the outer edge of OI emission reached the farthest distance (8.6 R_J, see Figure 4.20). We consider the possibility that the diffuse region spread outward from Jupiter in this period. The width (A_3) was high during DOY -7 to 2, decreased during DOY 3-22, and then started to increase after DOY 23. However, it was not significant trend enough to show the variations of the width of the banana cloud. Only the peak IPA (A_2) slightly decreased after DOY 13 and returned to the initial level during DOY 54-83, but the variation was minimal compared to the uncertainties. In the case of the dawn side (right figure), we cannot find an increase in the width (A_3) after DOY 3. The brightness of the banana cloud and the diffuse region (A_1 and A_4) increased during DOY 3-42. The brightness of the diffuse region decreased in the period DOY 44-53 and increased during DOY 54-73 again.

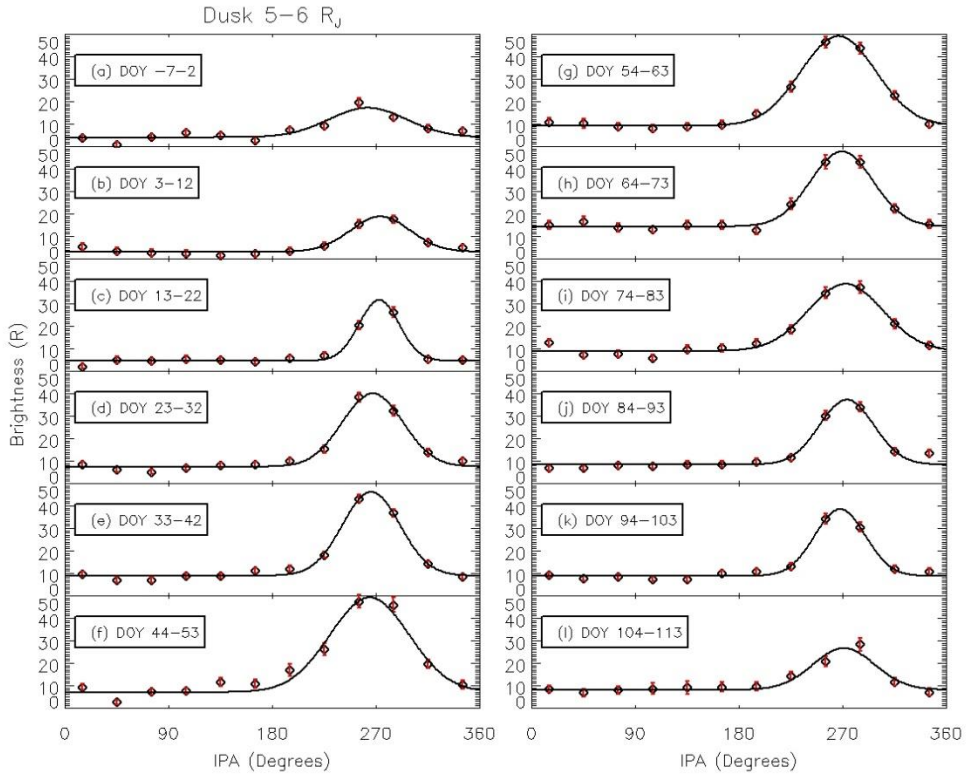

Figure 4.25. Io phase angle (IPA) dependence of OI emission brightness in the range of 5-6 R_J on the dusk side with a Gaussian fit line (solid line). Each column shows 10-day average distributions, and each point shows an IPA 30-degree average brightness.

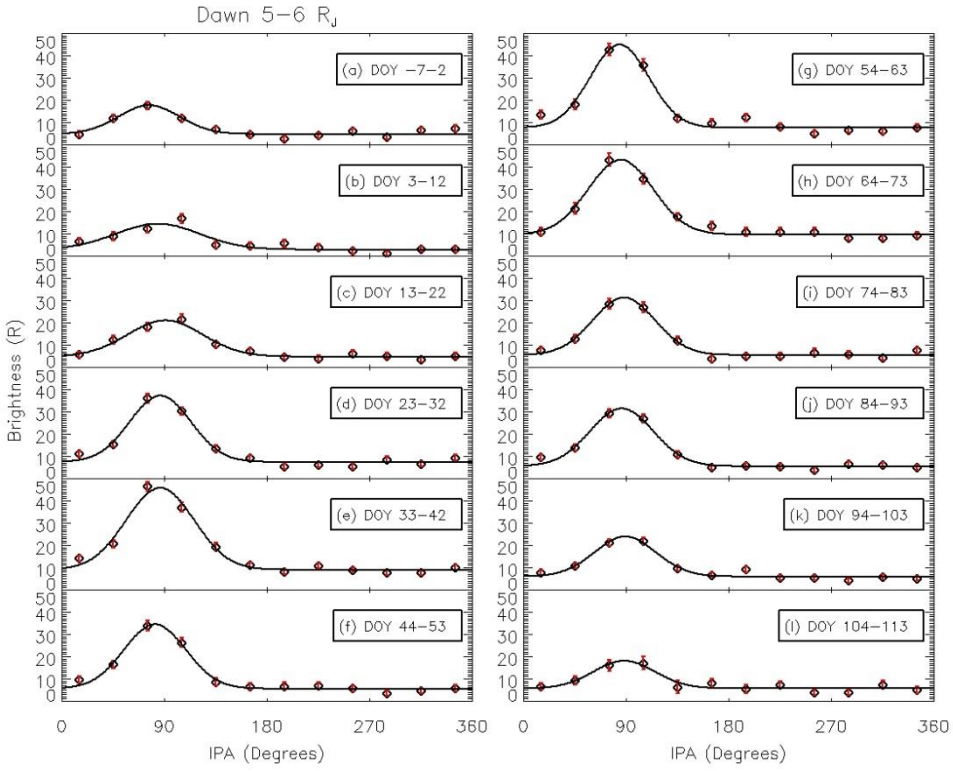

Figure 4.26. IPA dependence of OI emission brightness in the range of 5-6 R_J on the dawn side.

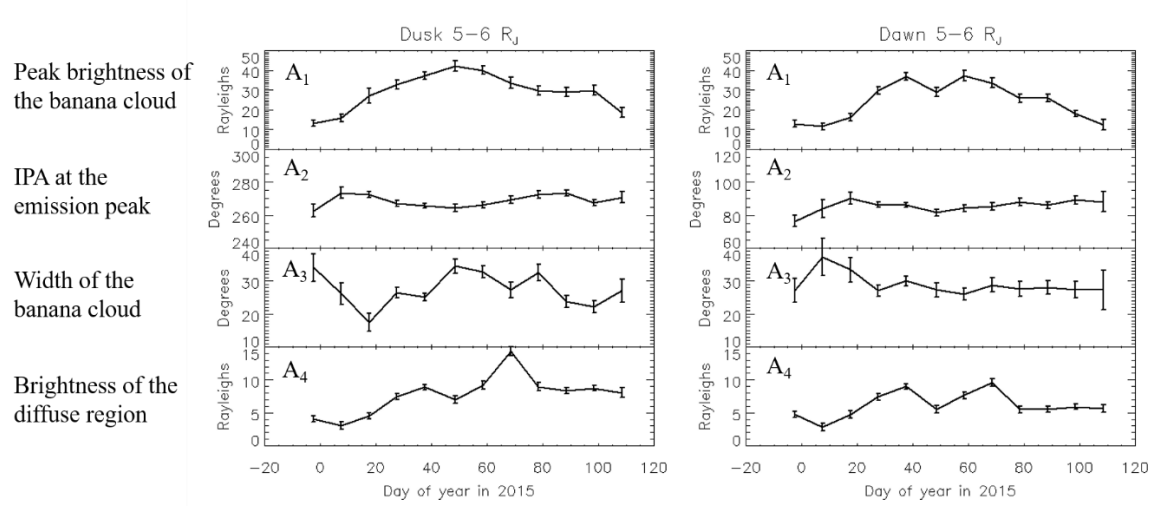

Figure 4.27. Time variations of Gaussian fit parameter on the dawn (right) and dusk sides (left) (see text).

4.4.4 Discussion

We discuss the origin of increases in the brightness and expansion of Io's neutral oxygen cloud. Smyth and Combi (1988, 1997) showed the velocity distribution of neutrals ejected from Io, which represents the composite effects of atmospheric heating below the exobase and atmospheric sputtering. The distribution has a core component that has a peak at 0.5 km/s (well below the exobase escape velocity of ~2 km/s) and a tail component that extends to many 10s of km/s (Smyth and Marconi, 2003). The model of Smyth and Combi (1997) showed sodium column densities outside of the corona (6-100 Io radii from Io) increase with decreasing the slope of the velocity distribution over the peak (see Figure 4.28). The parameter α related to the slope is explained in section 1.3.2. According to Smyth and Combi (1997) and Smyth and Marconi (2003), the slope relates to the degree of completion of the cascade process after ions collide with atmospheric atoms. It is because the collisional cascade moves energy from the higher velocity component to the lower velocity one around the peak of the velocity distribution.

We speculate that the increase of the source rate caused the first increase in the banana cloud density (A_4) during DOY 13-42. If both the core and tail velocity components increased, both A_1 and A_4 increased and the edge of the cloud moved outward (from ~6.4 to ~8 R_J) in this period. We also speculate that the decrease in the slope of the tail component caused the second increase of A_4 during DOY 44-73. If the tail velocity component (several 10s of km/s) increased but the lower velocity component (near the exobase escape velocity) decreased, A_1 decreased, but A_4 increased, and the edge of the cloud spread outward (from ~8 to ~8.6 R_J) in this period. If this hypothesis is true, the average number of the collisional cascade decreased in this period. The changes in ion temperature in IPT and/or the distribution of Io's upper atmosphere could cause the change of the velocity distribution of the neutrals ejected from Io's atmosphere.

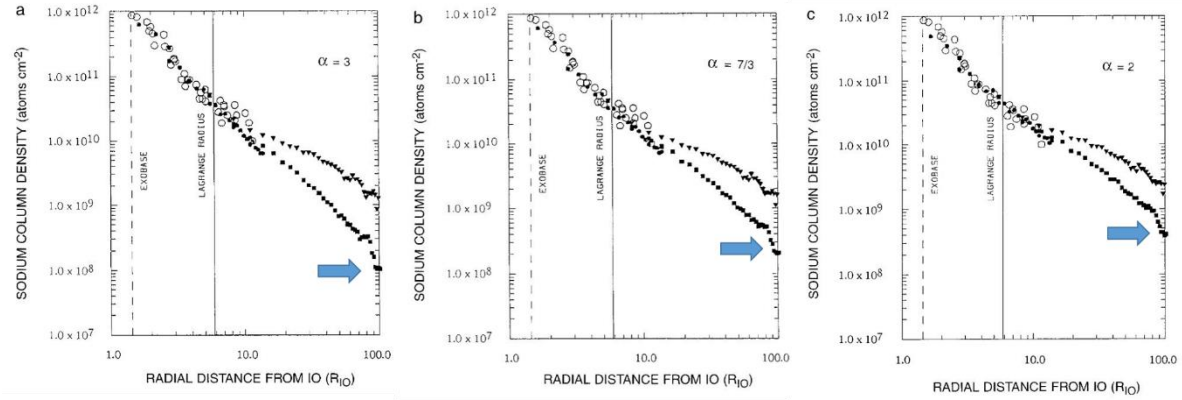

Figure 4.28. Model calculation using cascade velocity distribution in three slope cases (Smyth and Combi, 1997). Open circle shows observations of the sodium cloud and corona (Schneider et al., 1991). Triangle shows model for the leading cloud along the east-west direction. Square shows model for the trailing cloud.

4.5 Summary

We studied the distribution and variation of neutral oxygen cloud in the torus using Hisaki satellite. The major points we found in this chapter as follows:

1. Io's oxygen cloud consists of two regions, namely, a dense region (banana cloud) near Io and a diffuse region with a longitudinally homogeneous distribution along Io's orbit. The banana cloud spreads along the leading side of Io and inside of Io's orbit. The neutral oxygen cloud spreads out to 7.6 Jupiter radii (R_J), where the brightness drops below ~1 R (corresponding to 1-sigma error).
2. We revealed that atomic oxygen emission increased by a factor of 2.5 in 2015 when Io volcanism was active. The period for atomic oxygen brightness to increase from the volcanically quiet levels to the maximum levels and that of sodium were almost same (30 days).
3. On the other hand, the duration of atomic oxygen brightness recovery from maximum levels to the quiet levels (before the volcanic event) was 60 days and longer than that of the sodium nebula of about 40 days. Time variation of electron densities and/or electron temperatures in Io's plasma torus after the volcanic eruption and the difference between source regions of NaCl and SO_2 may be possible mechanisms to explain the difference in the rates of decrease in brightness.
4. Io's oxygen cloud consists of two regions, namely, a dense region (banana cloud) near Io and a diffuse region with a longitudinally homogeneous distribution along Io's orbit. The banana cloud spreads along the leading side of Io and inside of Io's orbit. The neutral

oxygen cloud spreads out to 7.6 Jupiter radii (R_J), where the brightness drops below ~1 R (corresponding to 1-sigma error).

5. The evolution of the radial distribution of OI shows Io's neutral oxygen cloud spread outward during the high density period (from 7 R_J to a maximum of 8.6 R_J). The estimated densities during the high density period are 91^{+29}_{-25} cm^{-3} at 5.9 R_J, more than three times as large as those during the normal density period (27^{+8}_{-7} cm^{-3} at 5.9 R_J).
6. We found a series of expansions of Io's neutral oxygen cloud from the evolution of the azimuthal distribution of OI. The both densities of the banana cloud the diffuse region increased during the high density period.

The above results help to better constrain the neutral oxygen torus geometric distribution as a function of time. For follow-on research, we will apply these new features to constrain the neutral Io torus model (e.g., Smith et al., 2019). Combining the observational results with a physical model, we are able to place much better constraints on Io source processes and their characterization.

Chapter 5 Source and loss processes of Io plasma torus

OI 130.4 nm emission in Io torus reflects not only escape process from Io's atmosphere, but also electron temperature and density (electron impact excitation), and ionization process of oxygen atom. In this chapter, we describe the dawn-dusk asymmetry of electron temperature in section 5.1, the change of lifetime of O^+ during a volcanic event in section 5.3, and estimated oxygen plasma source rate in the torus in section 5.2 using the atomic oxygen and IPT data obtained by Hisaki/EXCEED.

5.1 Dawn-dusk asymmetry of OI

As mentioned in section 4.2, the atomic oxygen emission at 130.4 nm when Io was on the dusk side was generally larger than that when Io was on the dawn side throughout the observation periods in 2013-2015. We summarize the dusk to dawn ratio of observed emissions of O, S and Na in the wavelength range from UV to visible in Table 5.1. Doppler shift due to Io's orbital motion does not account for the difference between brightness of the atomic oxygen emission on the dawn side and those on the dusk side with regard to resonant scattering of solar irradiance as described in Subsection 4.2.2. Sodium nebula emissions at D-lines (588.9 and 589.5 nm) did not show the dawn-dusk asymmetry (Yoneda et al., 2015). In contrast, atomic oxygen emission at 630.0 nm from Io's atmosphere and corona, which are probably caused by electron impact excitation (Oliversen et al., 2001), indicated a dawn-dusk asymmetry (Scherb and Smyth, 1993). The dawn-dusk asymmetry was also seen in the other lines of SI and OI, which are excited by electron impact (Ballester 1989).

The possible causes of the dawn-dusk asymmetry due to electron impact excitation are examined as follows. Plasma parameters are derived as a function of Jupiter's radius from EUV spectra observed by Cassini (Steffl et al., 2004), and by the Hisaki satellite. In this section,

we use results of Hisaki observation on 29 November 2013. Yoshioka et al. (2014) showed that the core electron temperature for 5.9-7.6 R_J on the dusk side (5.5 eV) is larger than on the dawn side (4.6 eV) (see Figure 5.2). This dawn-dusk asymmetry in electron temperature may be caused by the dawn-to-dusk electric field in the Jovian magnetosphere (Barbosa and Kivelson, 1983; Ip and Goertz, 1983). It was also suggested that hot electron fraction and core electron density are 2.6 % and 1400 cm^{-3} on the dawn side and 1.5 % and 1300 cm^{-3} on the dusk side, respectively (Yoshioka et al., 2014). Based on plasma parameter derived by Yoshioka et al. (2014) and the CHIANTI atomic database, the ratio of atomic oxygen emission at 130.4 nm on the dusk side to that on the dawn side is estimated as 1.10.

Time variation of atomic oxygen brightness ratio (brightness on the dusk side relative to that on the dawn side) averaged for 10 days in season 1 (from 19 December 2013 to 24 April 2014) and season 2 (from 27 November 2014 to 14 May 2015) is plotted in Figure 5.3. The plot indicates that the brightness on average on the dusk side was larger than that on the dawn side by a factor of 1.12±0.03 during season 1, and 1.21±0.03 in season 2 (error bars show the standard errors ($1\sigma/\sqrt{n}$; n are the data numbers) of the data). Averaged dawn-to-dusk ratio of atomic oxygen emission at 130.4 nm in seasons 1 was consistent with the estimation shown in the above paragraph based on plasma parameters derived by Yoshioka et al., (2014). This result indicates that the dawn-dusk asymmetry of atomic oxygen emission at 130.4 nm is due to the dawn-dusk asymmetry of core-electron temperature. The averaged ratio is larger than the estimation. Hikida et al. (2019) shows the electron densities at 5.9 R_J on the dusk side are larger than those on the dawn side from DOY 330 in 2014 to 45 and from 80 to 120 in 2015. They also showed the hot electron fractions increased only on the dusk side from DOY 50 in 2015. We considered the increase of hot electron density on the dusk side relates to the increase of the dawn-to-dusk ratios of OI 130.4 nm emission after DOY 50 in 2015.

Table 5.1. Summary of observed dawn to dusk brightness ratios of Iogenic neutral species emission. EI is electron impact excitation, and RS is solar resonance scattering.

Species	Emission line (nm)	Main mechanism	Dusk/dawn ratio	Reference
Na	588.9, 589.5	RS	0.99	Yoneda et al., 2015
S	147.9	EI	~1.7	Ballester 1989
	181.4	EI	~1.5	Ballester 1989
	190.0, 191.4	EI	~1.3	Ballester 1989
O	135.6	EI	~1.4	Ballester 1989
	630.0	EI	~1.5	Scherb and Smyth., 1993
	130.4	EI+RS	1.12±0.03 (season 1) 1.21±0.03 (season 2)	This study

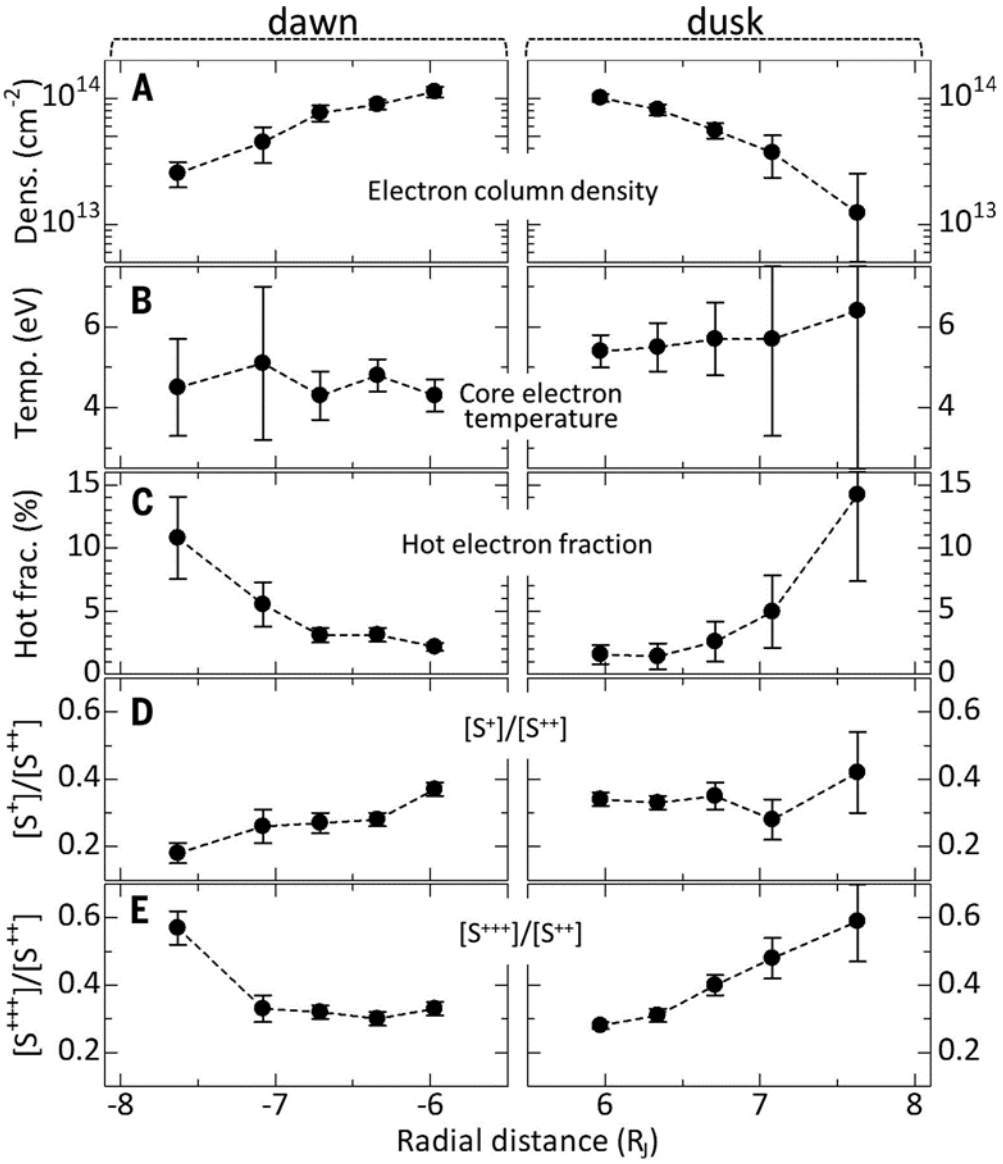

Figure 5.1. Plasma parameter derived from the spectral diagnosis as a function of radial distance from Jupiter on dawn side and dusk side (Yoshioka et al., 2014). Core electron temperature on the dawn side was larger than on the dusk side. The tendency did not depend on radial distance from Io.

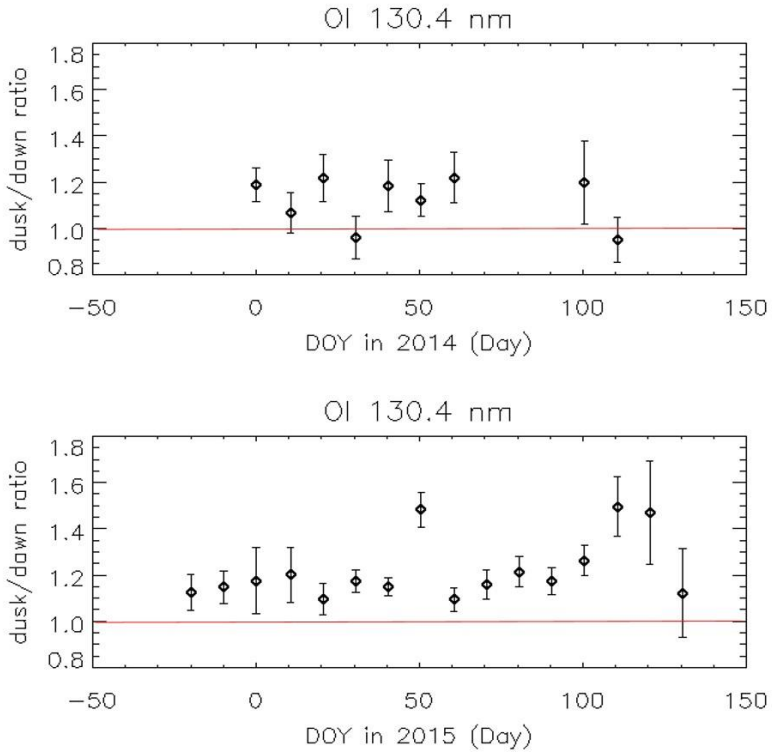

Figure 5.2. Variations of the atomic oxygen at 130.4 nm brightness ratio on the dusk side to on the dawn side for the cases of season 1 and season 2. Each data point is a value averaged for 10 days.

5.2 Oxygen ion source rate

We estimated the total oxygen ion source rate by using the radial profile of oxygen density estimated in Subsection 4.3.3. Oxygen atoms in the neutral cloud are ionized by electron impact and charge exchange. We calculated the oxygen source rate caused by electron impact (S_{EI}) by inputting the electron parameters from the top and middle panels of Figure 4.16 into the equations shown below (see review by Schreier et al., 1998):

$$S_{EI} = (I_O n_{e,core} + I_O^h n_{e,hot}) n_O,$$
$$I_O = 1.1015 \times 10^{-8} \sqrt{T_{e,core}} exp\left(-\frac{14.54}{T_{e,core}}\right), \quad (5.1)$$
$$I_O^h = 5.747 \times 10^{-7} \frac{\ln(T_{e,hot}/27.07)}{\sqrt{T_{e,hot}}},$$

where $n_{e,core}$ is the core electron density, $T_{e,core}$ is the core electron temperature, $n_{e,hot}$ is the hot electron density, $T_{e,hot}$ is the hot electron temperature, and n_0 is the atomic oxygen number density.

We then calculated the oxygen source rate caused by charge exchange (S_{CE}) by using the ion density profile and reaction coefficients as follows. Top and middle panels of Figure 5.3 show the radial profiles of sulfur and oxygen ions and that of oxygen atoms. We used O^+, O^{2+}, S^+, S^{2+}, S^{3+} densities derived by Bagenal (1994) inside of Io's orbit, and those of Yoshioka et al. (2017) outside of Io's orbit. The black line shows the atomic oxygen profile estimated in this study (see Subsection 4.2.3). Table 5.3 shows a list of charge exchange reactions and reaction coefficients (Delamere et al., 2005). The charge exchange source, S_{CE} can be written as

$$S_{CE} = (k_1 n_{O+} + (k_2 + k_3) n_{O2+} + k_4 n_{S+} + k_5 n_{S2+} + k_6 n_{S3+}) n_O. \quad (5.2)$$

The bottom panel of Figure 5.3 shows the radial profile of the oxygen plasma source rate ($cm^{-3}s^{-1}$). The red line shows the source rate of electron impact ionization, the blue line shows the charge exchange rate, and the black line shows the total source rate ($S = S_{EI} + S_{CE}$). The figure shows that the source rate of charge exchange is larger than that of electron impact from 4 to 7.3 R_J, and the rate of charge exchange is smaller than electron impact beyond 7.4 R_J. This switch from charge-exchange to electron-impact-ionization at ~7.5 R_J is consistent with models of Smyth and Marconi (2003) and Delamere et al. (2005) (see Figure 5.4).

The equation that estimates the total oxygen source rate in the neutral cloud (S_{NC}, kg/s) is

$$S_{NC} = m_O \int_{5\ R_J}^{9\ R_J} 2\pi x h \cdot S(x) dx\,, \quad (5.3)$$

where *x* is the radial distance centering Jupiter, h is the north–south thickness of the cloud (1.2 R_J), and m_O is the mass of an oxygen atom (2.66×10^{-26} kg).

In this study, we assumed that the neutral oxygen cloud is uniform in the north–south direction and that the radial range where oxygen atoms are ionized is between 5-9 R_J. Finally, we calculated the total source rate to be 410 kg/s where 100 kg/s was caused by electron impact ionization and 310 kg/s was caused by charge exchange. Yoshioka et al. (2017) estimated the oxygen and sulfur ion source rates which are necessary to explain the ion densities derived from Hisaki observations in November 2013. They found best-fit oxygen and sulfur source rates to be 4.0×10^{-4} $cm^{-3}s^{-1}$ and 3.7×10^{-4} $cm^{-3}s^{-1}$, and the total neutral source rate is 1.3 t/s. This means their oxygen source rate was calculated to be 460 kg/s. Thus, the total oxygen source rate estimated in this study is consistent with the results of Yoshioka et al. (2017).

Before the Hisaki observations, the total source rate and O/S ratio were also derived from Voyager 1 and 2 and Cassini observations (Bagenal & Delamere, 2011; Delamere & Bagenal, 2003; Delamere et al., 2004). The oxygen source rates shown in the above references are summarized in Table 5.3. The oxygen source rate estimated in this study is in the range of the value based on the Cassini observations in January 2001 (310 kg/s) and that based on Voyager 1 observations in March 1979 (530 kg/s). The results based on the Voyager 2 observations in July 1979 (1,730 kg/s) and Cassini observations in September 2000 (1,460 kg/s) are much larger than the value obtained in this study and are known to be times of high volcanic activity at Io and high plasma production (Delamere et al., 2004).

Table 5.2. List of reactions for ionized oxygen atoms in the neutral cloud and reaction coefficients (Delamere and Bagenal, 2003).

Reaction	Coefficients (k, cm^3s^{-1})
$O + O^+ \rightarrow O^+ + O$	$k_1 = 1.32 \times 10^{-8}$
$O + O^{2+} \rightarrow O^+ + O^+$	$k_2 = 5.2 \times 10^{-10}$
$O + O^{2+} \rightarrow O^{2+} + O$	$k_3 = 5.4 \times 10^{-9}$
$O + S^+ \rightarrow O^+ + S$	$k_4 = 6.0 \times 10^{-11}$
$O + S^{2+} \rightarrow O^+ + S^+$	$k_5 = 2.3 \times 10^{-9}$
$O + S^{3+} \rightarrow O^+ + S^{2+}$	$k_6 = 1.92 \times 10^{-8}$

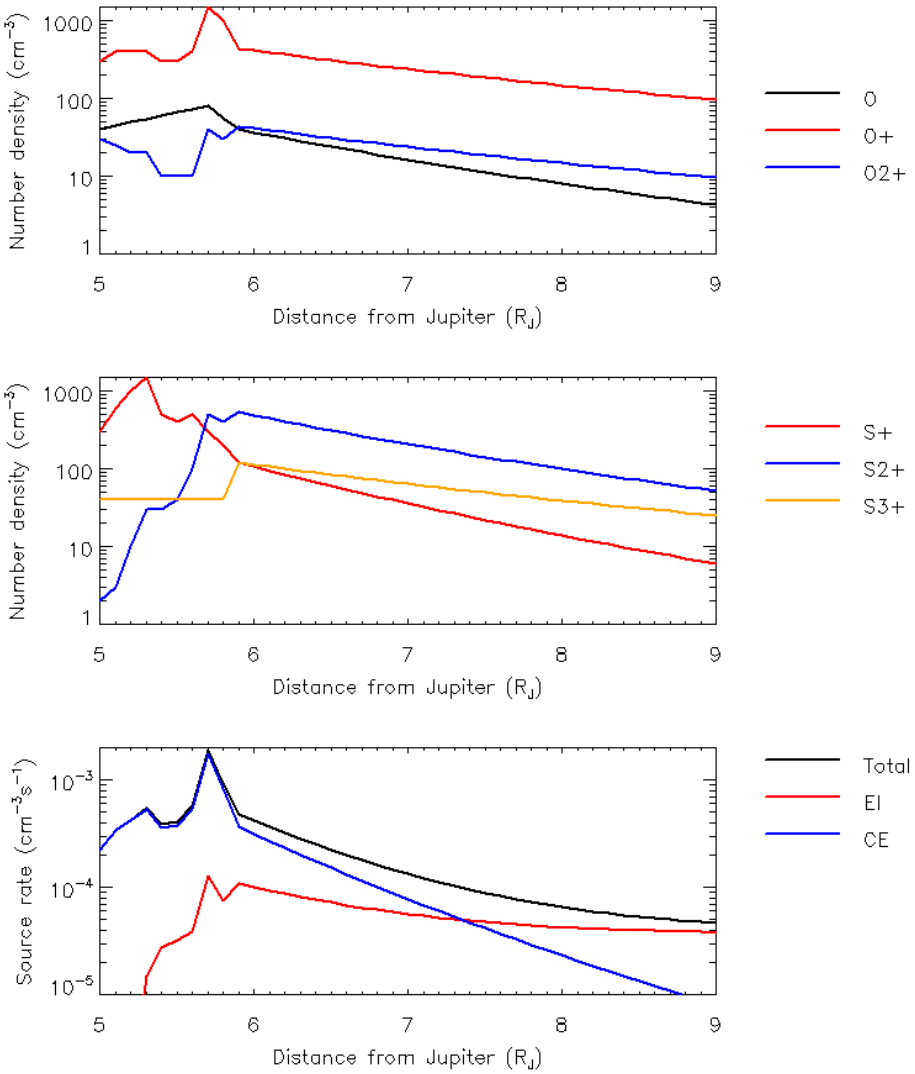

Figure 5.3. (Top and middle) Radial profiles of the number densities of oxygen and sulfur ions. The profiles inside Io's orbit are from Bagenal (1994), and those outside Io's orbit are from Yoshioka et al. (2017). The radial profile of oxygen atoms derived in this study is also shown in the black line. (Bottom) Radial profile of the oxygen source rate calculated in this study. EI, CE show contributions of electron impact (EI) and charge exchange (CE), respectively.

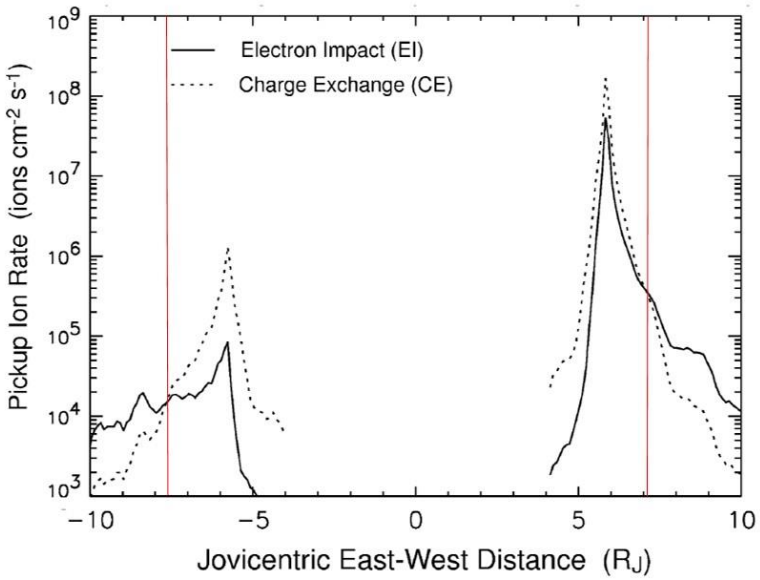

Figure 5.4. Radial profile of pick-up ion rate of oxygen (Smyth and Marconi, 2003). Red vertical lines show switches from electron impact (EI) to charge exchange (CE) at about ~7.5 R_J.

Table 5.3. List of the total neutral source rate, O/S ratio, and oxygen source rate in the neutral cloud estimated by previous studies (Bagenal & Delamere, 2011; Delamere & Bagenal, 2003; Delamere et al., 2004; Yoshioka et al., 2017).

	Voyager 1 Mar 1979	Voyager 2 Jul 1979	Cassini Sep 2000	Cassini Jan 2001	Hisaki Nov 2013
Total source rate (kg s^{-1})	800	2600	3000	640	1300
O/S ratio	4	4	1.9	1.9	1.08
Oxygen source rate (kg s^{-1})	530	1730	1460	310	460

5.3 Estimating the O^+ lifetime

5.3.1 Hisaki observation results

We estimate lifetimes of O^+ in the torus for the two cases during high torus density period and normal density period. Figure 5.5a and 5.5b show time variations of OI 130.4 nm and OII 83.4 nm emissions, respectively, averaged over the range of 5-6 R_J on both dawn and dusk sides.

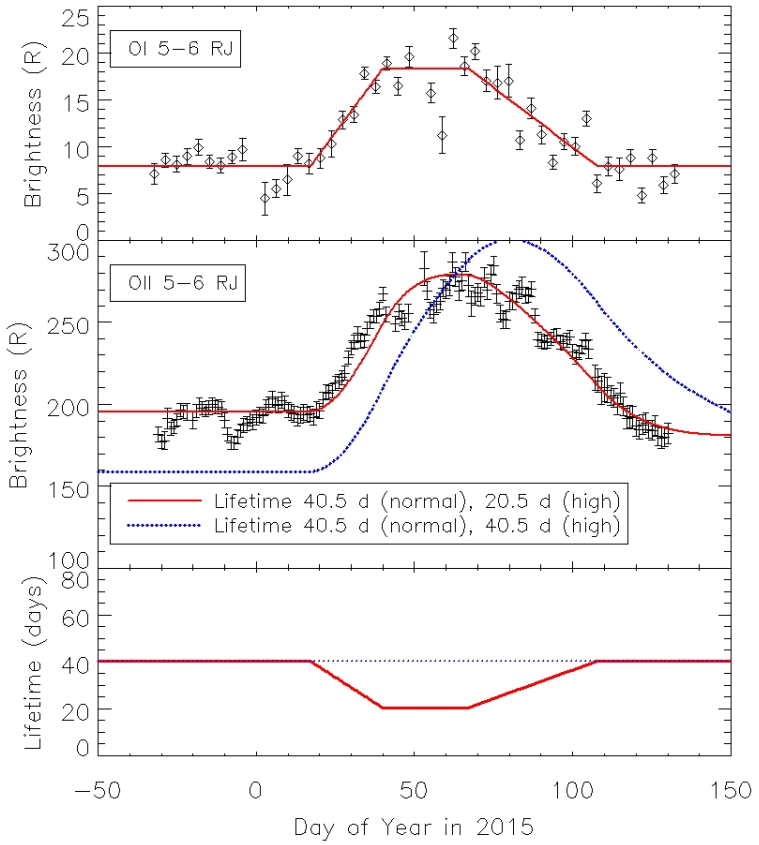

Figure 5.5. (a) Time variations of OI 130.4 nm emission averaged from 5 to 6 R_J from Jupiter on the dawn and dusk sides. Red line shows fitted line (see text). (b) Time variations of OII 83.4 nm emission averaged from 5 to 6 R_J on the dawn and dusk sides. The red solid line shows best-fit line for the case of the O^+ lifetimes of τ_{low} = 40.5 and τ_{high} = 20.5 days, and the blue dashed line shows the constant lifetime of 40.5 days. (c) Time variations of the lifetime assumed in Figure 5.5b. The solid red line is in the case of τ_{low} = 40.5 and τ_{high} = 20.5 days, and blue dashed line is in the case of the constant lifetime of 40.5 days.

We assume that the time variation of OI 130.4 nm emission brightness, $I_O(t)$, is modeled as a trapezoidal shape as follows (as indicated by the red line in Figure 5.5a):

$$\mathrm{I_O}(t) = \begin{cases} y_0 & (t < t_1, t_4 \le t) \\ \{s_1(t-t_1)+1\}y_0 & (t_1 \le t < t_2) \\ ay_0 & (t_2 \le t < t_3) \\ \{s_2(t-t_3)+a\}y_0 & (t_3 \le t < t_4) \end{cases}, \tag{5.4}$$

where

$$\mathrm{s_1} = \frac{a-1}{t_2-t_1}, s_2 = -\frac{a-1}{t_4-t_3}, \tag{5.5}$$

where t is DOY in 2015, y_0 is the brightness during the normal density period (Rayleighs (R)), a is a gain of the OI brightness during the peak to the normal density period (a > 1), and t_1 - t_4 are DOY of the inflection points' coordinates. The best-fit parameters are y_0 = 7.9 R, a = 2.3, t_1 = 17, t_2 = 40, t_3 = 67 and t_4 = 108. We assume that the source rate of O^+, $f_{O^+}(t)$, is proportional to $I_O(t)$.

$$f_{O^+}(t) = \alpha I_O(t), \tag{5.6}$$

where α is a constant. We assume that the variations of the O lifetime does not influence the relation between $f_{O^+}(t)$ and $I_O(t)$. Another assumption is that the lifetime of O^+ depends on the source rate of O^+. Delamere et al. (2004) found that the transport time scale decreased significantly when the source rate increased. The lifetime of O^+ can thus also be assumed to be represented by a trapezoidal function as in Equation (5.4) with $\mathrm{y_o} = \tau_{\mathrm{low}}$ (lifetime of O^+ during the normal density period) and $\mathrm{ay_O} = \tau_{\mathrm{high}}$ (lifetime of O^+ during the high density period) (figure 5.5c). We set the model density of O^+, $N_{O^+}(t)$, as a function of t as follows (Yoneda et al., 2010):

$$N_{O^+}(t) = \int_{-\infty}^{t} f_{O^+}(t') exp\left(-\frac{t-t'}{\tau_{O^+}(t')}\right) dt', \tag{5.7}$$

where τ_{O^+} is the lifetime of O^+. We assumed that the model brightness of OII 83.4 nm emission ($I_{O^+}(t)$) was proportional to $N_{O^+}(t)$

$$\begin{aligned} I_{O^+}(t) &= \beta N_{O^+}(t) \\ &= p\int_{-\infty}^{t} I_O(t') exp\left(-\frac{t-t'}{\tau_{O^+}(t')}\right) dt', \end{aligned} \tag{5.8}$$

where β is a constant, $p = \alpha\beta$ is a fitting parameter. We fitted the model to the observed data using a least squares method in the range of τ_{low}, $\tau_{high} = 1 - 100$ days. The best-fit model has $\tau_{\mathrm{low}} = 40.5^{+1.5}_{-1.2}$ and $\tau_{\mathrm{high}} = 20.5^{+0.5}_{-0.4}$ days (solid line in Figure 5.5b). For

comparison, we also plot the model in the constant lifetime case of τ_{low}, τ_{high} = 40.5 days (dashed line). In this case, the model does not match the observations. We evaluated the errors in the same manner shown in Subsection 4.4.2 (see also Figure 5.6 (right)). Figure 5.6 (left) shows Chi-square distribution for two parameters (τ_{low}, τ_{high}). The left figure shows that τ_{high} is well constrained around 20 days while τ_{low} is allowed to have 30-50 days. Thus, Hisaki observations are consistent with a model that the lifetime of O^+ decreases when the density in the torus increases.

The main process to remove O^+ from the torus is radial transport, and loss processes caused with ionization and recombination should be small (Steffl et al., 2008). The transport time scale observed by Cassini were estimated to be 27 days in October 2000 (high density period) and 64 days in January 2001 (normal density period) (Delamere et al., 2004). Those estimated by Hisaki were 34±7 days in November 2013 (normal density period) and 9.9±0.9 days in February 2015 (high density period) (Yoshioka et al., 2018). The estimated value $\tau_{low} = 40.5^{+1.5}_{-1.2}$ days in this study is in the range of the error of the transport time scale estimated by Yoshioka et al. (2018), but shorter than that estimated by Delamere et al. (2004). The value $\tau_{high} = 20.5^{+0.5}_{-0.4}$ days is between the transport time scale estimated by Yoshioka et al. (2018) and Delamere et al. (2004).

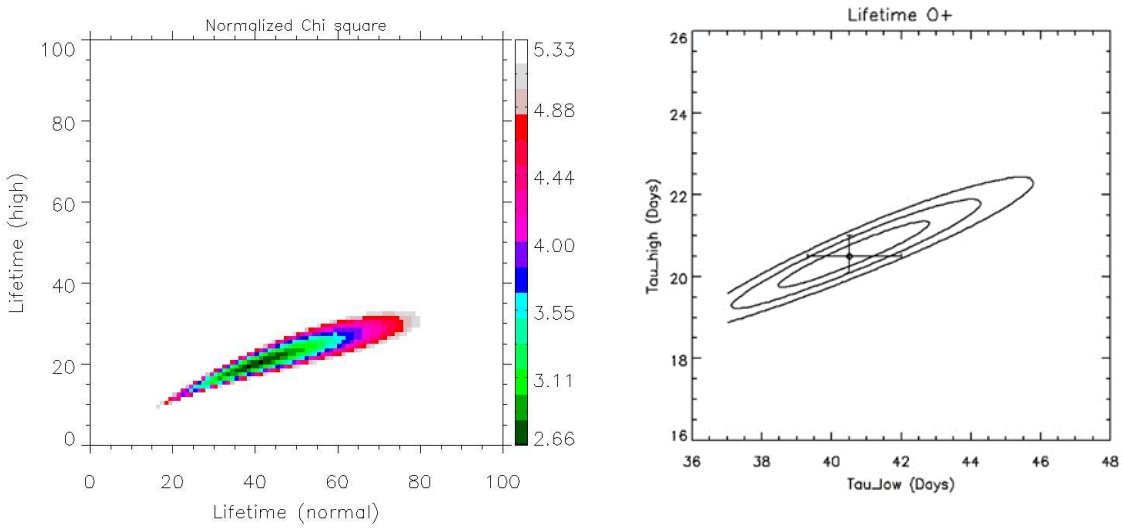

Figure 5.6. (Left) Normalized Chi-square distribution for two parameters (τ_{low}, τ_{high}). Number of data point of O^+ is 154. Distribution of fitting parameter *p* in equation (5) which minimizes Chi-square value. (Right) Plot of Chi-square for two parameters (τ_{low}, τ_{high}). The diamond mark is where the value of Chi-square is minimum ($\Delta X^2 = 0$). Ellipsoidal lines correspond to 1-sigma, 2-sigma, and 3-sigma ($\Delta X^2 = 2.3, 6.17, 11.8$). The 1-sigma ranges for the single parameter fit are over-plotted as a cross marking $\Delta X^2 = 1.0$.

5.3.2 Discussion

In this subsection, we discuss the increased radial outward transport of the torus ions in the high density period. The radial transport timescale can be estimated by integrating the radial transport equation (Cheng 1986, Schreier 1998, Delamere and Bagenal 2005).

$$\frac{d}{dL}\left[\frac{D_{LL}}{L^2}\frac{d(NL^2)}{dL}\right] = -\frac{\mathrm{N}}{\tau}, \tag{5.9}$$

where $L = R/R_J$ (R_J is Jupiter radius and R is the radial distance), D_{LL} is diffusion coefficient, N is the number of ions in a flux shell per unit L. Siscoe and Summers (1981) derived the diffusion coefficient. The coefficient in case of diffusion is dominated by centrifugally driven turbulence ($(D_{LL})_\Omega$) is

$$(D_{LL})_\Omega = -\frac{m^*\Omega^2 L^4}{4\pi\Sigma_p B_J^2 R_J^2}\left(\frac{dNL^2}{dL}\right)\langle(\Delta L)^2\rangle, \tag{5.10}$$

where m^* is the average mass of the ions, Ω is the speed of angular rotation of Jupiter, Σ_p is the height-integrated Pedersen conductivity, B_J is the equatorial magnetic field strength at Jupiter's surface, $\langle(\Delta L^2)\rangle$ is the mean size of the eddys at distance L. The quantity N can be represented by using the number density n (m^{-3}).

$$N = 2\pi \mathrm{R}_\mathrm{J}^2 H^* L n, \tag{5.11}$$

Where H^* is the average thickness of the plasma disc at distance L. The quantity $\langle(\Delta L^2)\rangle$ is not specified. They assumed

$$\langle(L^2)\rangle = (\Delta L)_0^2 (L/L_0)^p, \tag{5.12}$$

where p is a parameter which is not determined. Then, the diffusion coefficient becomes

$$(D_{LL})_\Omega = -k_\Omega L^{4+p}\frac{dNL^2}{dL}, \tag{5.13}$$

where k_Ω is the constant defined through equations (5.11) and (5.12). dNL^2/dL can be expressed as

$$\frac{dNL^2}{dL} \propto \frac{dnL^2}{dL} = L^2\frac{dn}{dL} + 2nL. \tag{5.14}$$

Equations (5.14) suggests the diffusion coefficient depends both on the gradient of plasma density and on the density itself. Yoshioka et al. (2018) assumes the radial profile of ion densities to be a form of a power function as shown in equation (4.7) and derived the radial profile in November 2013 (normal density period) and February 2015 (high density period) (see Table 5.4). The power low slopes of ions, in other words, the gradient of plasma density,

are not different statically between two periods. The number density at 5.91 R_J in the high density period (total 1694 cm^{-3}) is larger than that in the normal density period (1210 cm^{-3}). We expect that dNL^2/dL (and the diffusion coefficient $(D_{LL})_\Omega$) in the high density period is larger than in the normal period because the second term of the right hand side of Equation (5.14) ($2nL$) increases in the high density period. Yoshioka et al. (2018) suggested the increase of neutral production rate leads to the increase of electron impact ionization rates, and subsequently leads to heavier mass loading, which drives faster outward transport. The discussion described above supports their explanation.

Table 5.4. Radial profile of ion densities derived by Yoshioka et al. (2018). n_0 is number density at 5.91 R_J, and γ is power law slope of the profile.

	November 2013 (Normal)		February 2015 (High)	
Species	n_0 (cm^{-3})	γ	n_0 (cm^{-3})	γ
S^+	120±20	-7.1±1.2	400±35	-7.7±0.6
S^{2+}	530±80	-5.5±0.9	700±60	-5.1±0.5
S^{3+}	120±20	-3.7±1.1	54±9	-1.3±0.9
O^+	440±100	-3.6±1.4	540±70	-3.7±0.7

5.4 Summary

Major findings given in this chapter are as follows:

1. Atomic oxygen emission at 130.4 nm when Io was on the dawn side was always brighter than that when Io was on the dusk side. The dusk-to-dawn emission ratio was 1.13±0.03 on average from December 2013 to April 2014 and 1.21±0.03 from December 2014 to May 2015. The dawn-dusk asymmetry of core electron temperature explains the cause of the dawn-dusk asymmetry of atomic oxygen emission.
2. We estimated the total oxygen source rate in the neutral cloud as 410 kg/s directly from the radial profile of atomic oxygen emissions. This value is consistent with the results of Yoshioka et al. (2017) derived from the use of a physical chemistry model based on Hisaki observations. This value is also similar to the results based on Voyager 1 observations and the results based on Cassini observations in January 2001 (Delamere & Bagenal, 2003) but lower than those based on the Voyager 2 epoch and Cassini in September 2000, which were periods when Io was known to be volcanically active (Bagenal & Delamere, 2011; Delamere et al., 2004).
3. The time variations of OII emission during high density period is consistent with lifetimes of 40.5 days in the normal density period and 20.5 days in the high density period, suggesting that the lifetime of O^+ shortens with increasing the plasma density in the torus.

Chapter 6 Conclusions and future work

6.1 Conclusions

We demonstrated the spatial and velocity distribution of SO_2 emissions by analyzing ALMA archive data. Results are summarized in the following.

1. SO_2 emission maps showed the gases widely distributed around the equator of Io where the sublimation of the surface frost mainly occurs. We found presumed volcanically active areas in the east side and northern high latitude region (Region 1) and in the west side near the equator (Region 3). We also identified the area near Io's center where sublimation is expected to be dominant as Region 2, and the area southward of Region 1 as Region 4.
2. In Region 2, the atmosphere in all regions consists of multiple gases with different temperatures before ingress. This suggests that the atmosphere has either different source of volcanism and sublimation, or non-uniform vertical temperature profile. On the other hand, that the atmosphere became equilibrium after ingress. It is speculated that the upper atmosphere diminished extremely and the source of emission was dominated by the sublimation atmosphere in low altitude.
3. In Region 1, high and low velocity components are clearly identified in the velocity distribution before ingress. The Doppler shift of the high velocity component relative to the low velocity is ~0.6 km/s. The result suggests the significant volcanic plume generated complex atmospheric dynamics and some part of SO_2 gas flew at the line of sight direction.
4. In Region 3, the rotational temperature of SO_2 is 311±41 K after ingress, much higher than temperature of sublimation atmosphere (~100-200 K). It might reflect the temperature of gases which are emitted form volcanoes or/and heated by a hot lava lake.
5. Enhancements of the sodium nebula and IPT on the dusk side were observed by the ground base telescope and Hisaki in the same period of the ALMA observation. The direct volcanic input of SO_2 gases may trigger the enhancement of Io neutral and plasma torus.

Using the data obtained with Hisaki satellite, we examined the dependence of atomic oxygen 130.4 nm emission on the Io phase angle (IPA), and compared the distribution and variation of neutral oxygen cloud in the torus obtained in the normal density period (November to December, 2014) with that obtained in the high density period (January to April, 2015). Major findings are summarized in the following.

6. From the normal density period data, we found the averaged brightness in the IPA range of 60-90° on the dawn side and that of 240-270° on the dusk side are significant between 5-6 R_J and 6-7 R_J. Only the emissions at 6-7 R_J on the dusk side show symmetric distribution around the peak. We also found a weak and longitudinally uniform (or homogeneous) emission of atomic oxygen is clearly visible. The observation suggests Io's neutral oxygen cloud consists of two regions, namely, a dense region (banana cloud) around Io and a diffuse region with a longitudinally homogeneous distribution along Io's orbit. The banana cloud spreads along the leading side of Io and inside of Io's orbit.
7. We also found the maximum brightness of the atomic oxygen emission is inside of Io's orbit from the radial distribution in the normal density period. This suggests that the dense region extends inside of the Io's orbit rather than that of the outside. The neutral oxygen cloud spreads out to 7.6 Jupiter radii (R_J), where the brightness drops below ~1 R (corresponding to 1-sigma error).
8. From the high density period in 2015, we found rapid increase of oxygen UV emission and sodium visible emission simultaneously. From the middle of January 2015 to February 2015, the brightness of atomic oxygen 130.4 nm emission started increase from 10–15 R to the maximum more than 30 R. We revealed that atomic oxygen emission around Io increased by a factor of 2.5 when Io volcanism was active. The period for atomic oxygen brightness to increase from the volcanically quiet levels to the maximum levels near Io is almost the same as that of sodium at 50 R_J (30 days).
9. On the other hand, the duration of atomic oxygen brightness recovery from maximum levels to the quiet levels (before the volcanic event) was 60 days and longer than that of the sodium nebula of about 40 days. Time variation of electron densities and/or electron temperatures in Io's plasma torus after the volcanic eruption and the difference between source regions of NaCl and SO_2 could be possible mechanisms to explain the difference in the rates of decrease in brightness.
10. The evolution of the radial distribution of OI from 7 R_J to a maximum of 8.6 R_J shows Io's neutral oxygen cloud spread outward during the high density period. The estimated densities during the high density period from 13 to 27 February 2015 are 91^{+29}_{-25} cm^{-3} at 5.9 R_J, more than three times as large as those during the normal density period from 27 November to 31 December 2014 (27^{+8}_{-7} cm^{-3} at 5.9 R_J).

11. We found continuous outward expansions of Io's neutral oxygen cloud from the evolution of the azimuthal distribution during the high density period. The both densities of the banana cloud and the diffuse region increased.

We examined the source and loss processes of oxygen ion in the torus using the Hisaki observation data. Major findings are as follows.

12. Atomic oxygen 130.4 nm emission when Io was on the dawn side was always brighter than that when Io was on the dusk side. The averaged dusk-to-dawn emission ratio was 1.13±0.03 for the data obtained from December 2013 to April 2014, and 1.21±0.03 from the data obtained from December 2014 to May 2015. Both solar resonant scattering and electron impact excite OI 130.4 nm. The dawn-dusk asymmetry of core electron temperature explains the cause of the dawn-dusk asymmetry of atomic oxygen emission.
13. We estimated the total oxygen source rate in the neutral cloud as 410 kg/s from the radial profile of atomic oxygen 130.4 nm emissions. 100 kg/s was caused by electron impact ionization and 310 kg/s was caused by charge exchange. The total oxygen source rate estimated in this study is consistent with the results of Yoshioka et al. (2017), which were derived from the use of a physical chemistry model with Hisaki observations.
14. From the variations of OII 83.4 nm and OI 130.4 nm emissions from November 2014 to May 2015, we estimate lifetimes of O^+ to be 40.5 days in the normal density period and 20.5 days in the high density period, suggesting that the lifetime of O^+ shortens with increasing the plasma density in the torus. The dominant loss process of O^+ is thought to be radial outward transport. We consider the increase of neutral production rate leads to heavier mass loading, and drives faster outward transport.

6.2 Future work

Here, we propose new scientific subjects of Io's atmosphere, neutral clouds and IPT as well as Europa raised by this study. These are suitable to be made by ALMA and Hisaki observations in the future.

Io's atmosphere

When Io enters the Jupiter shadow, SO_2 saturation vapor pressure drops sharply as the surface temperature drops. Therefore, The SO_2 atmosphere after ingress is theoretically expected to drop by a factor of 1000 after ingress due to condensation. However, our results indicated that the number density of SO_2 only decreased about 40%. For the reason of a small amount of SO_2 decrease after ingress, the previous modeling study suggests SO may be preventing SO_2 from condensation [Moore et al., 2009]. However, the detail process preventing condensation of SO_2 has not been understood well. To solve this issue, it is necessary to clarify the interaction between SO_2 and SO during eclipse using DCMC (Direct Simulation of Monte Carlo) model.

In this study, we only discussed whether the atmosphere has multiple temperature or single temperature using population diagram. Understanding temperature and density vertical profile of Io's atmosphere below exobase (~400 km) will allow us to know the altitude of the exobase, and provide quantitative information about sputtering process between Io's atmosphere and the torus ions. In addition, it will allow us to know the response of temperature and density of the exosphere to fluctuations of volcanic activity. It is important to construct a radiative transfer model with multiple atmospheric layers and compare it with ALMA observations to derive vertical distribution of Io's atmosphere and its variations.

Neutral clouds and IPT

We found the radial and azimuthal non-uniform distribution of oxygen atoms around Io's orbit during the volcanically quiet period, and the change of the distribution during the active period by using Hisaki satellite data. Previous modeling studies with assumption of uniform sputtering of Io's atmosphere cannot reproduce the distribution obtained with Hisaki. To solve this issue, it is necessary to produce the model in the case that atmospheric sputtering occurs only in local areas. Such detailed models are also useful for understanding the process that volcanic plumes diffuse from the exosphere to the torus.

Temporal variations of radial distribution of IPT during a volcanic event is not understood well. Yoshioka et al., (2018) and Hikida et al., (2019) show the variability of electron temperature and ion temperatures and densities using plasma diagnosis of Hisaki data. However, they assumed the distribution follows power low. It is necessary to develop radial diffusion model which can solve the time evolution to estimate the radial distribution of IPT which is not confined by their assumption. This study can contribute to develop the model in

terms of providing input parameters such as ionization rate of oxygen atom and lifetimes of O^+ during normal and high density periods which had never observed before Hisaki.

Europa

Jupiter moon Europa orbits outside of Io, and its surface mainly composed by ice. Europa's atmosphere is mainly created by surface sputtering with torus ions originated from Io. Thus, there may be positive relation between enhancement of IPT and Europa's atmosphere. However, such relationship has still not understood well. To solve this issue, coordinated observation of IPT and Europa's O_2 and O atmosphere is required. In order to know the total amount of Europa's atmosphere, it is necessary to observe the total flux of UV OI 130.4 nm and 135.6 nm, and/or visible OI 630.0 nm. Observation of the visible light is limited only when Europa enters Jupiter's shadow. Space large telescopes such as Hubble Space Telescope only can observe OI 130.4 nm and OI 135.6 nm, and on the other hand, observation of OI 630.0 nm can be realized by ground-based telescopes. Hisaki is allowed to extend the operation by the end of 2020, and plans to apply for an additional operation. Hisaki continues to provide continuous observation data of IPT data, and it is important to plan simultaneous observation with a large telescope during this period.

Reference

Bagenal, F. (1994), Empirical model of the Io torus: Voyager measurements. *Journal of Geophysical Research: Space Physics*, *99*(A6), 11043–11062. doi:10.1029/93JA02908

Bagenal, F., & Delamere, P. A. (2011), Flow of mass and energy in the magnetospheres of Jupiter and Saturn. *Journal of Geophysical Research: Space Physics*, *116*(A5), A05209. doi:10.1029/2010JA016294

Barbosa, D. D. and M. G. Kivelson (1983), Dawn-dusk electric field asymmetry of the Io plasma torus, *Geophysical Research Letters*, 10, 210-213. https://doi.org/10.1029/GL010i003p00210

Barth, C. A (1969), Planetary ultraviolet spectroscopy, *Appl.* Opt. 8, 1295-1304.

Brown, R. A. (1981), The Jupiter hot plasma torus: observed electron temperature and energy flows, *The Astrophysical Journal*, 244, 1072–1080, doi: 10.1086/158777

Brown, M. E., & Bouchez, A. H. (1997), The response of Jupiter's magnetosphere to an outburst on Io, *Science*, 278, 268-271. doi: 10.1126/science.278.5336.268

Brown, R. A. and Chaffee Jr., F. H. (1974), High-resolution spectra of sodium emission from Io, *The Astrophysical Journal*, 187, 125-126.

Burger, M. H (2006), Io's neutral clouds: From the atmosphere to the plasma torus, PhD thesis, University of Colorado, Boulder, USA.

Burger, M. H., & Johnson, R. E. (2004), Europa's neutral cloud: Morphology and comparisons to Io. *Icarus*, *171*(2), 557–560. doi:10.1016/j.icarus.2004.06.014

Clarke, J. T., J. Ajello, J. Luhmann, N. Schneider, I. Kanik (1994), Hubble Space Telescope UV observations of Io passing into eclipse, *Journal of Geophysical Research*, 99, 8387-8402. https://doi.org/10.1029/93JE02547

Cantrall, C., de Kleer, K., de Pater, I., Williams, D. A., Davies, A. G., & Nelson, D. (2018). Variability and geologic associations of volcanic activity in 2001–2016. *Icarus*, *312*, 267–294. https://doi.org/10.1016/j.icarus.2018.04.007

Cheng, A. F. (1986), Radial diffusion and ion partitioning in the Io torus, *Geophysical Research Letters*, 13, 517. https://doi.org/10.1029/GL013i006p00517

Delamere, P. A., & Bagenal, F. (2003), Modeling variability of plasma conditions in the Io torus. *Journal of Geophysical Research: Space Physics*, *108*(A7), 1276. doi:10.1029/2002JA009706

Delamere, P. A., Steffl, A., & Bagenal, F. (2004), Modeling temporal variability of plasma conditions in the Io torus during the Cassini era. *Journal of Geophysical Research: Space Physics*, 109(A10), A10216. doi:10.1029/2003JA010354

Delamere, P. A., Bagenal, F., & Steffi, A. (2005), Radial variations in the Io plasma torus during the Cassini era. *Journal of Geophysical Research: Space Physics*, 110(A12), 1–13. doi:10.1029/2005JA011251

Del Zanna, G., Dere, K. P., Young, P. R., Landi, E., & Mason, H. E. (2015), CHIANTI – An atomic database for Emission Lines. Version 8. *Astronomy & Astrophysics*, 582, A56. doi:10.1051/0004-6361/201526827

Dols, V. J., Delamere, P. A., & Bagenal, F. (2008), A multispecies chemistry model of Io's local interaction with the plasma torus. *Journal of Geophysical Research*, 113, A09208. doi:10.1029/2007JA012805

Dols, V. J., Delamere, P. A., Bagenal, F., Kurth, W. S., & Paterson, W. R. (2012), Asymmetry of Io's outer atmosphere: Constraints from five Galileo flybys. *Journal of Geophysical Research*, 117, E10010. doi:10.1029/2012JE004076

Douté, S., Schmitt, B., Lopes-Gautier, R., Carlson, R., Soderblom, L., & Shirley, J. (2001). Mapping SO2 Frost on Io by the Modeling of NIMS Hyperspectral Images. *Icarus*, *149*(1), 107–132. https://doi.org/10.1006/icar.2000.6513

Durrance, S. T., P. D. Feldman, and H. A. Weaver (1983), Rocket detection of ultraviolet emission from neutral oxygen and sulfur in the Io torus, *The Astrophysical Journal*, 267, 125-129. doi: 10.1086/184016

Durrance, S. T., Feldman, P. D., Blair, W. P., Davidsen, A. F., Kriss, G. A., Kruk, J. W., et al. (1995), Neutral sulfur emission from the Io torus measured with the Hopkins ultraviolet telescope. *The Astrophysical Journal*, *447*, 408–415. doi:10.1086/175884

Ewing, C.T. and K. H. Stern (1974), Equilibrium vaporization rates and vapor pressures of solid and liquid sodium chloride, potassium bromide, cesium iodide, and lithium fluoride, J. phys. Chem, 78, 1998-2005. https://doi.org/10.1021/j100613a005

Feaga, L. M., McGrath, M., Feldman, P. D. 2009, Io's dayside SO_2 atmosphere, *Icarus*, 201, 579-584. https://doi.org/10.1016/j.icarus.2009.01.029

Feldman, P. D., Strobel, D. F., Moos, H. W., Retherford, K. D., Wolven, B. C., McGrath, M. A., Roesler, F. L., Woodward, R. C., Oliversen, R. J., Ballester, G. E., 2000. Lyman-α imaging of the SO_2 distribution on Io. *Geophysical Research Letters*, 27, 1787–1790. https://doi.org/10.1029/1999GL011067

Geissler, P., McEwen, A., Porco, C., Strobel, D., Saur, J., Ajello, J., & West, R. (2004). Cassini observations of Io's visible aurorae. *Icarus*, *172*, 127–140. https://doi.org/10.1016/j.icarus.2004.01.008

Gladstone, G. R. (1992), Solar OI 1304 Å triplet line profiles, J. Geophys. Res, 97, 19,519-19,525. https://doi.org/10.1029/JA093iA12p14623

Giorgini, J.D., Yeomans, D.K., Chamberlin, A.B., Chodas, P.W., Jacobson, R.A., Keesey, M.S., Lieske, J.H., Ostro, S.J., Standish, E.M., Wimberly, R.N., "JPL's On-Line Solar System Data Service", Bulletin of the American Astronomical Society, Vol 28, No. 3, p. 1158, 1996.

Hikida, R., Yoshioka K, Tsuchiya F, Kagitani M, Kimura T, Bagenal F, Schneider N, Murakami G, Yamazaki A, Kita H, & Yoshikawa I. (2019). Spatially asymmetric increase in hot electron fraction in the Io plasma torus during volcanically active period revealed by observations by Hisaki/EXCEED from November 2014 to May 2015. Journal of Geophysical Research: Space Physics, in print

Hogbom, J. A., Aperture synthesis with a non-regular distribution of interferometer baselines, Astron. Astrophys. Suppl., 15, 417-426.

Ingersoll, A. P. (1989), Io Meteorology: How atmospheric pressure is controlled locally by volcanos and surface frosts, Icarus, 81, 298-313. https://doi.org/10.1016/0019-1035(89)90055-9

Ip, W. H. and C. K Goertz (1983), An interpretation of the dawn-dusk asymmetry of UV emission from the Io plasma torus, Nature, 302, 232-233. https://doi.org/10.1038/302232a0

Jessup, K. L., Spencer, J. R., Ballester, G. E., Howell, R. R., Roesler, F., Vigel, M., & Yelle, R. (2004). The atmospheric signature of Io's Prometheus plume and anti-jovian hemisphere: Evidence for a sublimation atmosphere. *Icarus*, *169*(1), 197–215. https://doi.org/10.1016/j.icarus.2003.11.015

Keszthelyi, L, A. S. McEvan, C. B. Phillips, B. Milazzo, P. Geissler, E. P. Turtle, J. Radebaugh, D. A. Williams, D. Simonelli, H. Breneman et al. (2001), Imaging of volcanic activity on Jupiter's moon Io by Galileo during GEM and GNN. J. Geophys. Res, 106, 33025-22052.

Kimura, T., Hiraki, Y., Tao, C., Tsuchiya, F., Delamere, P. A., Yoshioka, K., et al. (2018). Response of Jupiter's aurora to plasma mass loading rate monitored by the Hisaki satellite during volcanic eruptions at Io. *Journal of Geophysical Research: Space Physics*, 123, 1885–1899. doi:10.1002/2017JA025029

Kimura, T., Yamazaki, A., Yoshioka, K., Murakami, G., Tsuchiya, F., Kita, H., et al. (2019), Development of ground pipeline system for high-level scientific data products of the Hisaki satellite mission and its application to planetary space weather. *J. Space Weather Space Clim.*, 9, A8. doi: 10.1051/swsc/2019005

de Kleer, K and I, de Peter (2016), Time variability of Io's volcanic activity from near-IR adaptive optics observations on 100 nights in 2013-2015, Icarus, 280, 378-404. https://doi.org/10.1016/j.icarus.2016.06.019

de Kleer, K., de Pater, I., & Ádámkovics, M. (2019). Emission from volcanic SO gas on Io at high spectral resolution. *Icarus*, 317, 104–120. https://doi.org/10.1016/j.icarus.2018.07.012

Koga, R., Tsuchiya, F., Kagitani, M., Sakanoi, T., Yoneda, M., Yoshioka, K., et al. (2018a), The time variation of atomic oxygen emission around Io during a volcanic event observed with Hisaki/EXCEED. *Icarus*, 299, 300–307. doi:10.1016/j.icarus.2017.07.024

Koga, R., Tsuchiya, F., Kagitani, M., Sakanoi, T., Yoneda, M., Yoshioka, K., et al. (2018b). Spatial distribution of Io's neutral oxygen cloud observed by Hisaki. J*ournal of Geophysical Research: Space Physics*, 123, 3764–3776. doi:10.1029/2018JA025328

Kuppers, M., & Schneider, N. M. (2000). Discovery of chlorine in the Io torus. *Geophysical Research Letters*, *27*(4), 513–516. https://doi.org/10.1029/1999GL010718

Lellouch, E., Belton, M., de Pater, I. *et al* (1990). Io's atmosphere from microwave detection of SO_2. *Nature*, 346, 639–641. https://doi.org/10.1038/346639a0

Lellouch, E., Belton, M., De Pater, I., Paubert, G., Gulkis, S., & Encrenaz, T. (1992). The structure, stability, and global distribution of Io's atmosphere. *Icarus*, *98*(2), 271–295. https://doi.org/10.1016/0019-1035(92)90095-O

Lellouch, E., Strobel, D. F., Belton, M. J. S., Summers, M. E., Paubert, G., & Moreno, R. (1996). Detection of Sulfur Monoxide in Io's Atmosphere. *The Astrophysical Journal*, *459*(2), 1994–1997. https://doi.org/10.1086/309956

Lellouch, E., Paubert, G., Strobel, D. F. & Balton, M. (2000) Millimeter-wave observations of Io's atmosphere: The IRAM 1999 campaign. *Bull, Amer. Astron. Soc.*, 32, 3511.

Lellouch, E., G. Paubert, J. I. Moses, N. M. Schneider, D. F. Strobel (2003), Volcanically emitted sodium chloride as a source for Io's neutral clouds and plasma torus, *Nature*, 421, 45–47. https://doi.org/10.1038/nature01292

Lopes, R. M., Kamp, L. W., Smythe, W. D., Marl, P. M., Kargerl, J., Radebaugh, J., Turtle, E. P., Perry J., Williams, D. A., Carlson, R. W., Douté, S., and the Galileo NIMS and SSI teams (2004), Lava lakes on Io: observations of Io's volcanic activity from Galileo NIMS during the 2001 fly-bys, *Icarus*, 169, 140-174. https://doi.org/10.1016/j.icarus.2003.11.013

McGrath, M. A. & Johnson, R. E. (1987), Magnetospheric plasma sputtering of Io's atmosphere, *Icarus*, 69, 519-531. https://doi.org/10.1016/0019-1035(87)90021-2

McGrath, M. A., Lellouch, E., Strobel, D. F., & Johnson, R. E. (2004), Satellite atmospheres. In F. Bagenal, T. E. Dowling, & W. B. McKinnon (Eds.), *Jupiter: The planet, satellites and magnetosphere* (pp. 457–483). Cambridge, UK: Cambridge University Press.

Mendillo, M., Spencer, W. J., and Stansberry, J. (2004), Io's volcanic control of Jupiter's extended neutral clouds, *Icarus*, 170, 430-442. https://doi.org/10.1016/j.icarus.2004.03.009

Moore, C. H., Goldstein, D. B., Varghese, P. L., Trafton, L. M., & Stewart, B. (2009). 1-D DSMC simulation of Io's atmospheric collapse and reformation during and after eclipse. *Icarus*, *201*(2), 585–597. https://doi.org/10.1016/j.icarus.2009.01.006

Moore, C., Miki, K., Goldstein, D. B., Stapelfeldt, K., Varghese, P. L., Trafton, L. M., & Evans, R. W. (2010). Monte Carlo modeling of Io's [OI] 6300Å and [SII] 6716Å auroral emission in eclipse. *Icarus*, *207*(2), 810–833. https://doi.org/10.1016/j.icarus.2010.01.004

Moullet, A., Lellouch, E., Moreno, R., Gurwell, M. a., & Moore, C. (2008). First disk-resolved millimeter observations of Io's surface and SO 2 atmosphere. *Astronomy and Astrophysics*, *482*(1), 279–292. https://doi.org/10.1051/0004-6361:20078699

Moullet, A., Gurwell, M. A., Lellouch, E., & Moreno, R. (2010). Simultaneous mapping of SO2, SO, NaCl in Io's atmosphere with the Submillimeter Array. *Icarus*, *208*(1), 353–365. https://doi.org/10.1016/j.icarus.2010.02.009

Moullet, A., Lellouch, E., Moreno, R., Gurwell, M., Black, J. H., & Butler, B. (2013). Exploring Io's atmospheric composition with apex: First measurement of 34SO2 and tentative detection of KCl. *Astrophysical Journal*, *776*(1). https://doi.org/10.1088/0004-637X/776/1/32

Moullet, A. (2015), Exploring the Solar System with ALMA, REVOLUTION IN ASTRONOMY WITH ALMA: THE THIRD YEAR, ASP Conference Series, Vol. 499

Morgenthaler, J. P., Rathbun, J. A., Schmidt, C. A., Baumgardner, J and Schneider, N. M. (2019), Large volcanic event on Io inferred from Jovian sodium nebula brightening, The Astrophysical Journal Letters, 871, L23 (6pp).

Moses. J. I., Zolotov, M. Y. and Fegley, Jr. B. (2002), Alkali and chlorine photochmistry in a volcanically driven atmosphere on Io, *Icarus*, 156, 107-135. https://doi.org/10.1006/icar.2001.6759

Moullet, A., Lellouch, E., Moreno, R., Gurwell, M. A., & Moore, C. (2008). First disk-resolved millimeter observations of Io's surface and SO_2 atmosphere. *Astronomy and Astrophysics*, *482*(1), 279–292. https://doi.org/10.1051/0004-6361:2007869

Murcray, F. J., R. Goody (1978), Astronomical monochromatic imaging as applied to the Io sodium cloud, Applied Optics, 17, 19, 3117-3124.

Oliversen, R. J., Scherb, F., Smyth, W. H., Freed, M. E., Woodward Jr., R. C., Marconi, M. L., Retherford, K. D., Luppie, O. L. and Morgenthaler, J. P. (2001), Sunlit Io atomosperic [OI] 6300 Å emission and the plasma torus, *Journal of Geophysical Research*, 106, 26,183-26,193. https://doi.org/10.1029/2000JA002507

de Pater, I., Roe, H., Graham, J. R., Strobel, D. F., & Bernath, P. (2002). Detection of the forbidden SO $a^1\Delta \rightarrow X^3\Sigma^-$ rovibronic transition on lo at 1.7 μm. *Icarus*, *156*(1), 296–301. https://doi.org/10.1006/icar.2001.6787

Petry, D. et al., 2018, ALMA QA2 Data Products for Cycle 5, Version 2.0, ALMA

Press, W. H., Teukolsky, S. A., Vetterling, W. A., & Flannery, B. P. (1992), Numerical Recipes in C: The Art of Scientific Computing, 2nd ed., Cambridge Univ. Press, New York.

Remijan, A., Biggs, A., Cortes, P., A., Dent, B., Di Francesco, J., Fomalont, E., Hales, A., Kameno, S., Mason, B., Philips, N., Saini, K., Stoehr, F., Vila Vilaro, B., Villard, E. 2019, ALMA Technical Handbook, ALMA Doc. 7.3, ver. 1.1, ISBN 978-3-923524-66-2

Retherford, K. D. (2002), Io's Aurora: HST/STIS Observations, PhD Thesis, Johns Hopkins University, Baltimore, USA

Retherford, K. D. et al. (2007), Io's atmospheric response to eclipse: UV aurorae observations, Science, 318, 237-240. doi: 10.1126/science.1147594

Roesler, F. L., H. W. Moos, R. J. Oliversen, R. C. Woodward Jr., K. D. Retherford, F. Scherb, M. A. McGrath, W. H. Smyth, P. D. Feldman, and D. F. Strobel (1999), Far-ultraviolet imaging

spectroscopy of Io's atmosphere with HST/STIS. Science, 283, 353–357. doi: 10.1126/science.283.5400.353

Saur, J., Strobel, D. F., Neubauer, F. M. & Summers, M. E. (2003), The ion mass loading rate at Io, Icarus, 163, 456-468. doi: 10.1016/S0019-1035(03)00085-X

Saur. J, D. F. Strobel (2004), Relative contributions of sublimation and volcanoes to Io's atmosphere inferred from its plasma interaction during solar eclipse, *Icarus*, 214, 495-509. https://doi.org/10.1016/j.icarus.2004.05.010

Scherb, F., & Smyth, W. H. (1993), Variability of [O I] 6300-Å emission near Io. *Journal of Geophysical Research*, *98*, 18729–18736. doi:10.1029/93JE00539

Schieven, G., ed., 2019, Observing with ALMA – A Primer, ALMA Doc. 7.1, ver. 1

Schneider, N. M., Hunten, D. M., Wells, W. K., Schultz, A. B. & Fink., U. (1991), The structure of Io's corona, *The Astrophysical Journal*, 368, 298-315.

Schneider, N. M., & Bagenal, F. (2007), Io's neutral clouds, plasma torus, and magnetospheric interaction. In R. M. C. Lopes, & J. R. Spencer (Eds.), Io after Galileo, A new view of Jupiter's volcanic moon (pp. 265–286). Springer.

Schreier, R., Eviatar, A., & Vasyliūnas, V. M. (1998), A two-dimensional model of plasma transport and chemistry in the Jovian magnetosphere. *Journal of Geophysical Research*, 103, 19901–19913. doi:10.1029/98JE00697

Siscoe, G., L. & Summers, D. (1981), Centrifugally driven diffusion of Iogenic plasma, Journal of Geophysical Research, 86, A10, 8471-8479. https://doi.org/10.1029/JA086iA10p08471

Skinner, T. E., & Durrance, S. T. (1986), Neutral oxygen and sulfur densities in the Io torus. *The Astrophysical Journal*, 310, 966–971. doi: 10.1086/164747

Smith, H. T., Mitchell, D. G., Johnson, R. E., Mauk, B. H., & Smith, J. E. (2019), Europa Neutral Torus Confirmation and Characterization Based on Observations and Modeling, *The Astrophysical Journal*, 871, 69. doi:10.3847/1538-4357/aaed38

Smyth, W.H., 1998. Energy escape rate of neutrals from Io and the implications for local magnetospheric interactions. *Journal of Geophysical Research*. 103, 11941–11950

Smyth, W. H., & Combi, M. R. (1988), A general model for Io's neutral gas clouds. II - Application to the sodium cloud, *The Astrophysical Journal*, 328, 888-918. doi: 10.1086/166346

Smyth, W. H., & Combi, M. R. (1997), Io's Sodium Corona and Spatially Extended Cloud: A Consistent Flux Speed Distribution, *Icarus*, 126, 58-77, doi: 10.1006/icar.1996.5633

Smyth, W. H., & Shemansky, D. E. (1983), Escape and ionization of atomic oxygen from Io. *The Astrophysical Journal*, 271, 865–875. doi:10.1086/161252

Smyth, W. H., & Marconi, M. L. (2000), Io's oxygen source: Determination from ground-based observations and implications for the plasma torus, *Journal of Geophysical Research*, 105, 7783. doi: 10.1029/1999JA000308

Smyth, W. H., & Marconi, M. L. (2003), Nature of the iogenic plasma source in Jupiter's magnetosphere. I. Circumplanetary distribution. *Icarus*, 166(1), 85–106. doi:10.1016/S0019-1035(03)00176-3

Smyth, W. H., & Marconi, M. L. (2005), Nature of the iogenic plasma source in Jupiter's magnetosphere. II. Near-Io distribution. *Icarus*, 176(1), 138-154. doi:10.1016/j.icarus.2005.01.010

Smyth, W. H., & McElroy, M. B. (1978), Io's sodium cloud: comparison of models and two-dimensional images. *The Astrophysical Journal*, *226*, 336–346. doi: 10.1086/156613

Smyth, W. H., & Wong, M. C. (2004), Impact of electron chemistry on the structure and composition of Io's atmosphere, *Icarus*, 171, 171-182. doi:10.1016/j.icarus.2004.04.001

Spencer, J. R., Stern, S. A., Cheng, A. F., Weaver, H. A., Reuter, D.C. et al. (2007). Io Volcanism Seen by New Horizons : *Science*, *240*(1999). https://doi.org/10.1126/science.1147621

Steffl, A. J., Stewart, A. I. F. & Bagenal, F. (2004), Cassini UVIS observations of the Io plasma torus: I. Initial results, *Icarus*, 172, 78–90. doi:10.1016/j.icarus.2003.12.027

Steffl, A. J., Delamere, P. A. & Bagenal. F. (2006), Cassini UVIS observations of the Io plasma torus: III. Observations of temporal and azimuthal variability, *Icarus*, 180, 124-140, https://doi.org/10.1016/j.icarus.2005.07.013

Steffl, A. J., Delamere, P. A. & Bagenal, F. (2008), Cassini UVIS observations of the Io plasma torus IV. Modeling temporal and azimuthal variability, *Icarus*, 194, 153-165. doi:10.1016/j.icarus.2007.09.019

Stoehr, F. et al. 2019, ALMA Science Archive Manual, ALMA Doc. 7.15 v1.0

Stone, E. J. and E. C. Zipf (1974), Electron impact excitation of the 3S0 and 5S0 states of atomic oxygen, J. Chem. Phys., 60, 11, 4237-4243. https://doi.org/10.1063/1.1680894

Tao, C., Kimura, T., Tsuchiya, F., Murakami, G., Yoshioka, K., Yamazaki, A., et al (2018). Variation of Jupiter's aurora observed by Hisaki/EXCEED: 3. Volcanic control of Jupiter's aurora. *Geophysical Research Letter*, 45, 71–79. doi:10.1002/2017GL075814

Tsang, C. C. C., Spencer, J. R., & Jessup, K. L. (2015). Non-detection of post-eclipse changes in Io's Jupiter-facing atmosphere: Evidence for volcanic support? *Icarus*, *248*, 243–253. https://doi.org/10.1016/j.icarus.2014.10.033

Tsang, C. C. C., Spencer, J. R., Lellouch, E., Lopez-valverde, M. A., Richter, M. J., & Al, T. E. T. (2016). Journal of Geophysical Research : Planets The collapse of Io ' s primary atmosphere in Jupiter eclipse, 1400–1410. https://doi.org/10.1002/2016JE005025.Received

Tsuchiya, F., Arakawa, R., Misawa, H., Kagitani, M., Koga, R., Suzuki, F., et al. (2019), Azimuthal variation in the Io plasma torus observed by the Hisaki satellite from 2013 to 2016, *Journal of Geophysical Research: Space Physics*, doi: 10.1029/2018JA026038

Tsuchiya, F., Yoshioka, K., Kimura, T., Koga, R., Murakami, G., Yamazaki, A., et al. (2018). Enhancement of the Jovian Magnetospheric plasma circulation caused by the change in plasma supply from the satellite Io. *Journal of Geophysical Research: Space Physics*. 123, 6514–6532. doi:10.1029/2018JA025316

Thomas, N (1996), high resolution spectra of Io's neutral potassium and oxygen clouds, Astron. Astrophys, 313, 306-314.

Thomas, N., Bagenal, F., Hill, T., & Wilson, J. (2004). The Io neutral clouds and plasma torus. In Bagenal, F., Dowling, T. E., & McKinnon, W. B. (Eds.), Jupiter: The planet, satellites and magnetosphere (pp. 561–592). Cambridge, UK: Cambridge University Press. ISBN-10: 0521818087.

Underwood, D. S., Tennyson, J., Yurchenko, S. N., Huang, X., Schwenke, D. W., Lee, T. J., Clausen, S., Fateev, A. (2016), "ExoMol molecular line lists - XIV: The rotation-vibration spectrum of hot SO2", Monthly Notices of the Royal Astronomical Society 459, 3890-3899.

Wagman, D. D. (1979). Sublimation pressure and the enthalpy of SO_2. Chem. Thermodyn. Data Cent., Natl. Bur. of Stand., Washington, DC.

Williams, D. A., Robert, R. H., Active volcanism: Effusive eruptions (2007), Io after Galileo, Springer, ISBN-10:3-540-34681-3.

Wolven, B., H. W. Moos, K. D. Retherford, and P. D. Feldman (2001), Emission profiles of neutral oxygen and sulfur in Io's exospheric corona. J. Geophys. Res. 106, 26,155–26,182.

Wilson, J. K., M. Mendillo, J. Baumgardner, N. M. Schneider, and B. Flynn (2002), The dual sources of Io's sodium clouds, Icarus, 167, 476-489. https://doi.org/10.1006/icar.2002.6821

Wilson, J. K. and N. M. Schneider (1994), Io's fast sodium: implication for molecular and atomic atmospheric escape, Icarus, 111, 31-44. https://doi.org/10.1006/icar.1994.1131

Wilson, T. L., Rohlfs, K. & Huttemeister, S. (2009), Tools of Radio Astronomy Fifth Edition, Springer. doi:10.1007/978-3-540-85122-6

Wong, M. C., and R. E. Johnson 1995. The effect of plasma heating on sublimation-driven flow in Io's atmosphere. Icarus 115, 109–118. https://doi.org/10.1006/icar.1995.1082

Wong, M. C., & Johnson, R. E. (1996). A three-dimensional azimuthally symmetric model atmosphere for Io 1. Photochemistry and the accumulation of a nightside atmosphere. *Journal of Geophysical Research E: Planets*, *101*(E10), 23243–23254. https://doi.org/10.1029/96JE02510

Wong, M. C., & Smyth, W. H. (2000). Model calculations for Io's atmosphere at eastern and western elongations. *Icarus*, *146*(1), 60–74. https://doi.org/10.1006/icar.2000.6362

Woods, T. N. and G. Rottman (2005), XUV Photometer System (XPS): Solar Variations during the SORCE mission, Solar Physics, 230, 375-387.

Yamazaki, A., Tsuchiya, F., Sakanoi, T., Uemizu, K., Yoshioka, K., Murakami, G., et al. (2014), Field-of-View guiding camera on the HISAKI (SPRINT-A) satellite. *Space Science Reviews*, 184(1–4), 259–274. doi:10.1007/s11214-014-0106-y

Yoneda, M (2007), Short-term variability of Jupiter's extended sodium nebula, Master thesis, Tohoku university, Sendai, Japan.

Yoneda, M., Kagitani, M., Okano, S. (2009), Short-term variability of Jupiter's extended sodium nebula, Icarus, 204**,** 589–596. https://doi.org/10.1016/j.icarus.2009.07.023

Yoneda, M., Nozawa, H., Misawa, H., Kagitani, M. & Okano, S. (2010), Jupiter's magnetospheric change by Io's volcanoes, *Geophysical Research Letters*, 37, 11202–11206. doi:10.1029/2010GL043656

Yoneda, M., Kagitani, M., Tsuchiya, F., Sakanoi, T., & Okano, S. (2015), Brightening event seen in observations of Jupiter's extended sodium nebula. *Icarus*, 261, 31–33. doi:10.1016/j.icarus.2015.07.037

Yoshikawa, I., Yoshioka, K., Murakami, G., Yamazaki, A., Tsuchiya, F., Kagitani, M., et al. (2014), Extreme ultraviolet radiation measurement for planetary atmospheres/magnetospheres from the Earth-orbiting spacecraft (Extreme Ultraviolet Spectroscope for Exospheric Dynamics: EXCEED). *Space Science Reviews*, 184(1–4), 237–258. doi:10.1007/s11214-014-0077-z

Yoshikawa, I., Suzuki, F., Hikida, R., Yoshioka, K., Murakami, G., Tsuchiya, F., et al., (2017). Volcanic activity on Io and its influence on the dynamics of the Jovian magnetosphere

observed by EXCEED/Hisaki in 2015. *Earth, Planets and Space*, 69:110. doi:10.1186/s40623-017-0700-9

Yoshioka, K., Murakami, G., Yamazaki, A., Tsuchiya, F., Kagitani, M., Sakanoi, T., et al. (2013), The extreme ultraviolet spectroscope for planetary science, EXCEED. *Planetary and Space Science*, 85, 250–260. doi:10.1016/j.pss.2013.06.021

Yoshioka, K., G. Murakimi, A. Yamazaki, F. Tsuchiya, T. Kimura, M. kagitani, T. Sakanoi, K. Uemizu, Y. Kasaba, I. Yoshikawa, and M. Fujimoto (2014), Evidence for global electron transportation into the jovian inner magnetosphere, Science, 345, 1581-1584. doi: 10.1126/science.1256259

Yoshioka, K., Tsuchiya, F., Kimura, T., Kagitani, M., Murakami, G., Yamazaki, A., et al. (2017), Radial variation of sulfur and oxygen ions in the Io plasma torus as deduced from remote observations by Hisaki. *Journal of Geophysical Research: Space Physics*, 122(3), 2999–3012. doi:10.1002/2016JA023691

Yoshioka, K., Tsuchiya, F., Kagitani, M., Kimura, T., Murakami, G., Fukuyama, D., et al. (2018). The influence of Io's 2015 volcanic activity on Jupiter's magnetospheric dynamics. *Geophysical Research Letters*, 45, 10,193–10,199. doi:10.1029/2018GL079264

疋田伶奈, 吉岡和夫, 村上豪, 桑原正輝, 吉川一朗 (2017), 「ひさき衛星搭載の極端紫外分光撮像装置(EXCEED)の回折格子の性能評価」, 『宇宙航空研究開発機構研究開発報告』, JAXA-RR-16-012

JAXA homepage, Hisaki/SPRINT-A (referred on 31 January 2020) http://www.jaxa.jp/projects/sas/sprint_a/index_j.html